

OBSERVATION OF $W \rightarrow \mu\nu$ DECAYS
IN PROTON-ANTIPROTON COLLISIONS
AT $\sqrt{s} = 1.8$ TeV

BY

THOMAS KEVIN WESTHUSING

B.A., Rice University, 1981
M.S., University of Illinois, 1982

THESIS

Submitted in partial fulfillment of the requirements
for the degree of Doctor of Philosophy in Physics
in the Graduate College of the
University of Illinois at Urbana-Champaign, 1989

Urbana, Illinois

Q. 539. 725
Ta. 9w

UNIVERSITY OF ILLINOIS AT URBANA-CHAMPAIGN

THE GRADUATE COLLEGE

DECEMBER 6, 1988

WE HEREBY RECOMMEND THAT THE THESIS BY

THOMAS KEVIN WESTHUSING

ENTITLED OBSERVATION OF $W \rightarrow \mu\nu$ DECAYS IN PROTON-ANTIPROTON

COLLISIONS AT $\sqrt{s} = 1.8$ TeV

BE ACCEPTED IN PARTIAL FULFILLMENT OF THE REQUIREMENTS FOR

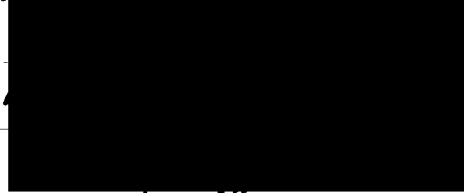
THE DEGREE OF DOCTOR OF PHILOSOPHY




Director of Thesis Research

Head of Department

Committee on Final Examination†

Chairperson

† Required for doctor's degree but not for master's.

University of Illinois
at Urbana-Champaign

Department of Physics

Loomis Laboratory of Physics
1110 West Green Street
Urbana
Illinois 61801

DEPARTMENTAL FORMAT APPROVAL

THIS IS TO CERTIFY THAT THE FORMAT AND QUALITY OF PRESENTATION OF THE
THESIS SUBMITTED BY THOMAS KEVIN WESTHUSING AS ONE OF
THE REQUIREMENTS FOR THE DEGREE OF Doctor of Philosophy
IS ACCEPTABLE TO THE Department of Physics.

(Full Name of Department, Division or Unit)

12-9-88

Date of Approval


[Redacted Signature]

Departmental Representative

OBSERVATION OF $W \rightarrow \mu\nu$ DECAYS
IN PROTON-ANTIPROTON COLLISIONS
AT $\sqrt{s} = 1.8$ TeV

Thomas Kevin Westhusing, Ph.D.
Department of Physics
University of Illinois at Urbana-Champaign, 1989
Professor L.E. Holloway, advisor

The production and subsequent decay to muon and neutrino of the W intermediate vector boson has been observed in $\bar{p}p$ collisions at a center-of-mass energy of 1.8 TeV at the Fermilab Tevatron collider. Details of the CDF detector are given and event selection criteria are developed. A cross section times branching ratio, based on a sample of three $W \rightarrow \mu\nu$ candidate events extracted from 27.2 ± 4.1 nb⁻¹ of data taken in the 1987 collider run, is calculated to be

$$\sigma_W \times B_{W \rightarrow \mu\nu} = 0.59^{+0.93}_{-0.32} (\pm 0.09) \text{ nb}$$

which is consistent with current theoretical predictions.

Acknowledgements

I would like to thank the multitude of people in the CDF collaboration whose long hours of labor and untold gigawatts of brain power created a remarkable detector.

To those comrades, George Redlinger and John Skarha, who shared with me those heady moments on Mount Olympus, I would like to say that it is better to rule in heaven, than to serve in "le bestia's" hell.

My advisor, Lee Holloway, deserves thanks for a management style which places a good deal of responsibility on those who are eager to find out what they can do and for his willingness to step in when they discover what they can't do.

I also wish to thank Dave Smith for not only providing practical advice whenever it appeared that DEC had undue influence on my life, but also for showing me that there are many avenues to explore besides the one we have chosen as a career. I also want to thank Dave Smith and Doria Mateja for a memorable evening on the roof of a mexican hotel in Taxco.

Throughout the last seven years I have had the friendship and support of many people including my fellow graduate students, those people working in the physics office, Dave Lesney, Jerry Wray, Tom Trumpinski, Harold Scott, Bob Sard, Inga Karliner, Steve Errede, Jim Wiss, Tony Liss, Dave Smith, and many others. I want to say thanks to all of you.

Finally I want to mention people to whom saying thanks is not enough. Barbara Gilbert and John Powell have changed my life and my debt to them is one that I can never repay. Two ladies who have also changed my life are my wife Cathy and daughter Lauren. They were always there when things got tough. I owe Lauren some heavy duty playing time.

This research was supported in part by the U.S. Department of Energy under contract DE-AC02-76ERO1195.

Contents

1	Introduction	1
2	Theory	3
3	Detector	11
3.1	Central Tracking Chamber	11
3.2	Central Drift Tubes	15
3.3	Central Calorimeter	15
3.4	Central Muon Chambers	17
4	Trigger	23
4.1	Central Muon Level 1 Trigger	23
4.2	Central Muon Level 2 Trigger	24
4.3	Trigger Performance	25
4.3.1	CMU Level 1	25
4.3.2	Central Fast Track Processor	28
4.3.3	CMU Level 2	30
5	Analysis	32
5.1	Require Muon $P_t > 10$ GeV/c	32
5.2	Remove Cosmic Rays	35
5.3	Require Muon $P_t > 20$ GeV/c	37
5.4	Require Muon to be Isolated	37
5.5	Require Muon to be Minimum Ionising	39
5.6	Require CTC, Muon Track Match	40

5.7	Require Missing E_t	43
5.8	W Candidates	45
5.9	Background	46
5.10	Efficiency	48
5.11	Cross Section	53
6	Conclusions	56
A	CDF Central Muon Detector	57
A.1	Introduction	57
A.2	Geometry	57
A.3	Chamber Construction	63
A.4	Charge Division	69
A.5	Chamber Performance	70
A.6	Conclusion	84
B	CDF Event Displays	85
C	Two Interesting Events	99
	Bibliography	104
	Vita	106

List of Figures

2.1	Contact Diagram for Weak Interactions	3
2.2	Drell-Yan Production of W Bosons	5
2.3	Rapidity distribution of W's at 1.8 TeV	6
2.4	Muon P_t distribution of the muons from W decay	7
2.5	Pseudorapidity of the muons from W decay	7
2.6	Transverse mass of W's	8
2.7	Transverse momentum distribution of W's at 1.8 TeV	10
3.1	CDF Detector.	12
3.2	CTC Residuals (a) R- ϕ Fit (b) R-Z Fit	13
3.3	$Z_{CTC} - Z_{VTPC}$ at the Beam Axis	15
3.4	(a) $\phi_{CTC} - \phi_{CDT}$ (b) $Z_{CTC} - Z_{CDT}$	16
3.5	CEM Energy Deposition for 57 GeV/c Muons	17
3.6	CHA Energy Deposition for 57 GeV/c Muons	18
3.7	End View of CMU Chamber	19
3.8	CMU Drift Times	20
3.9	Number Hits per CMU Track (a) R- ϕ Fit (b) R-Z Fit	21
3.10	CMU Track Residuals (a) R- ϕ Fit (b) R-Z Fit	22
4.1	CMU Level 1 Efficiency	24
4.2	TDC Difference (ns) CMU Level 1 (a) True (b) False	26
4.3	P_t Spectrum with CMU Level 2 + Other Trigger	27

4.4	P_t Spectrum with CFT Only + Other Trigger	28
4.5	Difference in CMU Towers for CMU, CFT Match	29
4.6	P_t Spectrum CMU Level 1, No CFT, + Other Trigger	29
4.7	Phi of Muon Candidates Passing CMU Level 2	30
4.8	CMU Level 2 Trigger Efficiency	31
5.1	The integrated luminosity per day.	33
5.2	The CDF muon signature for $W \rightarrow \mu + \nu$ decay.	34
5.3	The P_t spectrum of all muon candidates.	35
5.4	The difference, $\delta X = X_{CTC} - X_{CMU}$, in cm.	36
5.5	The difference, $\delta S = S_{CTC} - S_{CMU}$, in radians.	36
5.6	E_{CEM}^T for a cone of size, $\delta R_{Cone} = 0.4$, due to underlying event energy in $W \rightarrow e + \nu$ decays at CDF.	38
5.7	E_{CHA}^T for a cone of size, $\delta R_{Cone} = 0.4$, due to underlying event energy in $W \rightarrow e + \nu$ decays at CDF.	38
5.8	E_{CHA} versus E_{CEM} in a cone of $\delta R_{Cone} = 0.13$ for the muon candidates.	39
5.9	E_t/P_t for the electron W candidates at CDF.	40
5.10	The difference, $\delta X = X_{CDT} - X_{CMU}$, from cosmic ray data.	42
5.11	The difference, $\delta S = S_{CDT} - S_{CMU}$, from cosmic ray data	43
5.12	$ \vec{E}_t $ versus P_t for muon candidates	44
5.13	E_{CEM}^T in a cone of $\delta R = 0.4$ from underlying event.	47
5.14	E_{CHA}^T in a cone of $\delta R = 0.4$ from underlying event.	47
5.15	Probability that a muon passes energy and matching cuts.	48
5.16	P_t spectrum of muon background	49
5.17	E_{CHA} versus E_{CEM} with matching cuts only.	51
5.18	δS versus δX , for muons passing energy cuts only.	52
5.19	Cross section times branching ratio for $W \rightarrow \ell + \nu$ versus c.m. energy.	55

A.1	Location of the central muon chambers within the central calorimeter.	59
A.2	Central muon drift cell.	60
A.3	Central muon tower consisting of four drift cells.	61
A.4	Transverse view of a charged particle in the CDF detector. The inner circle is permeated by a 1.5 Tesla magnetic field while the outer circle represents the lowest plane of central muon sense wires.	62
A.5	Electric field as a function of distance from the sense wire.	64
A.6	Three drift cells in a plane. The sense wire length, L , is 2261 mm. The Fe^{55} sources are used for calibration of charge division.	66
A.7	The sense wire tension is tested by driving the sense wire with a variable frequency and monitoring the in phase and out of phase component of the voltage drop across the 50Ω resistor. The in phase component attains a maximum value while the out of phase component is zero at resonance.	68
A.8	Location in R of the four Fe^{55} sources for a sense wire.	71
A.9	Cosmic ray test stand setup. The top and bottom chambers define the cosmic ray track which is then interpolated into the center test chamber. Efficiencies for each sense wire can then be determined. The scintillators are used in the trigger.	72
A.10	Efficiency as a function of R for a typical sense wire.	73
A.11	Residual errors of the fit to cosmic ray tracks in the ZY plane.	74
A.12	A plot of $\delta = \frac{T_1 - 3T_2 + 3T_3 - T_4}{4}$. The separation of the two peaks in time represents a separation of 4 mm in space.	76
A.13	Residual errors of the fit to cosmic ray tracks in the XY plane.	77
A.14	Pulse height distribution for the muon ADC's.	78
A.15	E_{CHA} vs E_{CEM} for 50 GeV pions.	80
A.16	Punch through probability as a function of incident pion energy for the CDF central calorimeter.	81

A.17 ϕ , in units of CMU cell number, of the particle which passes closest to the beam axis in a punch through event.	82
A.18 Number of tracks per punch through event from 50 GeV pions.	83
B.1 End view of the CDF central detector for event 7605/6279.	87
B.2 Lego plot of the CDF calorimeter for event 7605/6279.	88
B.3 End view of the CDF central detector for event 7589/1116.	89
B.4 Lego plot of the CDF calorimeter for event 7589/1116.	90
B.5 End view of the CDF central detector for event 7604/2861.	91
B.6 Lego plot of the CDF calorimeter for event 7604/2861.	92
B.7 End view of the CDF central detector for event 7787/2063.	93
B.8 Lego plot of the CDF calorimeter for event 7787/2063.	94
B.9 End view of the CDF central detector for event 7787/102.	95
B.10 Lego plot of the CDF calorimeter for event 7787/102.	96
B.11 End view of the CDF central detector for event 7582/2280.	97
B.12 Lego plot of the CDF calorimeter for event 7582/2280.	98
C.1 End view of the CDF central detector for event 7310/468.	100
C.2 Lego plot of the CDF calorimeter for event 7310/468.	101
C.3 End view of the CDF central detector for event 7343/1999.	102
C.4 Lego plot of the CDF calorimeter for event 7343/1999.	103

Chapter 1

Introduction

Because the electroweak theory proved so successful at describing weak interactions, it was important for experimentalists to actually observe the gauge bosons thought to mediate the weak force. Unfortunately, the center of mass energies attainable in fixed target experiments were well below those needed to produce a physical gauge boson. It wasn't until colliding beams of protons and antiprotons became available at CERN that experimentalists could probe the energy domain in the neighborhood of the gauge boson masses. This led to the first observations of the W and Z bosons by UA1 and UA2 experiments at CERN [1].

Similar work was going on at Fermi National Accelerator Laboratory (FNAL) to upgrade the existing fixed target program to provide colliding beams at a center of mass energy beyond that attainable at CERN. In this way, the Collider Detector Facility (CDF) [3] at FNAL would not only provide confirmation of the observations of the gauge bosons at CERN, but extend those observations into a new energy regime.

After an initial checkout run in the fall of 1985, the CDF detector was moved into the FNAL beamline in December of 1986 and began observing proton-antiproton collisions at a world record center of mass energy of 1.8 TeV. Over the course of a four month run, CDF accumulated 35 nb^{-1} integrated luminosity out of a total of 67 nb^{-1} delivered by the accelerator. The peak luminosity achieved by the accelerator was slightly more than $1.4 * 10^{29} \text{ cm}^{-2} \text{ s}^{-1}$.

For the 1987 run, the CDF detector was almost fully instrumented. Surrounding the beam pipe in the central region, was a vertex time projection chamber (VTPC) to aid in both primary and secondary vertex determination. On the outside of the VTPC, was a central tracking chamber (CTC) used to provide track angle and momentum measurements for all charged tracks. The CTC, in turn, was surrounded by central electromagnetic (CEM) and central hadronic calorimetry (CHA) to provide neutral particle detection and to discriminate between leptons and hadrons. Completing the central portion of CDF, is the central muon system (CMU) built by the University of Illinois group. In addition to the central detector, CDF had forward tracking chambers, calorimetry and forward muon system for particle detection at low angles to the beam line.

In what follows is a description of some of the theoretical predictions concerning the gauge bosons at 1.8 TeV, a description of the CDF detector used in the observation of the gauge bosons, and some results from the 1987 run.

Chapter 2

Theory

In the 1930's, Enrico Fermi first attempted to characterize weak interactions with a point contact diagram. Consider neutrino-electron scattering as in figure 2.1. The cross section, $\sigma_{\nu e}$, is purely s-wave and is calculated to be $\sigma_{\nu e} = s * G_F^2/\pi$, where s is the Mandelstam s variable and G_F is the Fermi constant. Unitarity requires that a purely s-wave cross section be bounded from above such that $\sigma_{\nu e} < 2\pi/s$. Unitarity is therefore violated in collisions with a center-of-mass energy, $\sqrt{s} > \sqrt{\sqrt{2}\pi/G_F} \simeq 617$ GeV. It was noted however, that much better behavior was obtained by introducing an intermediate vector boson (IVB), analogous to the photon, to mediate the weak interaction. Moreover the short range nature of the weak force indicated that this boson should be massive. The resultant "theory" still violated unitarity but at much higher

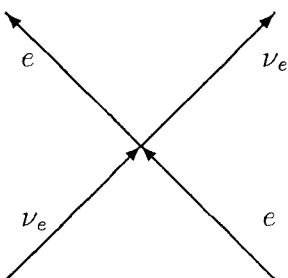


Figure 2.1: Contact Diagram for Weak Interactions

center-of-mass energies. The Weinberg-Salam model (WS) successfully incorporated this massive mediator into a fully re-normalizable, consistent theory describing all electromagnetic and weak interactions. This theory required the existence of both a charged (W) and neutral (Z) mediator of the weak force. The masses of the W and Z are related by

$$M_W = \frac{e}{2^{\frac{5}{4}} G_F^{\frac{1}{2}} \sin \theta_w} \simeq \frac{38.65}{\sin \theta_w} \text{ GeV}/c^2 = M_Z \cos \theta_w$$

where θ_w is the weak mixing angle and e is the electronic charge.

Neutrino-nucleon and neutrino-electron scattering experiments [4] measure the weak mixing angle to be

$$\sin^2 \theta_w = 0.224 \pm 0.015 \pm (0.012)$$

where the last error represents the average theoretical uncertainties in the measurement.

The predicted masses for the W, Z from the WS theory are then

$$M_W = 81.7 \text{ GeV}/c^2$$

$$M_Z = 92.7 \text{ GeV}/c^2$$

Such massive particles are only accessible at colliding beam accelerators and were discovered at CERN in 1983 [1] using colliding beams of protons and antiprotons. The measured masses for the W and Z were found to be [2]

$$M_W = 83.5^{+1.1}_{-1.0} \pm 2.7 \text{ GeV}/c^2$$

$$M_Z = 93.0 \pm 1.4 \pm 3.0 \text{ GeV}/c^2$$

where the first errors are statistical and the second errors are systematic errors. The mass measurements then yield a value of

$$\sin^2 \theta_w = 1 - \frac{M_W^2}{M_Z^2} = 0.194 \pm 0.032$$

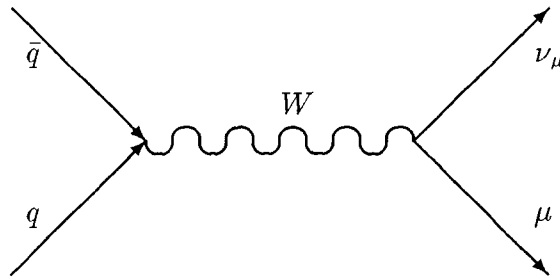


Figure 2.2: Drell-Yan Production of W Bosons

A more precise measurement of $\sin^2 \theta_w$ can be derived from

$$\sin^2 \theta_w = \left(\frac{38.65}{M_W} \right)^2 = 0.214 \pm 0.006 \pm 0.015$$

where the second error is the systematic error. These measurements are in excellent agreement with the predictions of the WS theory.

The production mechanism for W, Z production at hadron colliders is predominately "quark fusion" in which a quark from the proton and an anti-quark from the anti-proton fuse to produce a vector boson [5]. Figure 2.2 is the lowest order diagram for this process. Higher order corrections to figure 2.2 have been calculated [6]. At Tevatron energies of 1.8 TeV, there should be about a four-fold increase in the production cross section for W bosons over the measured value [1] at CERN energies of 0.63 TeV.

The plots throughout the rest of this chapter are derived from Monte Carlo studies using ISAJET [7] version 6.1. Figure 2.3 shows the expected rapidity distribution of the W's where rapidity, Y, of a particle is defined as

$$Y = -\frac{1}{2} \ln \frac{E - P_{\parallel}}{E + P_{\parallel}}$$

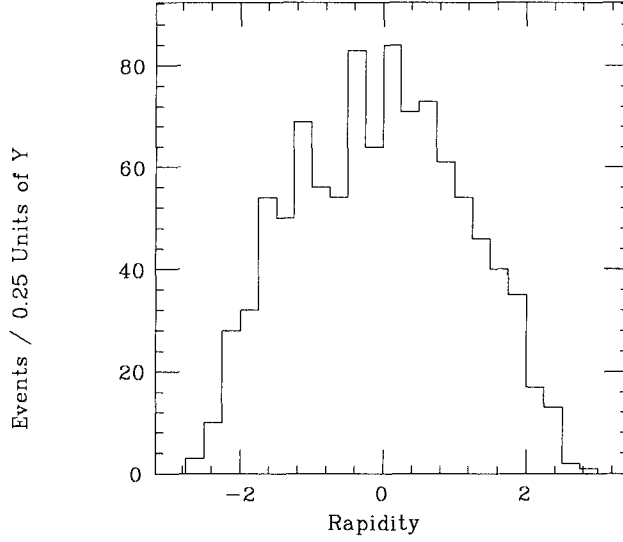


Figure 2.3: Rapidity distribution of W's at 1.8 TeV

One way of observing IVB's experimentally is in the lepton decay channel.

$$W^{\pm} \rightarrow \ell^{\pm} + \nu_{\ell}$$

$$Z^0 \rightarrow \ell + \bar{\ell}$$

where $\ell = \mu, e$. For W decay, the neutrino is observed as a transverse energy imbalance when the vector sum of transverse energy deposition in the detector calorimeter is calculated. Only the P_t of the neutrino is measured. The muons from W decay appear as high P_t tracks in the central tracking detector and leave minimum ionising energy in the calorimetry. After passing through the calorimetry, muons leave a track in the muon chambers. The expected P_t distribution of the muons (neutrinos) is given in figure 2.4. They are seen to have very high transverse momentum, with 87% having a $P_t > 20$ GeV/c. Figure 2.5 is a plot of the pseudorapidity distribution for the muons (neutrinos) from W decay. Pseudorapidity, η , is defined to be $\eta = -\log \tan \frac{\theta}{2}$ where θ is the polar angle of the lepton with respect to the beam axis. For massless particles, η is equivalent to rapidity, Y . The extent of the central muon chambers in η is indicated by the dashed lines in figure 2.5.

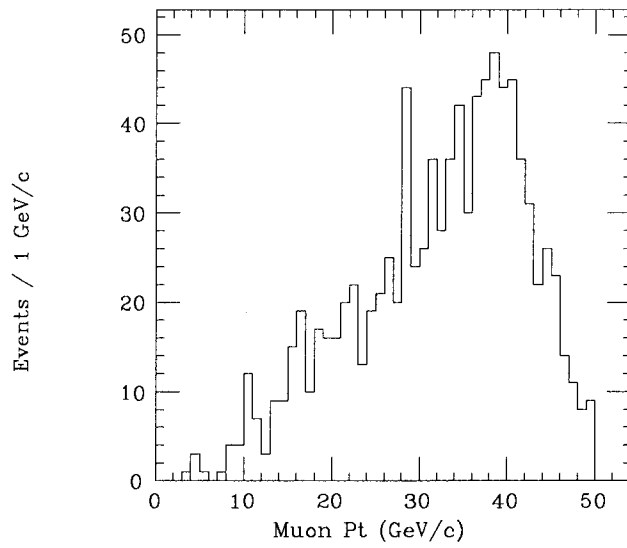


Figure 2.4: Muon P_t distribution of the muons from W decay

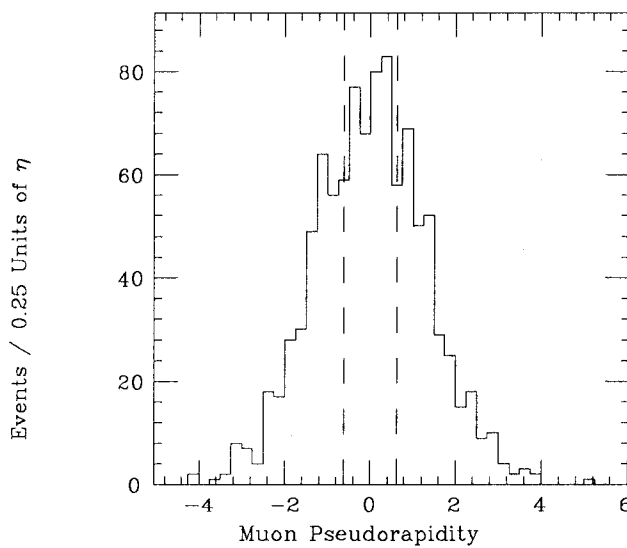


Figure 2.5: Pseudorapidity of the muons from W decay

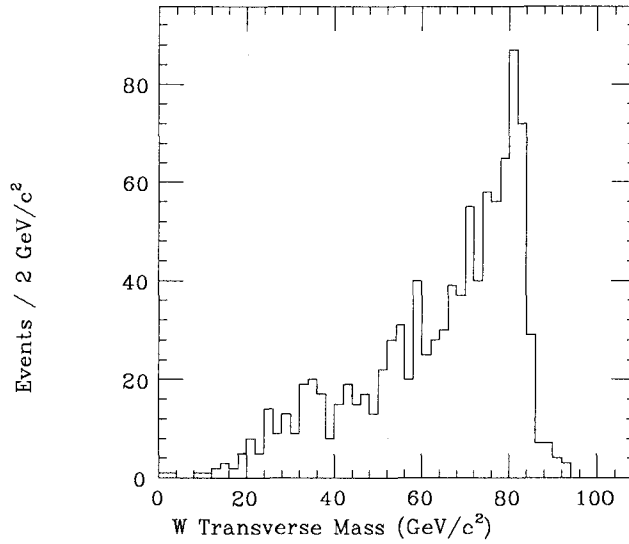


Figure 2.6: Transverse mass of W's

Because the longitudinal component of the neutrino momentum is not known, the invariant mass of the W cannot be measured directly. The "transverse mass", M_t , of the W is defined to be

$$M_t = \sqrt{2(E_t^\mu E_t^\nu - \vec{P}_t^\mu \cdot \vec{P}_t^\nu)}$$

where E_t is the transverse energy and \vec{P}_t is the transverse momentum vector. Figure 2.6 is a plot of the expected transverse mass distribution for W's when the mass of the W is $M_W = 83.0 \text{ GeV}/c^2$.

The W, Z's provide a laboratory for studying quarks within the proton. If quark 1 carries momentum fraction, X_1 , of the parent proton and quark 2 carries momentum fraction, X_2 , of its parent antiproton, then four momentum conservation requires that

$$X_1 X_2 S = M_W^2$$

where \sqrt{S} is the c.m. energy of the proton/anti-proton system and M_W is the mass of the W.

The longitudinal momentum of the W is given by

$$P_{\parallel}^W = (X_1 - X_2) \times \sqrt{S}/2$$

so that

$$X_1 = \frac{P_{\parallel}^W + \sqrt{(P_{\parallel}^W)^2 + M_W^2}}{\sqrt{S}}$$

A measurement of P_{\parallel}^W requires a measurement of the longitudinal momentum of the neutrino, P_{\parallel}^{ν} , which in turn is measured by constraining the lepton, neutrino invariant mass to be M_W and solving for the longitudinal component of the neutrino momentum.

P_{\parallel}^{ν} is then given by

$$P_{\parallel}^{\nu} = \frac{P_{\parallel}^{\mu}(M_W^2 + 2P_t^{\mu}P_t^{\nu} \cos \phi) \pm P_{\mu} \sqrt{(M_W^2 + 2P_t^{\mu}P_t^{\nu} \cos \phi)^2 - 4P_t^{\mu 2}P_t^{\nu 2}}}{2P_t^{\mu 2}}$$

where P_t denotes transverse momentum, ϕ is the angle between the muon and neutrino transverse momentum vectors, P_{\parallel} is the longitudinal momentum component, and P_{μ} is the muon momentum. P_{\parallel}^{ν} may have two solutions so that $P_{\parallel}^W = P_{\parallel}^{\nu} + P_{\parallel}^{\mu}$ also may have two solutions. The ambiguity can be resolved in most cases either because one solution is unphysical or because one solution is highly improbable when compared with the expected parton distribution functions which have been evolved from lower c.m. energies. The quark momentum distribution functions for the proton can therefore be measured by using the $W \rightarrow \mu + \nu$ decay as a tag.

As the quarks fuse to produce the IVB, they may radiate a gluon and impart a transverse momentum kick to the IVB. Because the radiating quark is unlikely to be very far off mass shell, the Q^2 of the quark-gluon pair is close to zero. For high momentum gluons, the gluon is emitted in the direction of the radiating quark. Therefore W + jet events should be characterised by a forward jet and a soft W transverse momentum spectrum. The transverse momentum of the W's is plotted in figure 2.7 and indicates that W's are usually produced with very little transverse momentum.

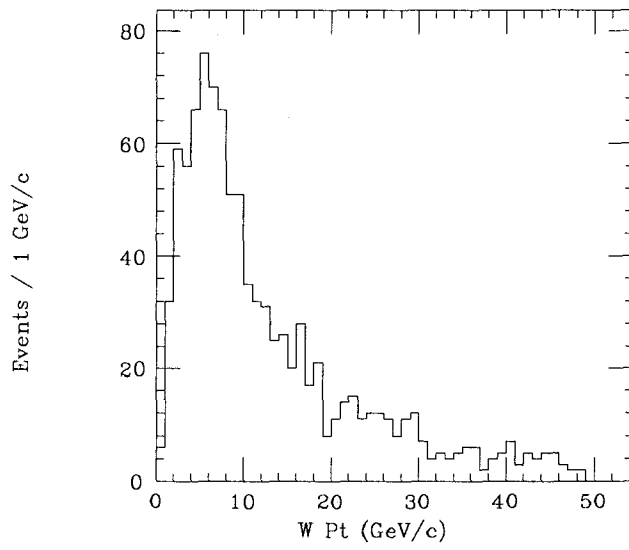


Figure 2.7: Transverse momentum distribution of W's at 1.8 TeV

Chapter 3

Detector

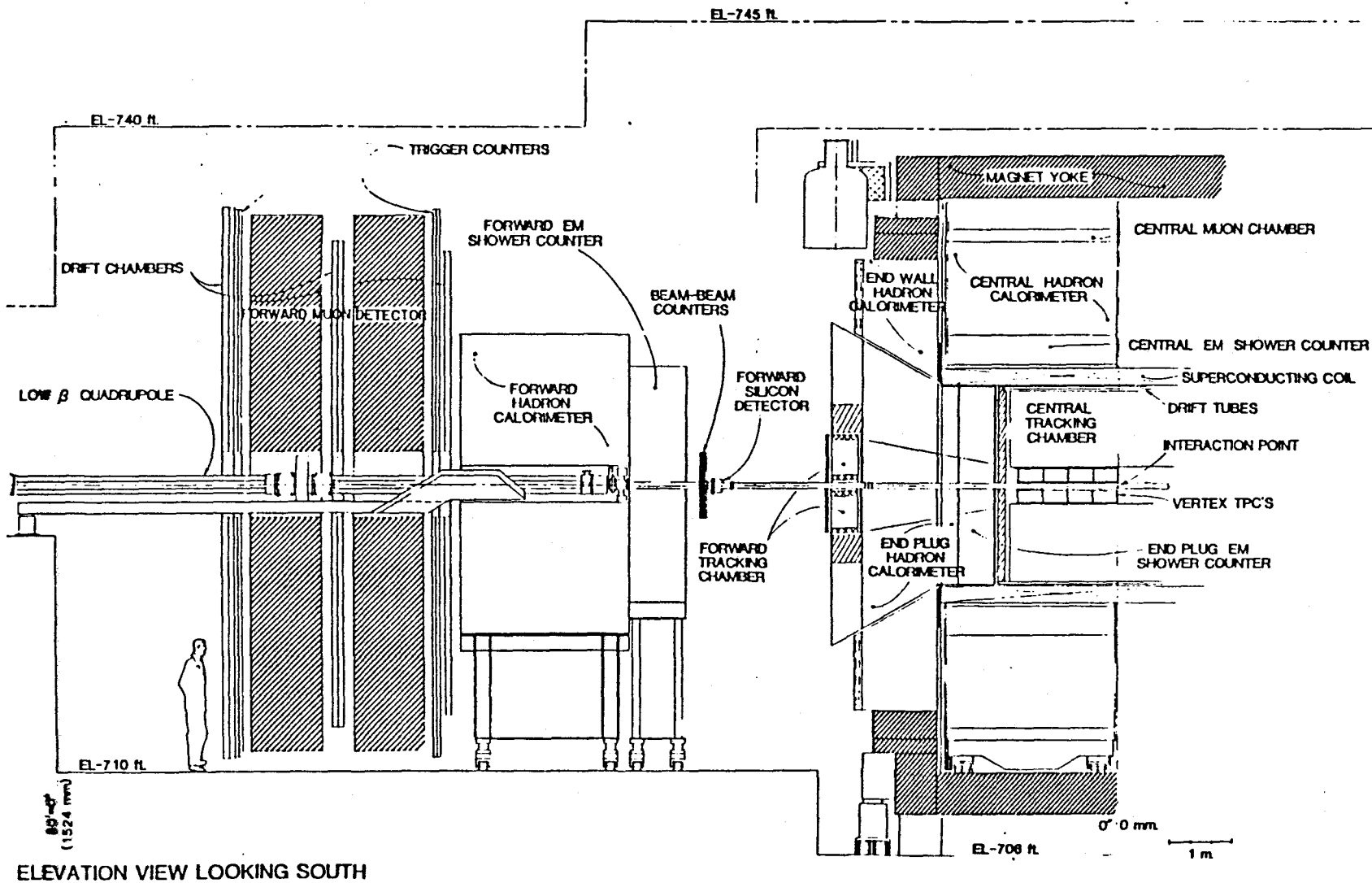
The CDF detector [3] is shown in figure 3.1. The CDF polar coordinate system has the +Z axis along the beam line in the direction of the proton beam. The azimuthal angle, ϕ , is defined with $\phi = 90^\circ$ in the vertically upward direction while the polar angle, θ , is defined with $\theta = 0^\circ$ along the +Z axis.

The CDF detector consists of a cylindrical central detector which covers the angular region, $10^\circ < \theta < 170^\circ$ in polar angle and forward/backward detectors consisting of electromagnetic and hadronic calorimetry and muon toroids for the angular region $2^\circ < \theta < 10^\circ$. The focus will be on the central detector.

On the outside of the beam pipe, which is a 25.4 mm in radius Be tube, are eight small vertex time projection chambers (VTPC) which provide information on the event vertex.

3.1 Central Tracking Chamber

Surrounding the VTPC at a radial distance of 272 mm is the central tracking chamber (CTC), which provides spatial and momentum measurement of all charged tracks. Permeating the CTC, which extends out to a radial distance of 1380 mm, is a 1.5 Telsa axial magnetic field. The CTC consists of nine super layers of sense wires. Five of these super layers consist of 12 axial sense wires provide tracking information in the



ELEVATION VIEW LOOKING SOUTH

Figure 3.1: CDF Detector.

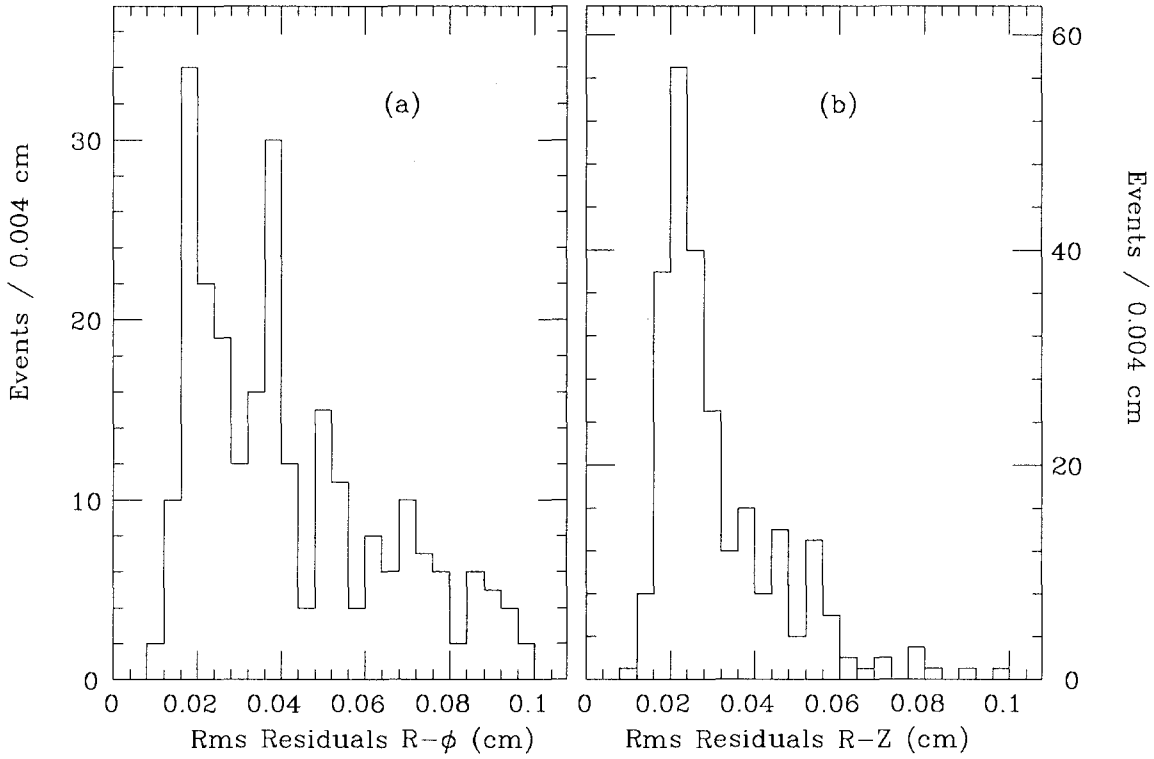


Figure 3.2: CTC Residuals (a) R- ϕ Fit (b) R-Z Fit

R- ϕ plane. The remaining four stereo super layers consisting of 6 sense wires tilted by $\pm 3^\circ$ relative to the beam axis provide tracking information in the R-Z plane.

Figure 3.2 (a, b) are plots of the CTC rms residual errors for the track fit in the R- ϕ plane and for the fit in the R-Z plane respectively. For tracks with $P_t > 10$ GeV/c and small impact parameters, the helical equation for the track in the R- ϕ plane reduces to a linear equation of the form

$$\phi = \phi_0 - \frac{eRB}{2P_t}$$

where ϕ_0 is the azimuthal angle of the tangent to the track at the beam line, e is the charge, B is the magnetic field strength, and ϕ is the azimuthal angle of the track at a

radial distance, R . A least squares fit for ϕ_0 and $eB/(2P_t)$ yields an error estimate for P_t as a function of the R - ϕ fit residuals, $\sigma_{R-\phi}^{rms}$.

$$\frac{\delta P_t}{P_t} = \frac{2 P_t \sigma_{R-\phi}^{rms}}{e B} \sqrt{\frac{\sum_i R_i^2}{\sum_i R_i^2 \sum_i R_i^4 - (\sum_i R_i^3)^2}}$$

where R_i is the radial distance of the i^{th} axial sense wire. By assuming that the 60 axial sense wires are evenly spaced radially within the CTC gives

$$\frac{\delta P_t}{P_t} = 0.0444 P_t \sigma_{R-\phi}^{rms} = 0.0013 P_t$$

over a pseudorapidity range of $|\eta| < 1$ when $\sigma_{R-\phi}^{rms} = 0.03$ cm.

The fit in the R - Z plane reduces to an equation of the form

$$Z \simeq R \cot \theta + Z_0 \quad (3.1)$$

where Z_0 is the Z of the track at the point of closest approach to the beam axis. The rms residual error in the R - Z fit from figure 3.2 (b) is about 0.025 cm so that the uncertainty in an individual Z measurement is

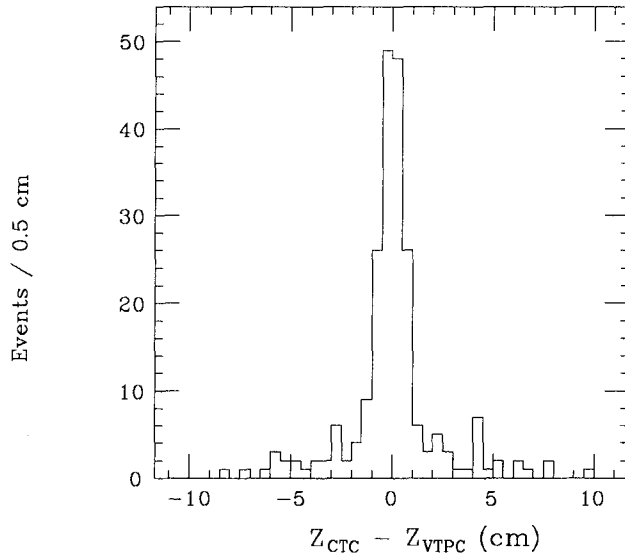
$$\sigma_{R-Z}^{rms} = 0.025 / \sin 3^\circ = 0.5 \text{ cm}$$

A least squares fit to equation 3.1 gives for the error on Z_0 and $\cot \theta$

$$\sigma_{Z_0} = 0.56 \sigma_{R-Z}^{rms} = 0.3 \text{ cm}$$

$$\sigma_{\cot(\theta)} = 0.006 \sigma_{R-Z}^{rms} = 0.003$$

where the 24 stereo wires were assumed to be uniformly distributed radially within the CTC. Figure 3.3 is a plot of the difference in Z between a CTC track extrapolated to the beam axis, and the vertex as found by the VTPC. Figure 3.3 shows a gaussian peak with non-gaussian tails. The full width half maximum of the peak is 1.5 cm so that $\sigma_{Z_{CTC}-Z_{VTPC}} = 0.6$ cm which is consistent with the CTC and VTPC resolution in quadrature.

Figure 3.3: $Z_{CTC} - Z_{VTPC}$ at the Beam Axis

3.2 Central Drift Tubes

On the outside of the CTC are three layers of central drift tubes (CDT) which were constructed at the University of Illinois. Each tube is 12.7 mm in diameter and provides both $R-\phi$ and $R-Z$ tracking information. Figure 3.4 (a,b) are plots of the difference between the CTC and the CDT in ϕ and Z . Again the difference is consistent with the resolutions of the CDT and CTC in quadrature. Surrounding the CDT is the 0.85 radiation lengths of the superconducting coil.

3.3 Central Calorimeter

After the coil, come the central electromagnetic (CEM) and central hadronic (CHA) calorimeters. They are divided into projective towers of size 0.1 in η and 15° in ϕ . The CEM consists of lead and scintillator sandwich and extends from 1676 mm to 2076 mm in radial distance from the beam axis. The energy resolution of the CEM is $\delta E_{CEM}/E_{CEM} = 0.14/\sqrt{E_{CEM}}$. Figure 3.5 is a plot of the CEM energy deposition for 57

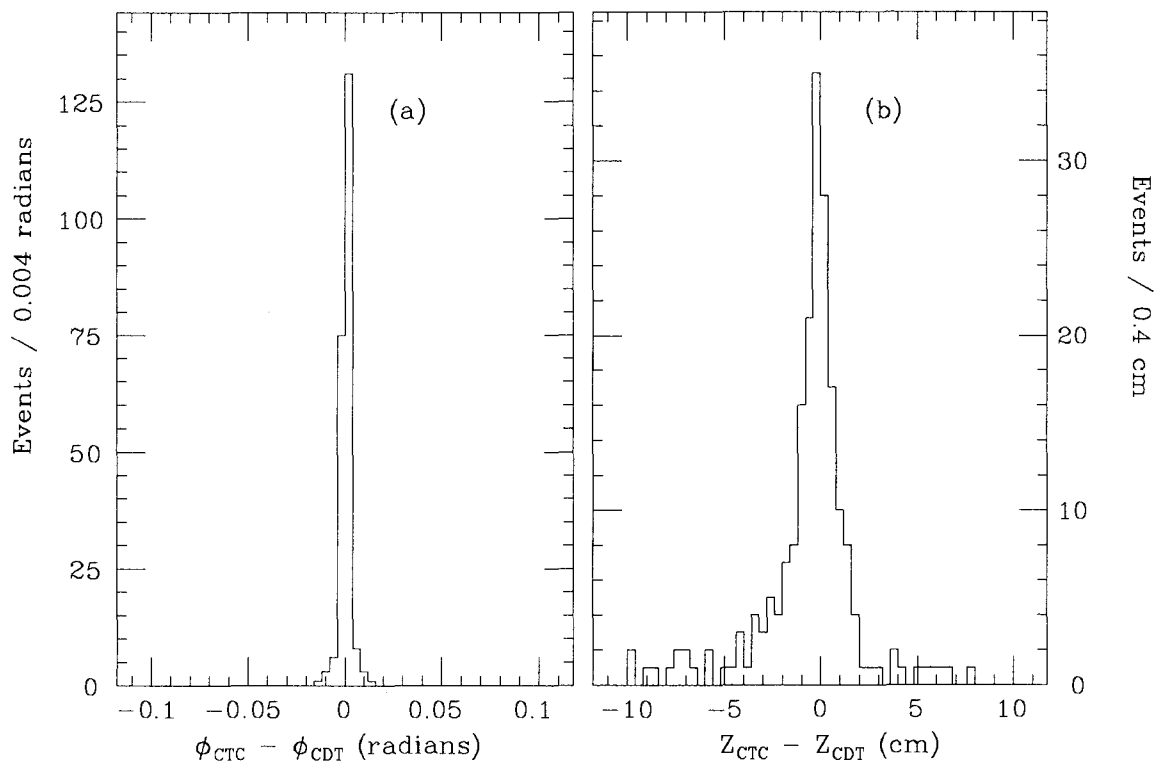


Figure 3.4: (a) $\phi_{CTC} - \phi_{CDT}$ (b) $Z_{CTC} - Z_{CDT}$

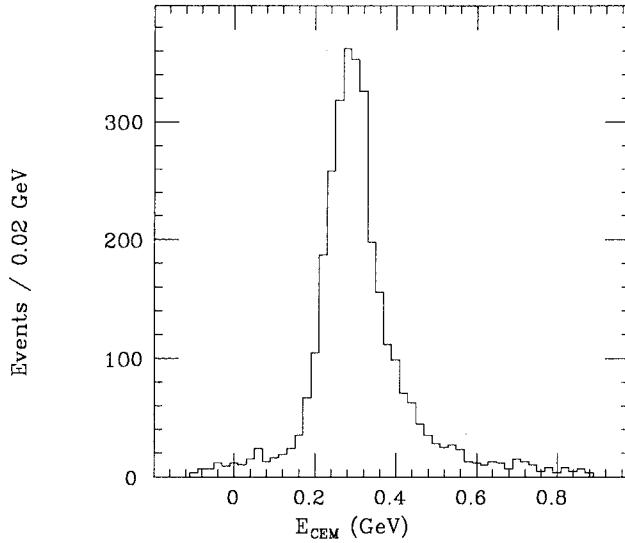


Figure 3.5: CEM Energy Deposition for 57 GeV/c Muons

GeV/c muons in a testbeam. The energy deposition, E_{CEM} , due to muons is Landau distributed with a mean of about 0.3 GeV.

The CHA consists of steel and scintillator sandwich and extends from 2076 mm to 3487 mm in radial distance. The resolution of the CHA is $\delta E_{\text{CHA}}/E_{\text{CHA}} = 0.78/\sqrt{E_{\text{CHA}}}$. Figure 3.6 is a plot of the CHA energy deposition for 57 GeV/c muons in a testbeam. The mean energy deposition, E_{CHA} , in the CHA calorimeter due to muons is about 2.1 GeV.

3.4 Central Muon Chambers

On the outside of the CHA calorimeter at a radial distance of 3487 mm from the beam axis are the central muon chambers (CMU). A complete description of the CMU chambers may be found in reference [8] which has been included as Appendix A. The central calorimetry provides 5.3 absorption lengths of shielding from penetrating hadrons [9]. The CMU detector was entirely constructed at the University of Illinois and consists of 144 chambers of drift cells. Three chambers are bolted together into a single unit atop

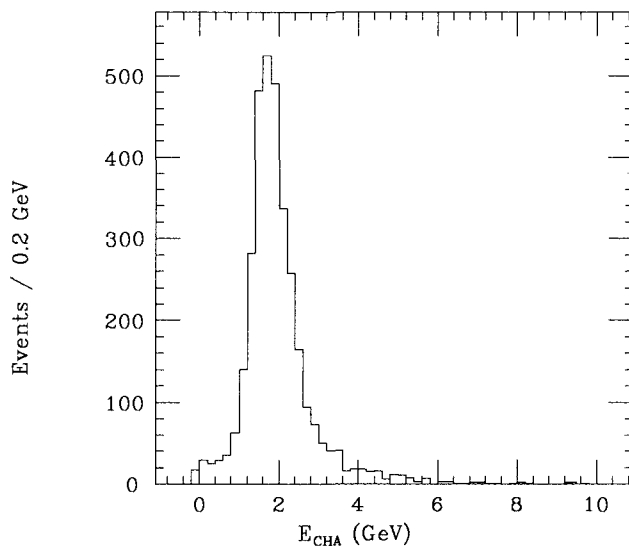


Figure 3.6: CHA Energy Deposition for 57 GeV/c Muons

a central calorimeter wedge and cover 12.6° in phi. Each chamber contains four layers of cells with four cells per layer. Figure 3.7 shows an end view of a typical chamber. A typical drift cell is rectangular in shape and is 63.5 mm in width and 25.4 mm in height. Running down the length of the cell, is a $50\ \mu\text{m}$ diameter stainless steel sense wire. The cells operate in the limited streamer mode which provides an amplification factor of 10^7 . The output of each sense wire is read by a channel of a RABBIT ADC/TDC card [10]. The arrival of the signal triggers a clock which records the arrival time of the signal while the size of the signal is stored as charge on a capacitor. Figure 3.8 is a plot of the arrival times for typical events from $\bar{p}p$ data. The edge of the distribution in figure 3.8 at 26600 TDC counts represents CMU hits occurring directly at the sense wire while events from the trailing edge at 14700 TDC counts are CMU hits for which the drift electrons traversed the half width of the cell. The difference between the two edges is about 11900 TDC counts or about 690 ns. This is consistent with a maximum average drift distance of 32 mm and a drift velocity of $50\ \text{mm}\ \mu\text{s}^{-1}$. The arrival time of the signal determines how far from the sense wire the charged track passed. The size of the signal

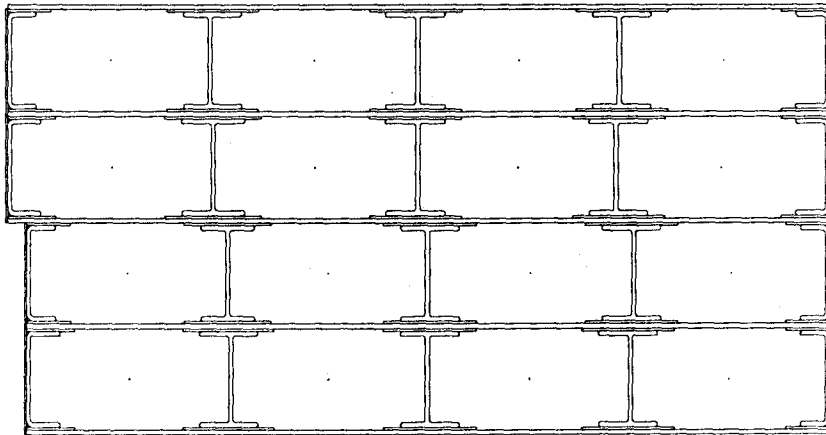


Figure 3.7: End View of CMU Chamber

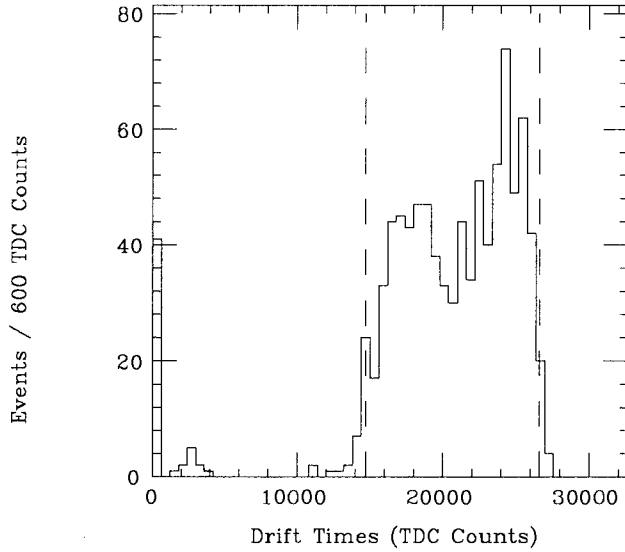


Figure 3.8: CMU Drift Times

determines the location of the track along the sense wire by use of the method of charge division. In a layer of four drift cells, each sense wire is connected at one end to another sense wire which is separated from the first by an intervening drift cell. Because the sense wire is resistive, the size of the signal measured at each end depends linearly on the location of the track along the sense wire pair.

The sense wires from alternating layers lie on a radial line pointing back to the interaction point (figure 3.7). The two sets of two sense wires from alternating layers are offset from each other by 2 mm at the radial midpoint of the chamber so that the track ambiguity in phi can be resolved. Because the sense wires lie along radial lines from the interaction point, the track angle with respect to the sense wires can be measured by comparing the arrival times of hits from alternating layers in the muon chambers. The track angle in turn is related to the transverse momentum of the particle since the solenoidal B field deflects tracks away from a radial line by an amount $\delta\phi = eL^2B/2DP_t$ where L is the radius of the solenoidal field, B is the field magnitude, and D is the radial distance to the muon chambers. The central muon chambers can therefore provide a

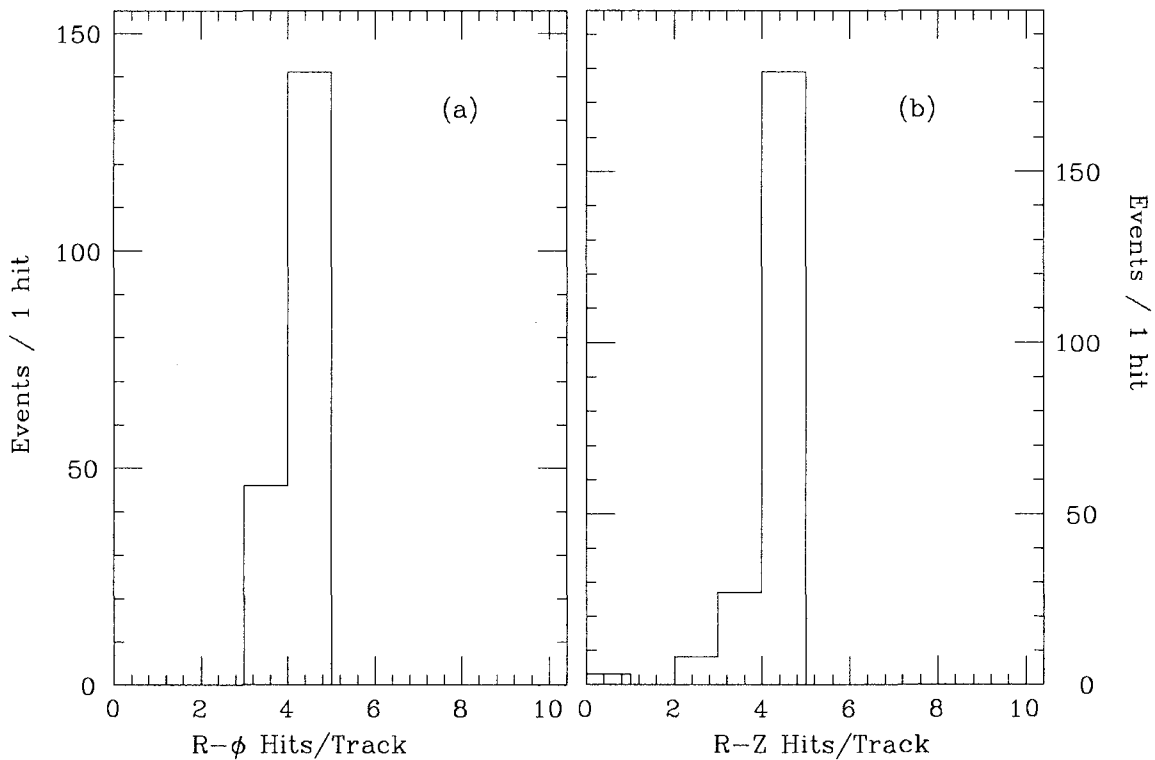


Figure 3.9: Number Hits per CMU Track (a) R- ϕ Fit (b) R-Z Fit

measurement of the transverse momentum of the muons.

CMU tracks are reconstructed independently in the R- ϕ plane, using TDC information, and in the R-Z plane by the use of charge division information. Figure 3.9 (a) is a plot of the relative number of three and four hit tracks reconstructed in the R- ϕ plane while 3.9 (b) is the same plot for CMU tracks reconstructed in the R-Z plane. The ratio of the number of three hit tracks to four hit tracks is a measure of the chamber efficiency since if there are four layers of cells, the probability of having three out of four hits is $P_3 = 4\epsilon^3(1 - \epsilon)$ and $P_4 = \epsilon^4$ so that the ratio is $4(1 - \epsilon)/\epsilon$. From figure 3.9, the single cell efficiency in R- ϕ is seen to be about 92%. The expected single cell efficiency should

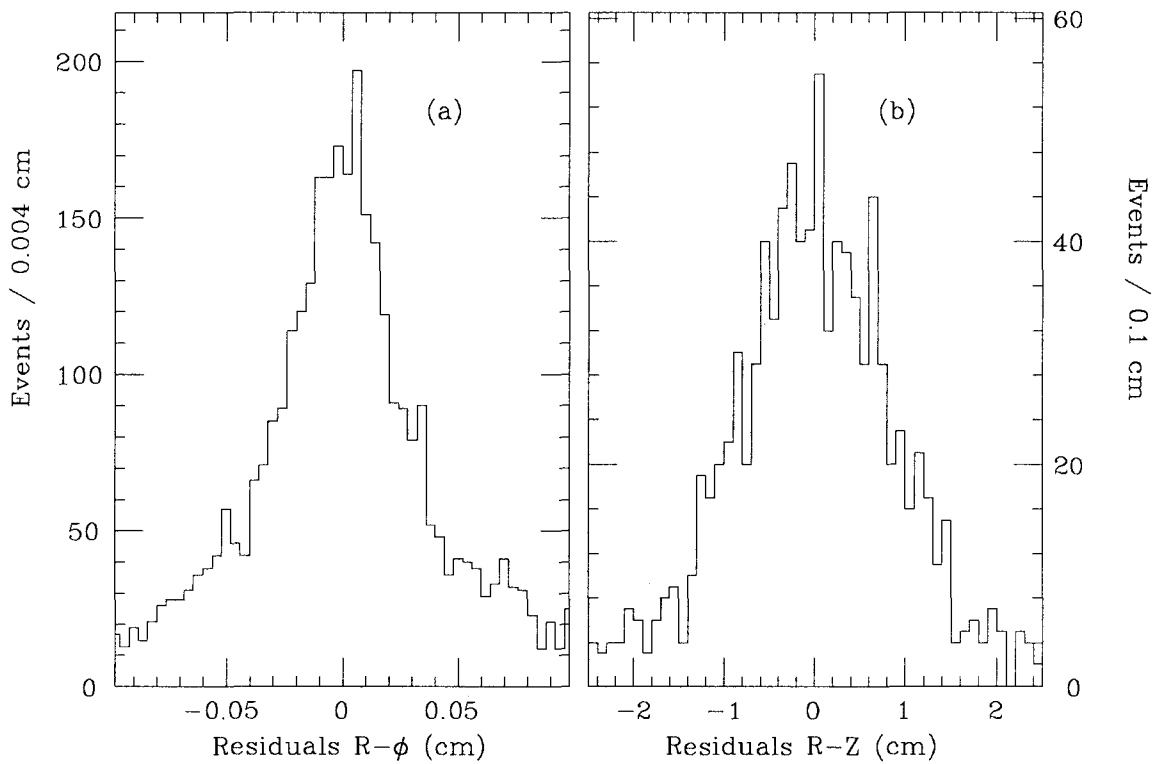


Figure 3.10: CMU Track Residuals (a) $R-\phi$ Fit (b) $R-Z$ Fit

be about 98% and the lower actual efficiency is in part, due to TDC readout problems when the ADC channels overflow.

The CMU track residuals for both the $R-\phi$ fit and for the $R-Z$ fit are given in figure 3.10 (a) and (b). From figure 3.10, the CMU resolution is seen to be $250 \mu\text{m}$ in the $R-\phi$ plane and 0.6 mm in the $R-Z$ plane.

Chapter 4

Trigger

The CDF trigger [11] consists of three stages of increasing sophistication. A level 1 trigger decision is required between beam crossings, which for 1987 was every $7 \mu\text{s}$. A level 2 decision may take several beam crossings, while the level 3 trigger is a software trigger which may take up to a second.

4.1 Central Muon Level 1 Trigger

The Level 1 central muon trigger [12] requires that the signals from hits on alternating layers in the chamber arrive within a programmable time difference of one another. If an infinite momentum track passed through the chamber, it would do so on a radial line passing through the interaction point and the time delay between hits in the CMU chamber would be zero for the two sense wires which lie along the radial line. Real particles undergo multiple scattering while traversing the 110 cm equivalent of steel between the muon chambers and the interaction point. The multiple scattering deflection is approximately gaussian distributed with a sigma of $0.12/P$ radians in the $R-\phi$ plane, where P is the momentum. Multiple scattering therefore introduces inefficiency into the CMU level 1 trigger since some particles might be scattered into large angles with respect to the CMU sense wires and so not pass the timing coincidence. Figure 4.1 is a plot of the calculated efficiency as a function of P for two possible level 1 coinci-

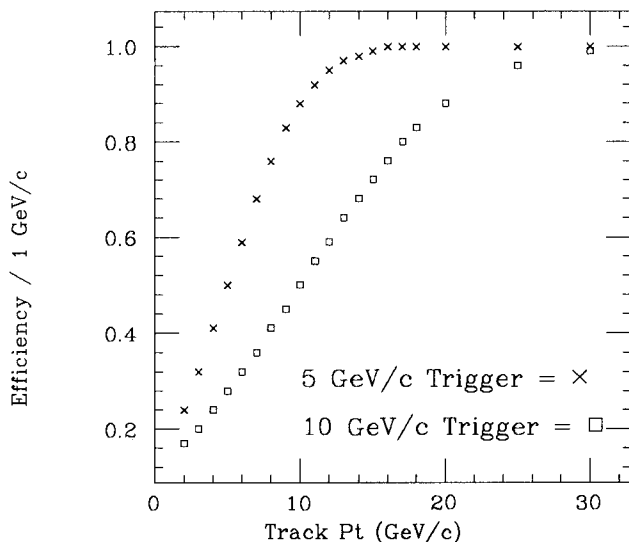


Figure 4.1: CMU Level 1 Efficiency

dence thresholds. From figure 4.1, the level 1 trigger efficiency is 50% for tracks with transverse momentum, P_t , when the coincidence threshold is set to select tracks with transverse momentum P_t .

4.2 Central Muon Level 2 Trigger

Once an event has passed the CMU level 1 trigger, a central fast track processor [13] (CFT) finds all high momentum central tracks in the CTC and provides momentum, charge, and phi information to a Fastbus device called the Muon Matchbox (MMB). Within the MMB are lookup tables which predict the location of the muon hits based on the central track information and multiple scattering contributions. Bits corresponding to the most likely location of the muon hits within a programmable error margin are enabled in the Fastbus MU2T cards. The level 1 CMU trigger bits are also passed to the MU2T cards where a coincidence is made. Information for those tracks passing the coincidence are fed to the Level 2 Trigger Processors [11] via the Cluster Bus. Within the level 2 processors, additional information from the event such as jet activity and other

calorimetry information can be combined with the muon information. A level 2 trigger decision is then made based on the combined muon and underlying event information.

4.3 Trigger Performance

For the 1987 run, much of the level 2 hardware was not available. The MU2T and MMB cards were available as was the CFT track processor, but the level 2 processors did not exist. The muon trigger, consisting of the CMU + CFT track match was modified to run at level 1 speeds i.e. between beam crossings. For events with very many tracks, there was not enough time for all tracks to be sent from the CFT to the MMB. This led to trigger inefficiencies of at most 30% [13].

In what follows, CMU level 1 refers to the CMU level 1 trigger only while CMU level 2 will denote the CMU level 1 matched with a CFT track and the match occurring at level 1 times.

4.3.1 CMU Level 1

The CMU level 1 hardware may be checked by looking at events for which there was another trigger besides a central muon trigger. The 1987 data consisted of approximately equal integrated luminosity from a CMU level 1 threshold of 5 GeV/c and a CMU level 1 threshold of 10 GeV/c. The 5 GeV/c threshold requires that the drift electrons, in cells from alternating layers of the CMU chamber, arrive at the sense wires within about 35 ns of each other while the 10 GeV/c threshold has a gate width of about 17 ns. Since the data is a combination of these two thresholds, there should be no events in which the CMU level 1 trigger fired with a TDC difference greater than 35 ns and conversely, there should be no events in which the CMU level 1 failed to fire with a TDC difference less than about 17 ns. Figure 4.2 is a plot of the TDC difference for muon hits from alternating layers which caused the CMU level 1 trigger to fire (a) and

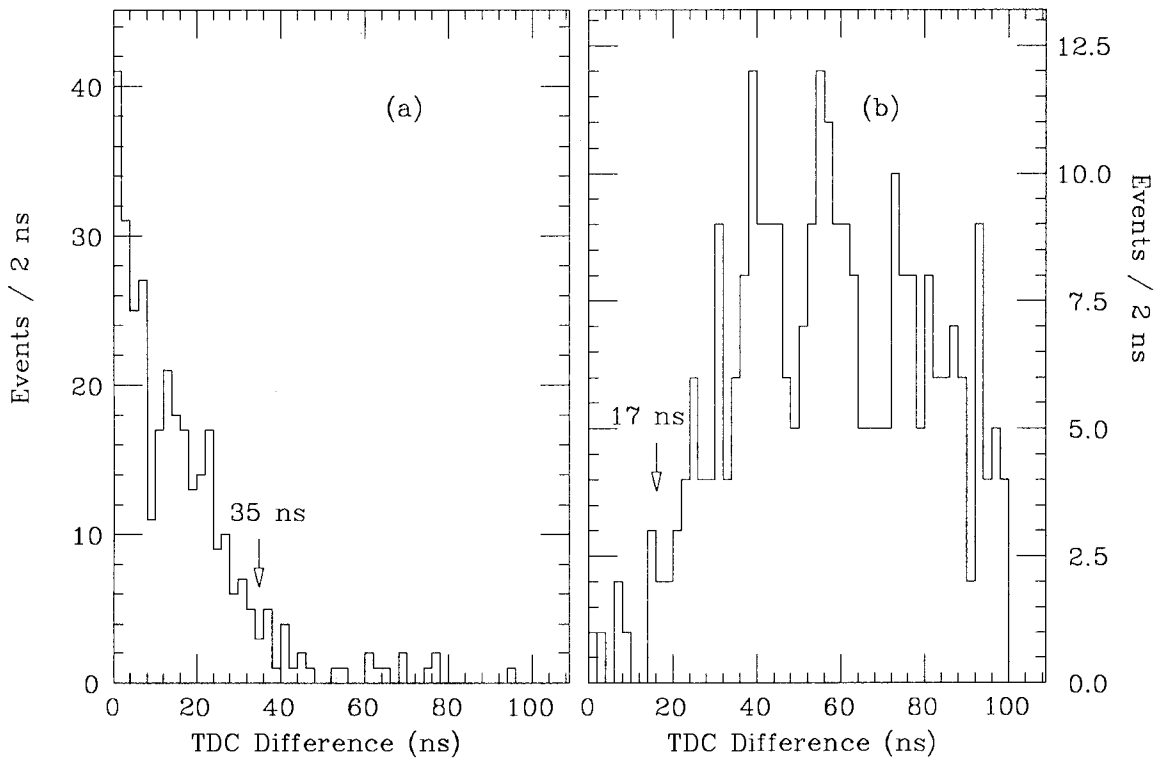


Figure 4.2: TDC Difference (ns) CMU Level 1 (a) True (b) False

the TDC difference of hits for which the CMU level 1 trigger didn't fire (b). There are very few events in (a) with a TDC difference above 35 ns corresponding to the 5 GeV/c trigger threshold. In (b) there are very few events with TDC difference less than the 17 ns cutoff corresponding to the 10 GeV/c threshold. The conclusion is that the timing hardware for CMU level 1 was performing correctly. This is a necessary but not sufficient condition for successful operation of the CMU level 1 trigger since it may still be selecting tracks with the wrong transverse momentum due to chamber misalignment or uncertainties in multiple scattering. In principle, figure 4.1 may be extracted from the data by again looking at events for which there was an alternate trigger to CMU Level 2.

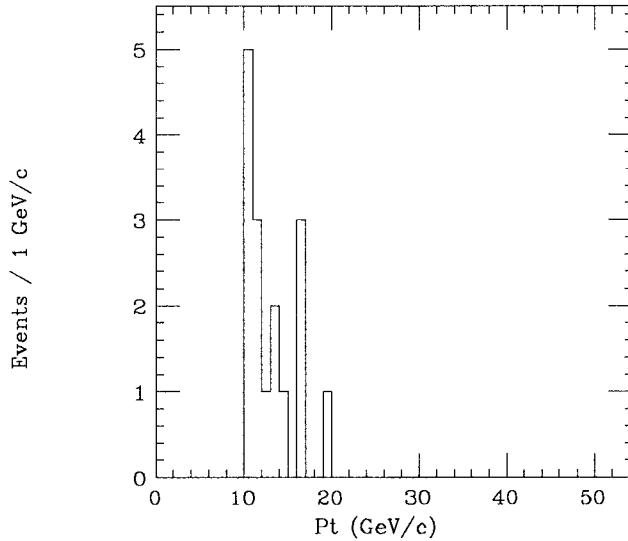


Figure 4.3: P_t Spectrum with CMU Level 2 + Other Trigger

Figure 4.3 is a plot of the P_t spectrum for tracks which generated a CMU level 2 trigger and also some other trigger. Figure 4.4 is the P_t spectrum of tracks which passed the CFT threshold but failed to fire the CMU level 1 trigger. In the case where CMU level 1 failed to fire, there may be events in which a particle from a hadron shower escaped the central calorimeter and entered the muon chambers (interactive punch through). To remove such events, the muons in these two figures were required to be consistent with minimum ionising particles with CEM energy deposition, $E_{CEM} < 1.0$ GeV, and CHA energy deposition, $E_{CHA} < 3.0$ GeV, and have a CMU, CTC track match within 3 cm in intercept difference and within 0.030 radians in slope difference in the $R-\phi$ plane (see chapter 5 for definitions of slope and intercept). The bin by bin ratio of events from figure 4.4 to the events from figure 4.3 is then the measured CMU Level 1 inefficiency as a function of track P_t . Unfortunately the statistics are too low to make this measurement meaningful.

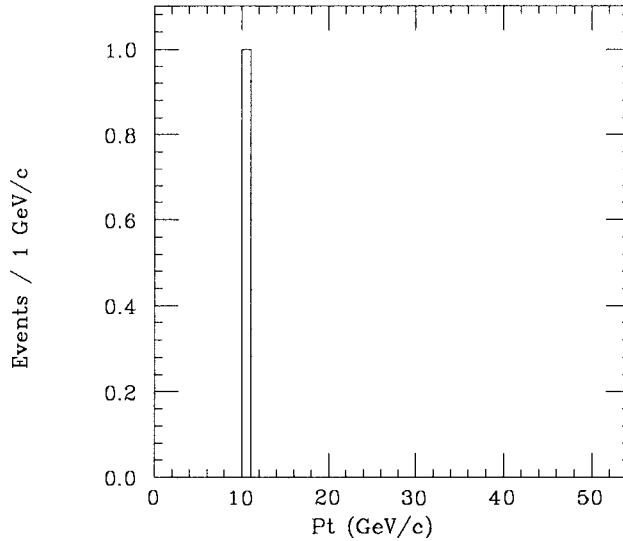


Figure 4.4: P_t Spectrum with CFT Only + Other Trigger

4.3.2 Central Fast Track Processor

The CFT processor hardware can also be checked with the data. Figure 4.5 shows the phi difference between the CFT predicted muon hits and the actual muon hits. The margin of error allowed by the MMB for the phi match was set to 0.26 radians for this data. This error margin can be seen in figure 4.5 since an error of 0.26 radians translates to a difference of ± 6 muon towers.

The CFT track processor efficiency can be checked by looking at events for which there was another trigger and a CMU level 1 trigger. Figure 4.3 again provides the normalization while figure 4.6 is a P_t spectrum for inefficient CFT tracks. Again a bin by bin ratio of events from 4.6 to events from figure 4.3 gives the CFT track processor inefficiency as a function of track P_t . The inefficiency measurement is again curtailed by limited statistics.

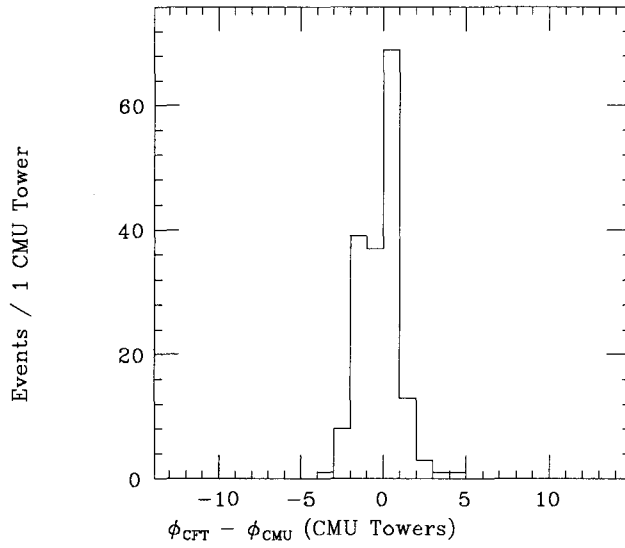
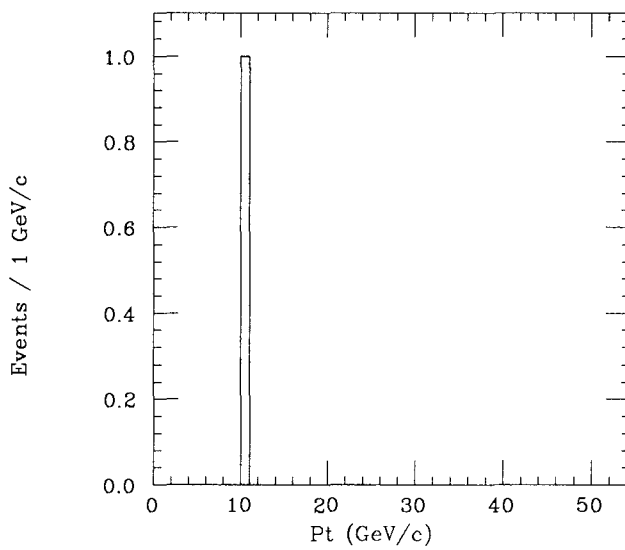


Figure 4.5: Difference in CMU Towers for CMU, CFT Match

Figure 4.6: P_t Spectrum CMU Level 1, No CFT, + Other Trigger

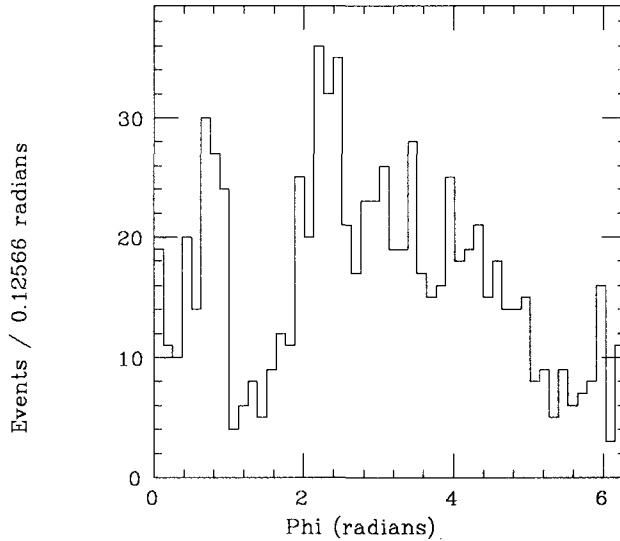


Figure 4.7: Phi of Muon Candidates Passing CMU Level 2

4.3.3 CMU Level 2

Finally since limited statistics prevent measurement of the overall CMU trigger efficiency, the trigger efficiency is estimated as a function of P_t by the average of the two curves in figure 4.1 multiplied by a factor which is derived from figure 4.7 and contains the inefficiency due to both CMU hardware problems and timing problems in matching the CMU hits with a CFT track. Above 15 GeV/c the CFT track processor should be fully efficient (neglecting timing problems). Figure 4.7 is a plot of the phi distribution of level 2 triggers. Figure 4.7 shows a depleted region close to $\phi = \pi/2$ which is caused by CMU chamber hardware problems. There is also a depleted region for $\phi > 4.9$ radians which is due to the timing problems with the CMU, CFT match. The total number of events excluding those in the depleted regions is 686 in a phi region of size 4.15 radians. The total number of events in the depleted region is 137 in a region of size 2.13 radians so that the efficiency due to the phi non-uniformity of the trigger is

$$E_{\text{Trig}} = (4.15 * 823)/(686 * 6.28) = 0.79$$

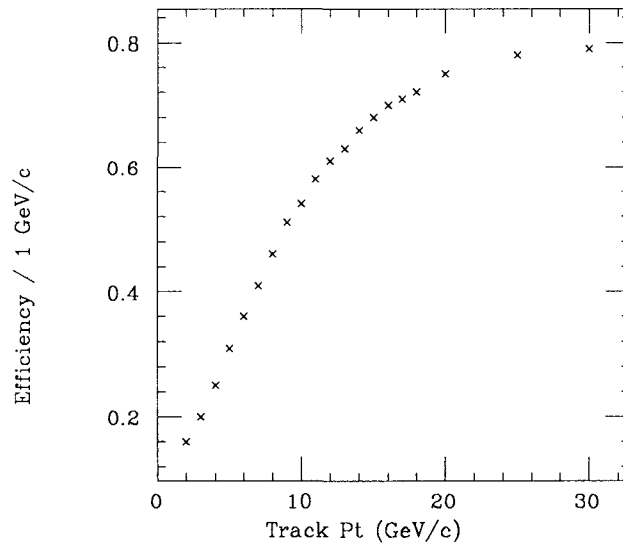


Figure 4.8: CMU Level 2 Trigger Efficiency

Figure 4.8 gives the overall estimated trigger efficiency as a function of P_t . Figure 4.8 is only valid for $P_t > 15$ GeV/c since below 15 GeV/c, the CFT processor efficiency is less than one.

Chapter 5

Analysis

The integrated luminosity per day delivered by the accelerator is shown in figure 5.1. The accelerator provided 67 nb^{-1} of which about 35 nb^{-1} was logged to tape. The peak luminosity reached $1.4 \times 10^{29} \text{ cm}^{-2}\text{s}^{-1}$. The following analysis will treat the $27.2 \pm 4.1 \text{ nb}^{-1}$ of data for which the CMU trigger was believed to be operating reliably.

Figure 5.2 depicts a high P_t muon from a W decay as it traverses the detector. The signature of high P_t muons in the CDF detector is a stiff track in the CTC, minimum ionising energy deposition in the calorimeters, and a muon track which matches the extrapolated central track to within multiple scattering errors. The following sections describe the details of the cuts applied to the data.

5.1 Require Muon $P_t > 10 \text{ GeV}/c$

Approximately 500 raw data tapes were analysed. The CTC track reconstruction code provided tracks which were reconstructed in the R - ϕ plane and in the R - Z plane. These 3-d tracks were required to satisfy the following conditions. Out of the maximum number of hits in the CTC possible along the track, more than 50% had to be used in the track. In addition there had to be at least one track segment comprising more than 66% of the available sense wires in an axial layer other than layer 0 and in a stereo layer. There were several very loose cuts on the quality of the track match with the

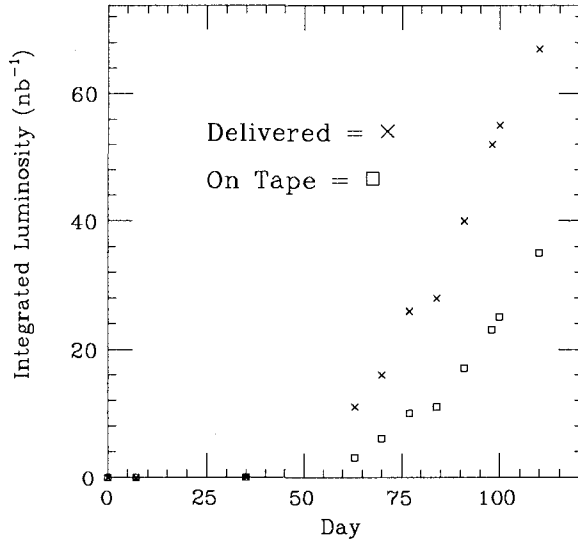


Figure 5.1: The integrated luminosity per day.

interaction vertex as well. These tracks were then filtered by requiring that the track have $P_t > 10$ GeV/c and be the best possible match to the CMU muon track within multiple scattering errors. The muon candidates were also required to be consistent with minimum ionising particles with energy deposition $E_{CEM} < 1$ GeV in the CEM calorimeter and $E_{CHA} < 3$ GeV energy deposition in the CHA calorimeter. Figure 5.3 is the P_t spectrum for the candidate muon events. It is seen to be a steeply falling spectrum with a long tail which should contain the $W \rightarrow \mu + \nu$ sample.

The expected multiple scattering error for 110 cm of steel equivalent in the intercept match, $\delta X = X_{CTC} - X_{CMU}$, between the CTC and CMU tracks is $\sigma_{\delta X} = 12/P$ cm where P is the momentum of the particle. The intercept, X_{CTC} , is defined as the distance of the point, from the radial line passing through the center of the muon chamber, at which the CTC track intersects the lowest layer of CMU sense wires in the $R-\phi$ plane. Similarly the multiple scattering error in the slope match, $\delta S = S_{CTC} - S_{CMU}$, between the CTC and CMU tracks is $\sigma_{\delta S} = 0.12/P$ radians. The slope, S_{CTC} , is defined as the tangent of the angle between the CTC track and the radial line passing through the center of the muon chamber in the $R-\phi$ plane. Figure 5.4 and figure 5.5 are plots of δX

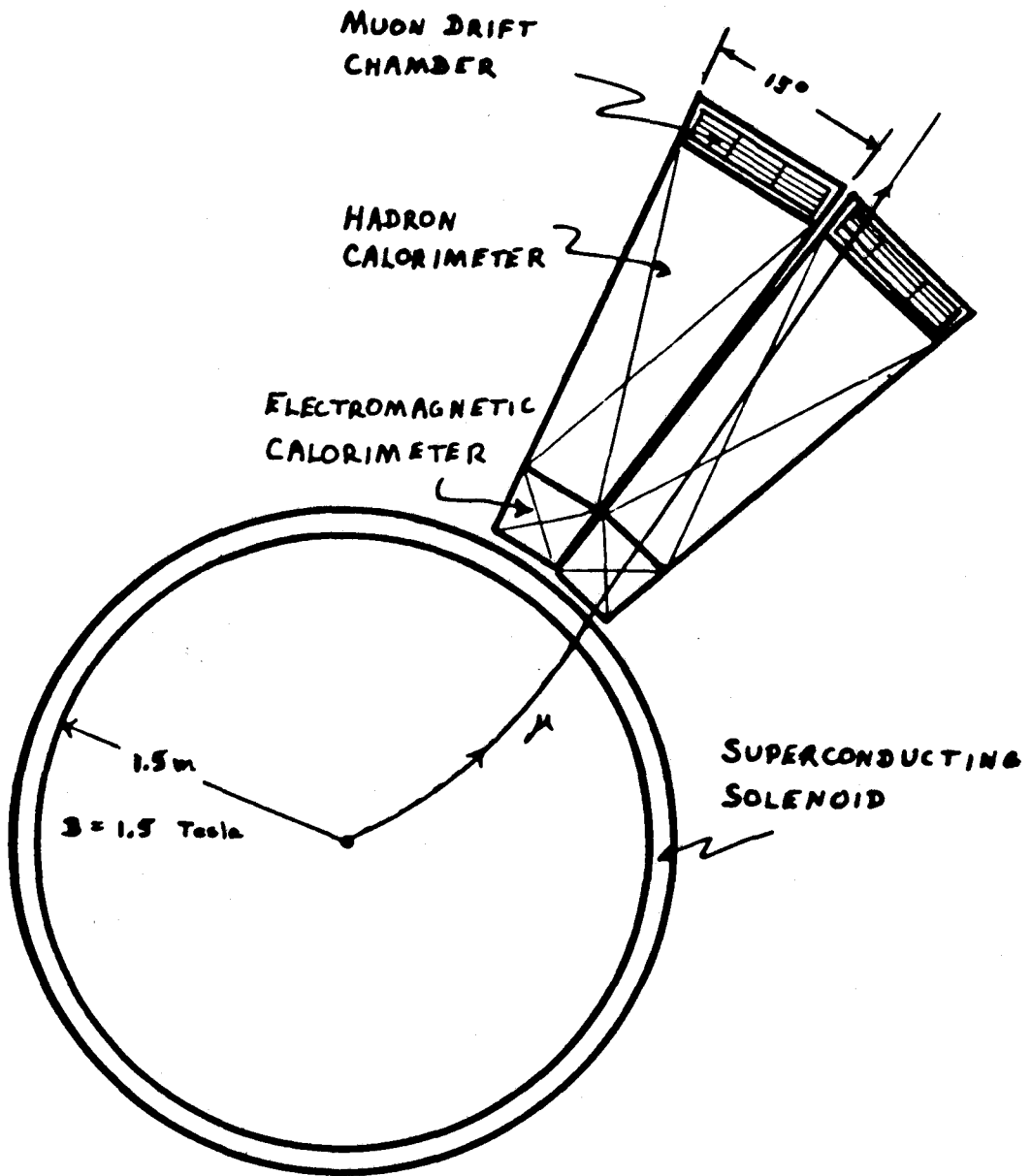


Figure 5.2: The CDF muon signature for $W \rightarrow \mu + \nu$ decay.

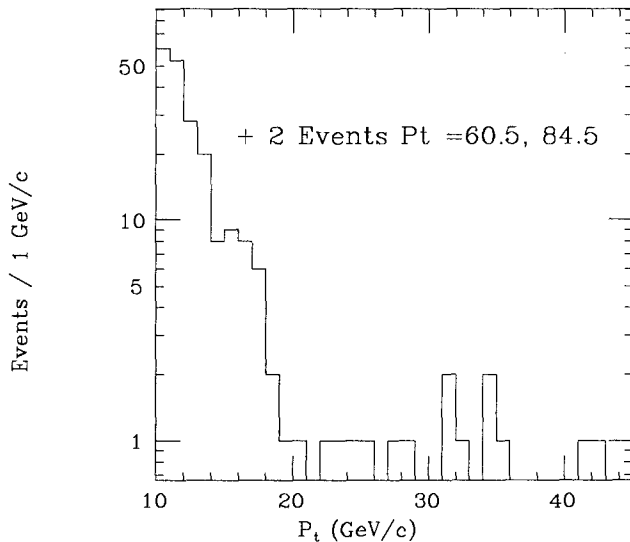


Figure 5.3: The P_t spectrum of all muon candidates.

and δS for the candidate muons. The peaks in these figures can be treated as gaussian with non-gaussian tails so that the errors, $\sigma_{\delta X}$ and $\sigma_{\delta S}$, can be derived by

$$\sigma_{\delta X} = 0.42 \times W_{\text{fwhm}} = 1.4 \text{ cm}$$

$$\sigma_{\delta S} = 0.42 \times W_{\text{fwhm}} = 0.017 \text{ radians}$$

where in each case, W_{fwhm} , is the full width of the peak at half maximum. These errors are consistent with the multiple scattering of 10 GeV/c particles.

5.2 Remove Cosmic Rays

Cosmic rays continually bombard the CDF detector and might coincide with a beam crossing. If the cosmic ray passes close to the interaction point, it could mimic a high P_t di-muon event. Due to hardware problems with the CDF detector, a cosmic ray might also mimic a W decay. The Fermi Lab main ring passes over the top of the B0 collision hall and so the top of the CDF detector was continually showered by low energy particles produced by the antiproton production cycle. This required that the voltage of the top 8 wedges (out of 48) of CMU chambers be reduced. Figure 4.7 shows the

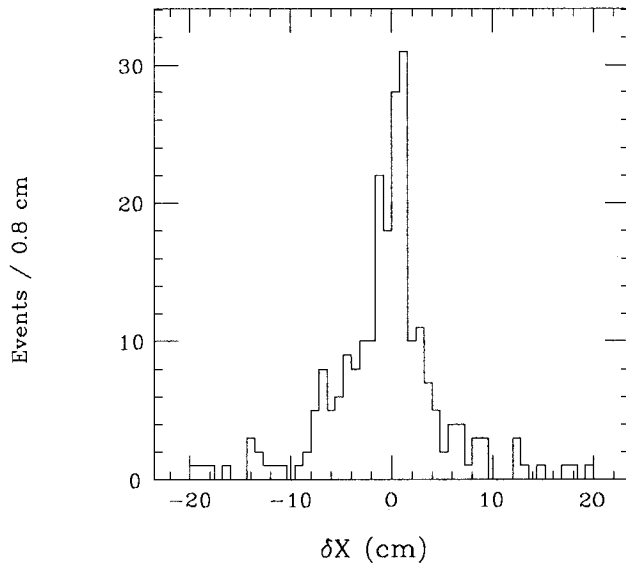


Figure 5.4: The difference, $\delta X = X_{\text{CTC}} - X_{\text{CMU}}$, in cm.

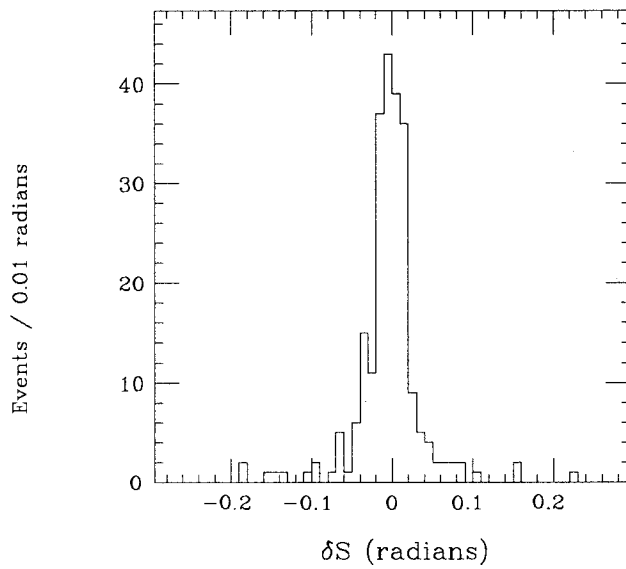


Figure 5.5: The difference, $\delta S = S_{\text{CTC}} - S_{\text{CMU}}$, in radians.

hole at $\phi = \pi/2$ due to the reduced chamber voltage. Cosmic rays could pass through the top of the detector without leaving a muon track, pass near the interaction vertex, and exit through the bottom of the detector leaving a muon track. These events would then mimic a $W \rightarrow \mu + \nu$ event. An event was therefore cut if there were only two central tracks with $P_t > 10$ GeV/c and the cosine of the angle between these two tracks was less than -0.98 . Both tracks also had to leave less than 5 GeV of energy in the calorimeters.

5.3 Require Muon $P_t > 20$ GeV/c

Decay kinematics [6] imply that the P_t of the muon from W decay should be peaked toward $M_W/2$. Figure 2.4 indicates that 87% of the muons from W decay should have a $P_t > 20$ GeV/c. Figure 5.3 indicates that any potential background is a steeply falling function of P_t and should have died away for $P_t > 20$ GeV/c. Therefore muons from W decay were required to have $P_t > 20$ GeV/c.

5.4 Require Muon to be Isolated

For real W events, there should be very little transverse energy surrounding the muon in a cone of radius, $\delta R_{\text{Cone}} = \sqrt{\delta\phi^2 + \delta\eta^2} = 0.4$, due to energy deposition from the underlying event. The electron candidate W decays at CDF were studied to determine this contribution from the underlying event. The transverse energy in a cone of 0.4 about the electron was subtracted from the transverse energy in a cone of radius 1.0 about the electron. The difference represents the energy in 5.25 cones of radius 0.4 so that the average transverse energy from the underlying event could be calculated for electrons from W decay. Figure 5.6 is a plot of the EM transverse energy in a cone of 0.4 which lies adjacent to the cone which surrounds the electron candidates for W decay as measured at CDF [14]. Figure 5.7 is the same plot for hadronic energy. The electron

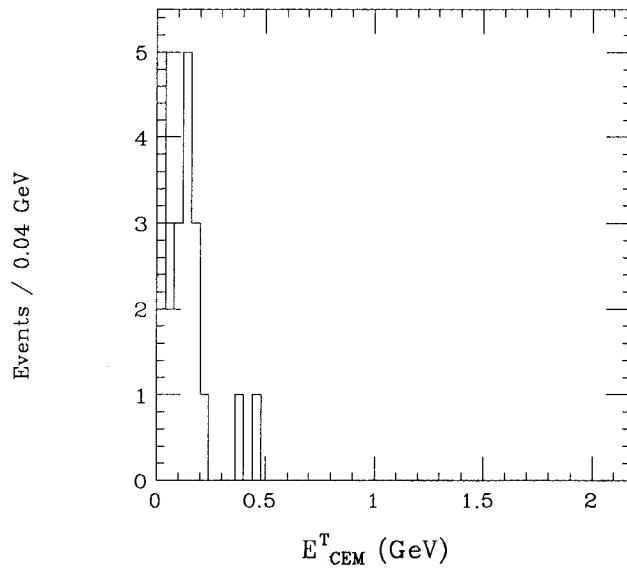


Figure 5.6: E_{CEM}^T for a cone of size, $\delta R_{\text{Cone}} = 0.4$, due to underlying event energy in $W \rightarrow e + \nu$ decays at CDF.

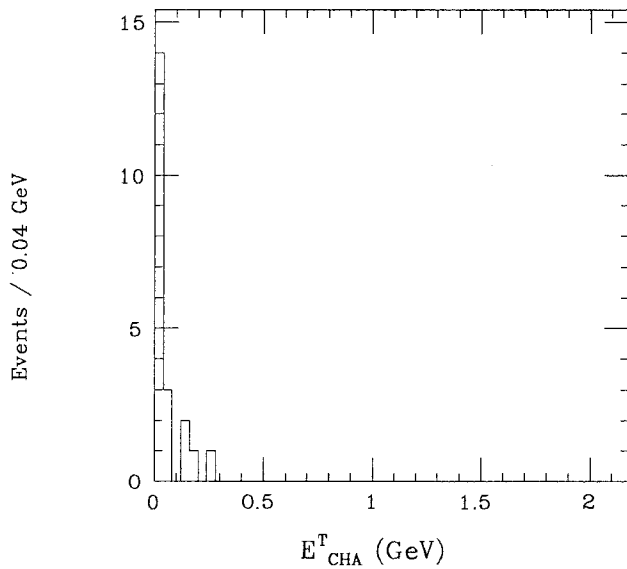


Figure 5.7: E_{CHA}^T for a cone of size, $\delta R_{\text{Cone}} = 0.4$, due to underlying event energy in $W \rightarrow e + \nu$ decays at CDF.

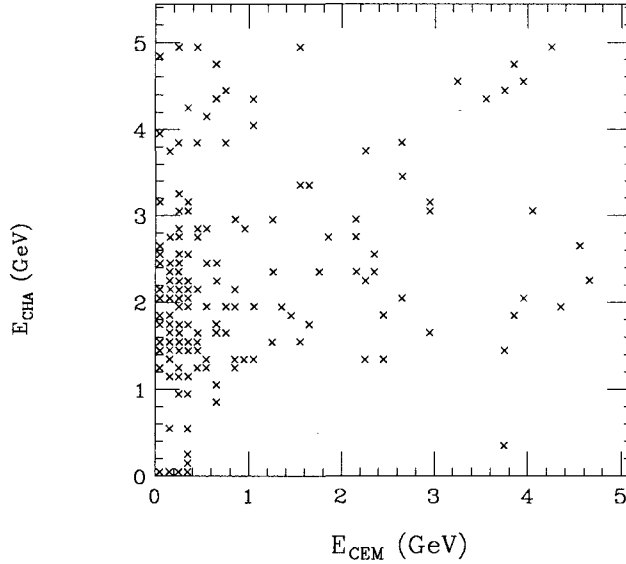


Figure 5.8: E_{CHA} versus E_{CEM} in a cone of $\delta R_{\text{Cone}} = 0.13$ for the muon candidates.

is seen to be well isolated from any underlying event energy so it is reasonable to expect that the muon candidates should be similarly isolated.

5.5 Require Muon to be Minimum Ionising

Because the muons from W events are isolated from the underlying event, the calorimetry signature should match that of test beam muons. Figure 3.5 shows that, for isolated stiff muons in a test beam, $E_{\text{CEM}} > 0.5$ GeV is highly unlikely while figure 3.6 shows that $E_{\text{CHA}} > 3.5$ GeV is also unlikely. Figure 5.8 is a scatter plot of E_{CHA} versus E_{CEM} for candidate muons in a cone of radius, $\delta R_{\text{Cone}} = 0.13$. The CTC, CMU matching cuts of $\delta X < 3$ cm and $\delta S < 0.030$ radians were applied. A cut was made on calorimetry energy requiring that $E_{\text{CHA}} < 3.0$ GeV and that $E_{\text{CEM}} < 1.0$ GeV.

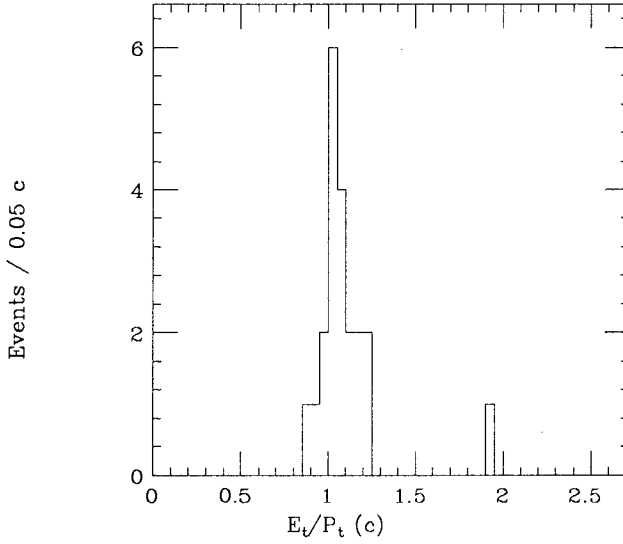


Figure 5.9: E_t/P_t for the electron W candidates at CDF.

5.6 Require CTC, Muon Track Match

There are three sources of error in matching a CTC track with a muon track. Multiple scattering is one contribution with an error on $\delta X = X_{\text{CTC}} - X_{\text{CMU}}$, of

$$\sigma_{\delta X} < 0.6 \text{ cm}$$

for muons above 20 GeV. A second source of mismatch is due to mis-measurement of the central track P_t . Since the central track is extrapolated through the central magnetic field, an error in P_t can generate a CTC, CMU mismatch at the muon chambers. An estimate for the error in the P_t measurement of the central tracks can be obtained from a plot of E_t/P_t for the electron W candidates as in figure 5.9. The error in the energy measurement of 40 GeV electrons in the CEM calorimeter is

$$\delta E_{\text{CEM}} = 0.14 \sqrt{E_{\text{CEM}}} = 0.9 \text{ GeV}$$

so that the error in E_t/P_t from energy mis-measurement alone is 0.02. An upper bound for the P_t resolution of the CTC can be found by attributing all of the width of the

E_t/P_t plot to P_t mis-measurement. The error derived from figure 5.9 is then

$$\sigma_{E_t/P_t} = 0.42 \times W_{\text{fwhm}} = 0.042 = E_t \delta P_t / P_t^2$$

For 40 GeV electrons with $E_t \simeq 40$ GeV,

$$\delta P_t / P_t = 0.001 P_t$$

The error in δX due to momentum mis-measurement is then

$$\sigma_{\delta X} = eLB(D - L/2) \delta P_t / P_t^2 = 184.4 \times 0.001 = 0.2 \text{ cm}$$

where $L = 1476$ mm is the inner radius of the solenoid, $eB = 4.545 \times 10^{-3} \text{ cm}^{-1} \text{ GeV}/c$ is the charge times the field strength, and $D = 3487$ mm is the radial distance to the muon chambers. A final source of error in matching CMU tracks with CTC tracks comes from CMU chamber misalignment with respect to the CTC. Cosmic ray data was taken using the CMU chambers and the central drift tubes (CDT). The cosmic rays which passed close to the beam axis were reconstructed using the CDT detector. This track was then extrapolated to the two muon chambers struck and compared to the reconstructed muon track. Figure 5.10 is a plot of the difference, $\delta X = X_{\text{CDT}} - X_{\text{CMU}}$, between the CDT track and the muon track in the R - ϕ plane. The cosmic rays undergo multiple scattering as they pass through the detector so that the width of the peak in figure 5.10 is in part due to multiple scattering. An upper bound on the error in δX due to CMU chamber misalignment can be derived from figure 5.10 and is found to be

$$\sigma_{\delta X} = 0.42 \times W_{\text{fwhm}} = 1.5 \text{ cm}$$

Combining the three matching errors in quadrature yields an upper bound on the CTC, CMU intercept matching error in the R - ϕ plane of

$$\sigma_{\delta X} = \sqrt{0.6^2 + 0.2^2 + 1.5^2} = 1.6 \text{ cm}$$

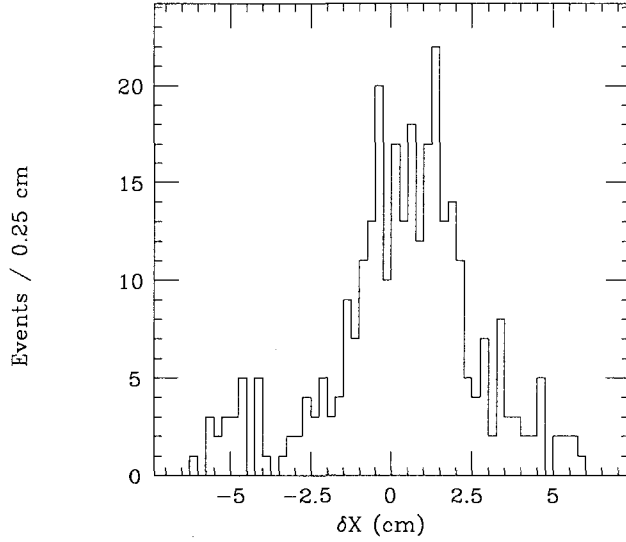


Figure 5.10: The difference, $\delta X = X_{\text{CDT}} - X_{\text{CMU}}$, from cosmic ray data.

A similar analysis can be made for the error in the CTC, CMU slope difference, $\delta S = S_{\text{CTC}} - S_{\text{CMU}}$, in the R - ϕ plane. The error in δS due to multiple scattering is

$$\sigma_{\delta S} < 0.006 \text{ radians}$$

for particles above 20 GeV/c. The error in δS due to P_t mis-measurement is then

$$\sigma_{\delta S} = 2 \text{ mm} / 3487 \text{ mm} = 0.001 \text{ radians}$$

where 2 mm is the uncertainty, δX , due to P_t mis-measurement and 3487 mm is the radial distance to the muon chamber. An upper bound on the error in δS due to chamber misalignment is obtained from figure 5.11 which shows the slope difference between the extrapolated CDT track and the CMU tracks. The error is found to be

$$\sigma_{\delta S} = 0.42 \times W_{\text{fwhm}} = 0.010 \text{ radians}$$

. The combined error in the CTC, CMU slope mismatch from all three sources is then

$$\sigma_{XY}^{\text{phi}} = \sqrt{0.006^2 + 0.001^2 + 0.010^2} = 0.012 \text{ radians}$$

The muon W candidates were required to have $\delta X < 3.0$ cm and a $\delta S < 0.030$ radians for the matching differences between the CMU track and the CTC track.

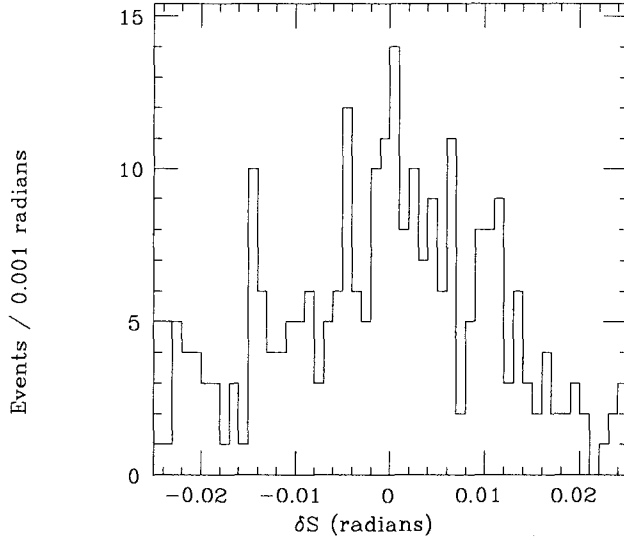


Figure 5.11: The difference, $\delta S = S_{\text{CDT}} - S_{\text{CMU}}$, from cosmic ray data

5.7 Require Missing E_t

Missing E_t , \vec{E}_t , is defined as

$$\vec{E}_t = - \sum_i \vec{E}_t^i$$

where \vec{E}_t^i is the energy deposition in a single tower of the CDF calorimeter. If a neutrino is present in an event, it carries away energy without interacting in the detector so that there will be a transverse energy imbalance and a non-zero \vec{E}_t . Minimum ionising particles such as muons deposit little energy in the calorimeter, and so look very much like a neutrino. \vec{E}_t for $W \rightarrow \mu + \nu$ events from calorimeter measurements alone should therefore be small. In order to get the true \vec{E}_t due to the neutrino, the calorimeter \vec{E}_t^{Cal} is corrected by

$$\vec{E}_t = -\vec{P}_t^\mu + \vec{E}_t^{\text{Cal}}$$

where \vec{P}_t^μ is the transverse momentum of the muon. Figure 5.12 is a plot of $|\vec{E}_t|$ versus muon P_t for all muon candidates after both minimum ionising and matching cuts were applied. The dotted line indicates the cuts made on muon P_t and $|\vec{E}_t|$. Muon W candidates are required to have $|\vec{E}_t| > 10$ GeV.

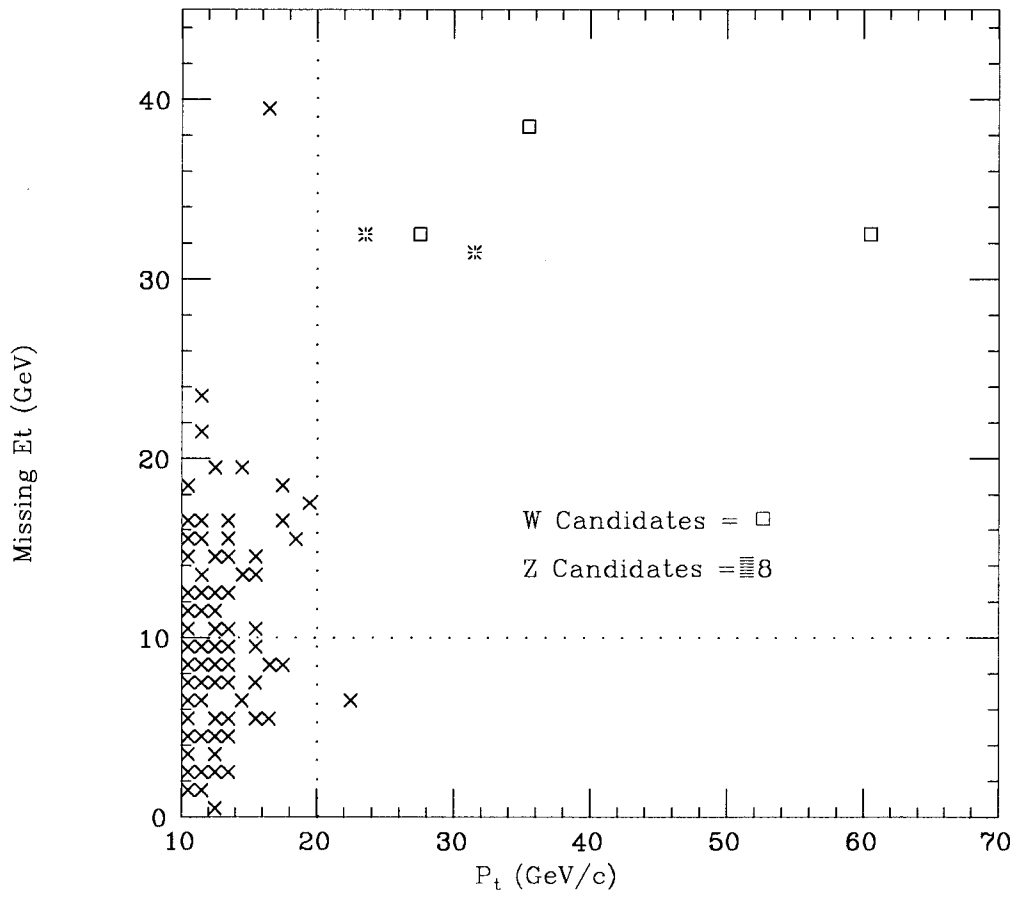


Figure 5.12: $|\vec{E}_t|$ versus P_t for muon candidates

Cut	Number of Events
Total Passing CMU Trigger	2.0×10^5
Require Muon $P_t > 20$ GeV/c	103
Require Minimum Ionising Muon	25
Require CTC, CMU Match	6
Require $ \vec{E}_t > 10$ GeV	5
Hand Scan for W's	3

Table 5.1: Breakdown Of Analysis Cuts

5.8 W Candidates

Table 5.1 summarizes the breakdown of the 27.2 nb^{-1} of data according to the cuts which were applied to the data. All 25 events which survived the minimum ionising cut were hand scanned. After the cuts have been made, there are 5 events left as $W \rightarrow \mu + \nu$ candidates. Two of the remaining events, 7787/2063 and 7787/102, can be identified as $Z \rightarrow \mu^+ + \mu^-$ candidates. In event, 7787/2063, the second muon appears in the forward muon chambers while in event, 7787/102, the second muon exits the detector in a region without muon coverage after depositing energy consistent with a minimum ionising particle. The remaining three events look like legitimate W candidates. Table 5.2 contains relevant information for the 5 events which pass all the cuts plus event 7582/2280 which passed all but the missing E_t cut. In table 5.2, momentum is in units of GeV/c, energy is in units of GeV and ϕ is measured in radians. Those events containing jets with $E_t^{\text{Jet}} > 10$ GeV have entries in the columns under jet E_t and ϕ_{Jet} . Total scalar E_t in the event is under column $\sum_i E_t^i$. Copies of the CDF event display for the events in table 5.2 may be found in appendix B.

Event 7605/6279 is a muon of $P_t = 60.7$ GeV/c and is recoiling against a gamma

Event	P_t^μ	ϕ^μ	$ \vec{E}_t^{\text{Cal}} $	ϕ_{E_t}	$\sum_i E_t^i$	E_t^{Jet}	ϕ_{Jet}
7582/2280	+22.3	335.5	17.6	320.3	53.6	17.4	158.7
7605/6279	-60.7	168.2	36.3	196.5	72.1	32.8	20.1
7589/1116	+27.1	127.9	12.9	239.5	58.3		
7604/2861	-35.1	129.7	9.6	21.2	52.0		
7787/102	-31.4	27.1	5.0	298.5	54.7		
7787/102	+33.5	215.7	5.0	298.5	54.7		
7787/2063	-23.3	161.0	10.8	316.8	37.4		
7787/2063	+15.5	342.4	10.8	316.8	37.4		

Table 5.2: Event parameters for W, Z events.

which is highly uncharacteristic of a W decay although $|\vec{E}_t| = 32.5$ GeV suggests the presence of a neutrino. The other two events, 7589/1116 and 7604/2861 appear to be standard W decays. Figure 5.12 indicates where these three events fall in $|\vec{E}_t|$. Figure 5.13 and figure 5.14 are plots of the electromagnetic and hadronic energy from the underlying event and may be compared with figures 5.6 and 5.7 for the electron W candidates.

5.9 Background

There are several sources of background to W decays. One source is due to interactive punch through where a particle from a high P_t hadron shower penetrates the central calorimeter and leaves a track in the muon chamber. A kaon or pion might also noninteractively punch through by passing through the calorimeter without strongly interacting and so fake a muon. Low P_t kaons ($P_t \approx 10$ GeV/c) can also decay into muons in the CTC and may be misreconstructed with a much higher P_t due to a kink in the CTC

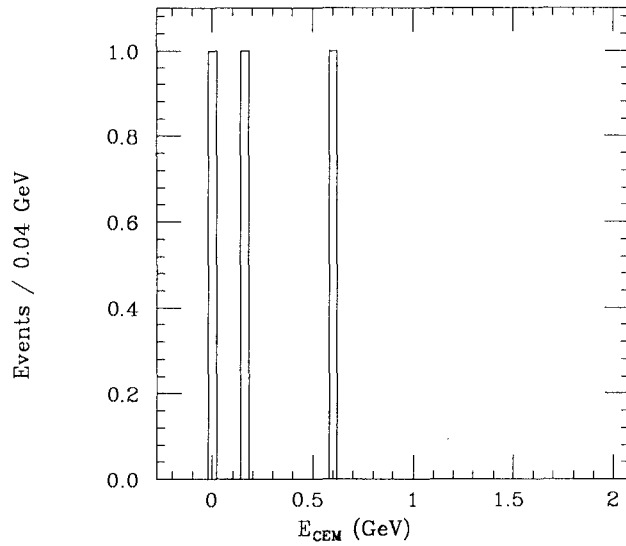


Figure 5.13: $E_{\text{CEM}}^{\text{T}}$ in a cone of $\delta R = 0.4$ from underlying event.

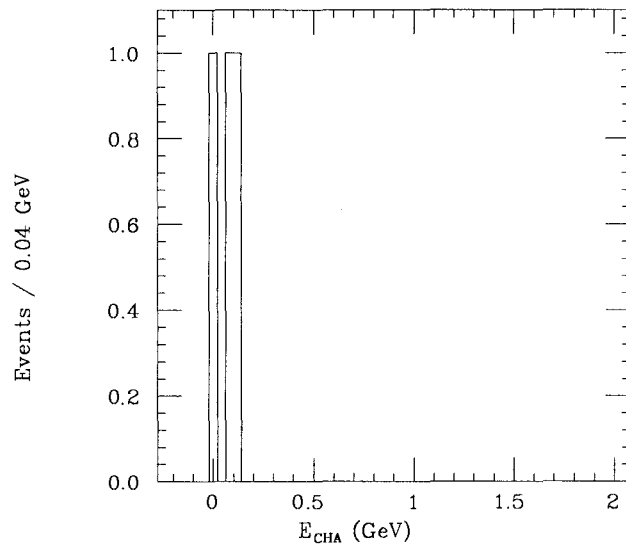


Figure 5.14: $E_{\text{CHA}}^{\text{T}}$ in a cone of $\delta R = 0.4$ from underlying event.

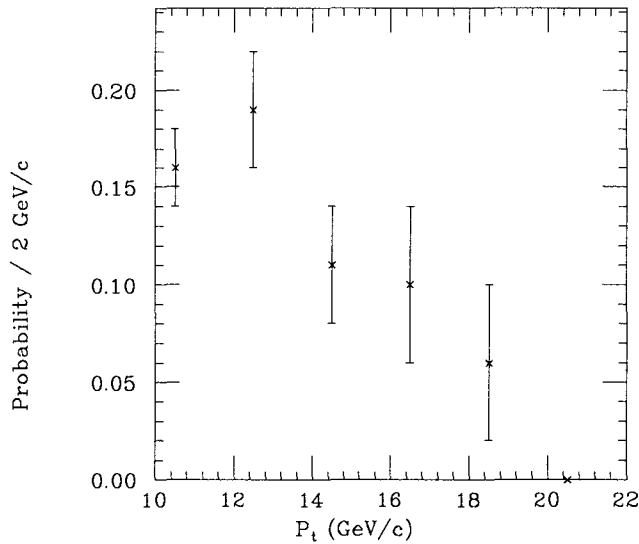
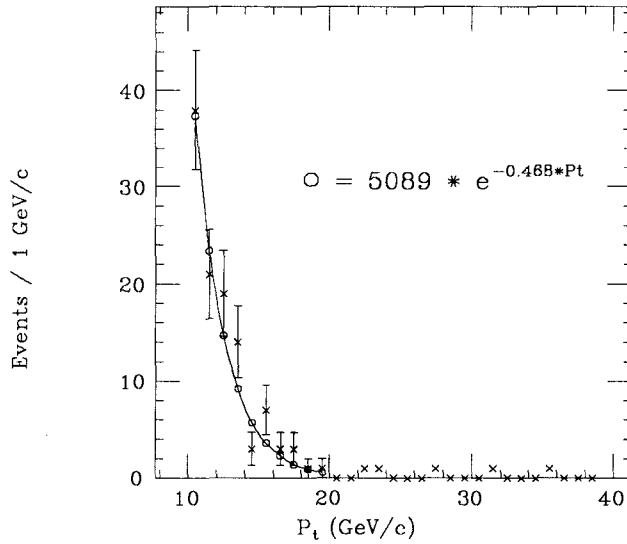


Figure 5.15: Probability that a muon passes energy and matching cuts.

track[16]. Finally there are prompt muons from semi-leptonic heavy flavor decay as well. Since the P_t spectrum for muons from W decay indicates that 87% have $P_t > 20$ GeV/c, it is safe to assume that all muons with $P_t < 20$ GeV/c are background. Figure 5.15 is a plot of the probability of a muon candidate passing the energy and matching cuts listed above as a function of P_t . If the sample with $P_t < 20$ GeV/c consisted solely of muons, figure 5.15 would be flat. Instead, the probability of getting a good muon drops with P_t . This is due to increasing probability of interactive punch through with P_t and also due to the increasing percentage of misreconstructed tracks as P_t increases. Figure 5.16 is a P_t spectrum of the muons which pass both energy and matching cuts. A fit with a function of the form, $A e^{B P_t}$, gives $A = 5089$ and $B = -0.468$ and a chi squared per degree of freedom of 1.3. Upon integrating the exponential over $P_t > 20$ GeV/c, 0.9 events are predicted as the background to the W sample.

5.10 Efficiency

The efficiency for observing W decays in the muon channel depends on several factors.

Figure 5.16: P_t spectrum of muon background

1. Trigger Efficiency

The trigger efficiency is somewhat of an unknown. Because 1987 was an engineering run for the CDF detector, significant alterations to the muon trigger were undertaken as the detector was taking data. In addition, the trigger hardware was operating under time constraints (a trigger decision was required between beam crossings) for which it was not designed. An estimate for the central track processor efficiency is $A_{\text{CFT}} \approx 0.70$ but was expected to be much greater ($A_{\text{CFT}} \approx 1.0$) for low multiplicity events with a high P_t muon above threshold (i.e. W events). The central muon level 1 trigger was expected to have $A_{\text{Trig}} > 0.98$ for muons above 20 GeV/c. Thus the trigger efficiency should have been $A_{\text{Trig}} > 0.98$ for muons with $P_t > 20$ GeV/c. Unfortunately this number can not be verified from the data directly but depends on trigger simulation of the central track processor using actual events and estimates for the level 1 efficiency. A conservative number of $A_{\text{Trig}} = 0.79$ will be used for the trigger efficiency.

2. Geometrical Acceptance

The geometrical acceptance was studied using the CDF detector simulation and

Isajet version 6.10 [7] as the event generator. EHLQ I [15] was used as the structure functions. 1000 $W \rightarrow \mu + \nu$ events were generated and then simulated in the CDF detector. The events were reconstructed using the standard CDF analysis package. The purely geometrical acceptance of the detector was found to be $A_{\text{Geom}} = 0.28 \pm 0.01 \pm 0.02$ where the second error is due to uncertainties in the structure functions. This systematic error was estimated by comparing the acceptance for EHLQ I with the acceptance using Duke-Owens I as the structure functions.

3. W Cuts

The efficiencies of the W cuts can be estimated by loosening each cut individually while applying all the rest.

(a) $P_t > 20 \text{ GeV}/c$

Monte Carlo studies using EHLQ I structure functions indicate that a P_t cut of $20 \text{ GeV}/c$ is $A_{P_t} = 0.87$ efficient for W's.

(b) Minimum Ionising Energy

Figure 5.17 is a plot of E_{CHA} versus E_{CEM} with the matching cuts applied but no calorimeter energy cuts. There are five additional events, all with $E_{\text{CEM}} > 2.0 \text{ GeV}$. From figure 3.5, there is no probability that these can be real muons. There are no events with $E_{\text{CEM}} < 1.0 \text{ GeV}$ and $E_{\text{CHA}} > 3.0 \text{ GeV}$ so that the efficiency for the energy cut is $A_{\text{Energy}} = 1.0$. Note, from figure 3.6, that with higher statistics the CHA energy cut would introduce some inefficiency for W selection.

(c) Matching Requirement

Figure 5.18 is a plot of δS versus δX for muons with $P_t > 20 \text{ GeV}/c$ which passed the calorimeter energy cuts only. From figure 5.18, the nearest event in δX to the candidate events has a $\delta X = -4.7 \text{ cm}$. The sigma in δX for the

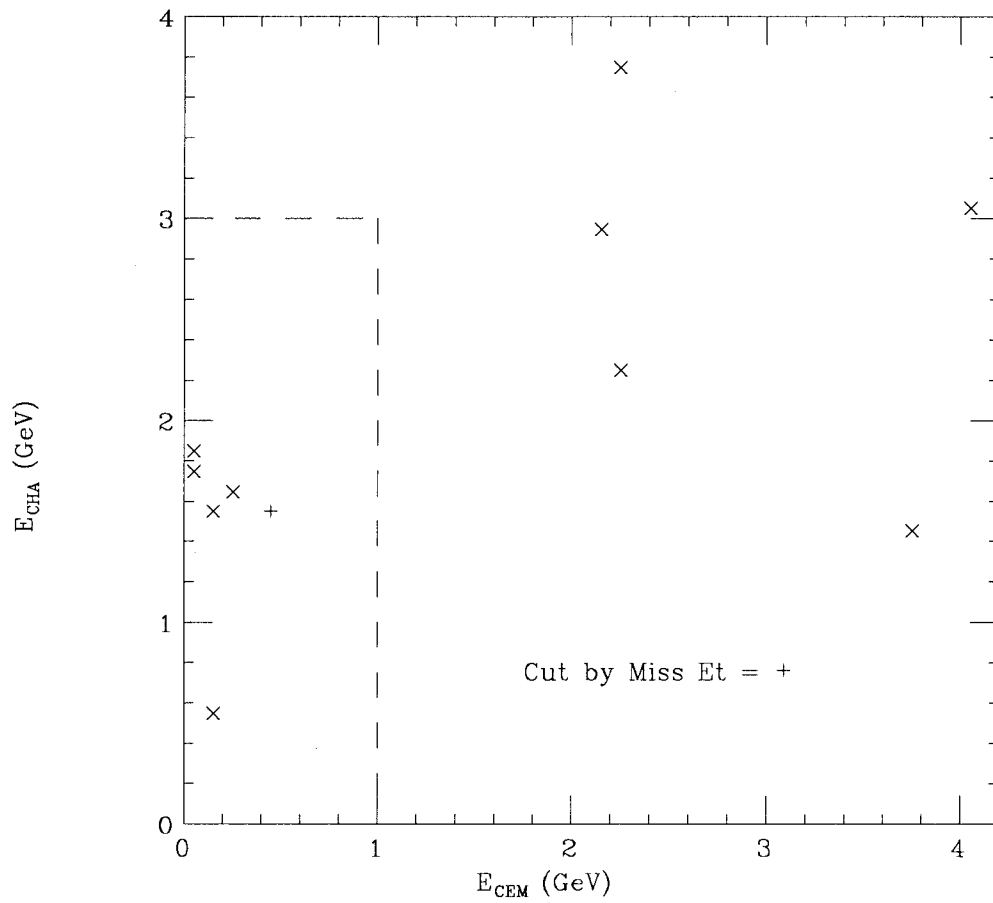


Figure 5.17: E_{CHA} versus E_{CEM} with matching cuts only.

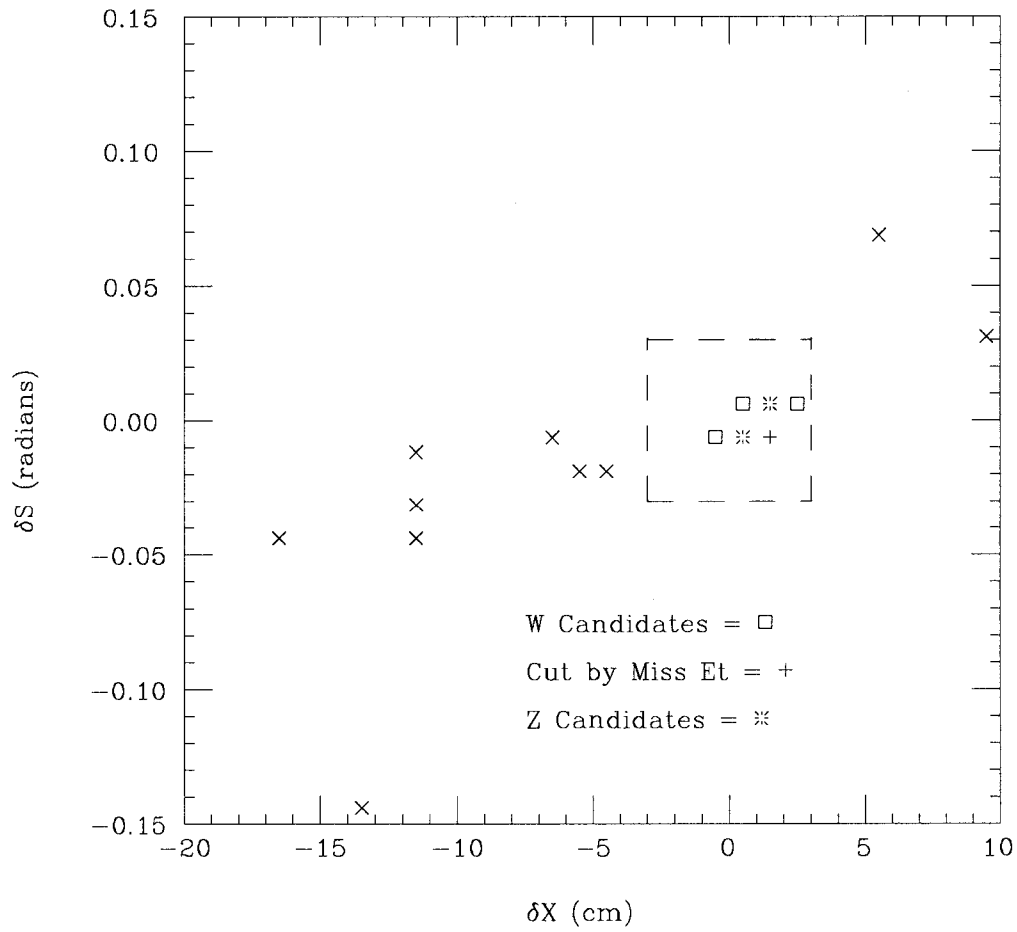


Figure 5.18: δS versus δX , for muons passing energy cuts only.

W and Z candidate muons is $\sigma = 1.4$ cm so that the probability that this event is a real W based on matching is less than 0.001. The efficiency of the matching cuts is therefore $A_{\text{Match}} = 1.0$ for this sample.

(d) $|\vec{E}_t| > 10$ GeV

Event 7582/2280 was the only event to pass all of the cuts except the \vec{E}_t cut. $|\vec{E}_t^{\text{Cal}}|$ is 17.6 GeV at $\phi = 320.3^\circ$ and is recoiling against an electromagnetic energy cluster of $E_t = 17.4$ GeV deposited at $\phi = 158.7^\circ$. The muon has $P_t = 22.3$ GeV at $\phi = 335.5^\circ$ which is nearly the same magnitude and direction as \vec{E}_t^{Cal} . This suggests that the missing E_t is generated by the muon (which looks like a neutrino in the calorimeter) and not by a neutrino. In addition, there is a $P_t = 3.1$ GeV pion which nearly overlaps in ϕ with the muon so that the muon isn't isolated. This event therefore looks like a background event in which a hadron of $P_t = 22.3$ GeV passes through the central calorimeter without strongly interacting and is recoiling against a cluster of hadrons (the electromagnetic jet) which have a collective $P_t \simeq 17.6$ GeV.

The background extrapolation in figure 5.16 predicts a single background event with $P_t > 20$ GeV and because the background is exponentially decaying, this event should appear with $P_t \simeq 20$ GeV which is where 7582/2280 is found. The efficiency for the missing E_t cut is therefore $A_{\text{Met}} = 1.0$.

5.11 Cross Section

$\sigma_W \times B_{W \rightarrow \mu\nu}$, where σ_W is the W production cross section and $B_{W \rightarrow \mu\nu}$ is the branching ratio into $\mu + \nu$, can be calculated based on the three observed W events, 7589/1116,

7604/2861, 7605/6279 and is given by

$$\sigma_W \times B_{W \rightarrow \mu\nu} = \frac{N}{\epsilon L} = 0.59^{+0.93}_{-0.32} (\pm 0.09) \text{ nb}$$

where $\epsilon = 0.19$ is the combined efficiency, including geometrical acceptance, $N = 3$ is the number of observed W events, and $L = 27.2 \pm 4.1 \text{ nb}^{-1}$, is the integrated luminosity. The first error is the statistical error and the last error is the systematic error due to uncertainty in the integrated luminosity, L. The statistical error is derived from the integral over the mean of a poisson distribution where three events are observed. The values of the mean for which the integral is greater than 0.05 and less than 0.95 are taken as the uncertainties in the observed number of W candidates, N. Figure 5.19 is a plot of $\sigma \times B_{W \rightarrow \mu+\nu}$ and $\sigma \times B_{W \rightarrow e+\nu}$ from CDF measurements as well as measurements for $\sigma \times B_{W \rightarrow e+\nu}$ from UA1 and UA2 versus the c.m. energy. The solid curve is a theoretical prediction by Altarelli, et. al. [6] and the dotted line represents the theoretical uncertainties. The theoretical curve has been adjusted for $M_W = 80 \text{ GeV}/c^2$. The points for UA2 and UA1 have been shifted $\pm 10 \text{ GeV}$ in c.m. energy respectively for clarity.

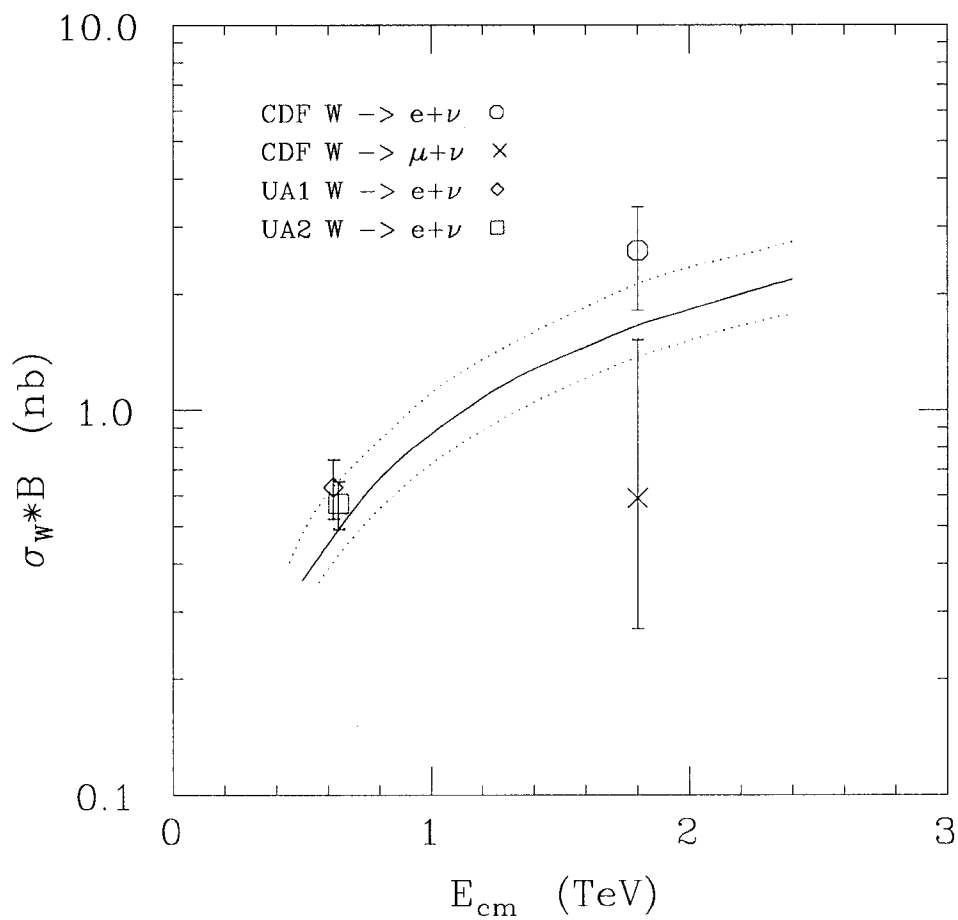


Figure 5.19: Cross section times branching ratio for $W \rightarrow \ell + \nu$ versus c.m. energy.

Chapter 6

Conclusions

We have observed muons with $P_t > 10 \text{ GeV}/c$ in 1.8 TeV $\bar{p}p$ collisions at the Fermilab Tevatron collider. Cuts on the data were developed to extract a sample of muons with $P_t > 20 \text{ GeV}/c$ which are consistent with $W \rightarrow \mu + \nu$ and with $Z \rightarrow \mu^+ + \mu^-$. Based on a sample of three events, the cross section times branching ratio for $W \rightarrow \mu + \nu$ was calculated to be

$$\sigma_W \times B = 0.59_{-0.32}^{+0.93} (\pm 0.09) \text{ nb}$$

which is consistent with theoretical predictions given the low statistics. In addition, we have observed several $\mu + \nu + \text{jet}$ events which suggest the possibility of new physics.

Appendix A

CDF Central Muon Detector

A.1 Introduction

In this appendix we will describe the drift chambers for muon detection in the central rapidity region, $|\eta| \leq 0.63$, of the CDF detector. These chambers identify muons by their penetration of the 5.3 interaction lengths of the central calorimeter, measure their positions and directions, and provide a level - one trigger for muons which have a transverse momentum greater than a given set value. In section 2 of this appendix, we describe the chamber geometry and how the level - one trigger is achieved. In section 3, we describe the method of construction and in section 4, the method of charge division is outlined. Section 5 contains some results obtained with cosmic ray and test beam data.

A.2 Geometry

The central muon detector is located around the outside of the central hadron calorimeter at a radial distance of 3487 mm from the beam axis. The muon detector is segmented in phi into 12.6° wedges which fit into the top of each central calorimeter wedge. This leaves a gap in the central muon coverage of 2.4° between each wedge. Access to the muon detector is through a 300 mm by 120 mm opening at each end of

the central calorimeter wedge so that each detector is further segmented in ϕ into three modules of 4.2° each. The three modules are bolted together at each end to form a single unit. This single unit is suspended from the top of the calorimeter wedge at three points which provide for adjustment of the chambers in both θ and ϕ [17]. Figure A.1 shows the location of the muon chambers within the central calorimeter wedge.

Each of the three modules in a wedge consists of four layers of four rectangular drift cells. A typical drift cell is shown in figure A.2. Overall dimensions of the cell are 63.5 mm wide by 26.8 mm high by 2261 mm long. A stainless steel resistive $50 \mu\text{m}$ sense wire is located at the center of the cell.

Arrangement of the sense wires within a muon chamber permits a lower bound on the transverse momentum of a particle to be determined. Four drift cells, one from each layer, make up a muon tower (figure A.3). Two of the four sense wires, from alternating layers, lie on a radial line which passes through the interaction point. The remaining two wires of the tower lie on a radial line which is offset from the first by 2 mm at the midpoint of the chamber. The ambiguity as to which side of the sense wires (in ϕ) a track passes is resolved by determining which two sense wires were hit first. The angle, α , between a particle track and the radial line passing through the sense wires can be determined by measuring the difference in arrival times of the drift electrons. A muon tower therefore provides two independent measurements of α .

Figure A.4 shows a transverse projection of a track as a particle passes through the central solenoidal magnetic field. If β is the angle of deflection due to the magnetic field and α is the angle between the track and a radial line from the interaction point, then α and β are related by

$$D \sin(\alpha) = L \sin\left(\frac{\beta}{2}\right), \quad (1)$$

where $D = 3487$ mm is the distance from the interaction point to the bottom of the muon detector and $L = 1476$ mm is the radius of the solenoidal magnetic field.

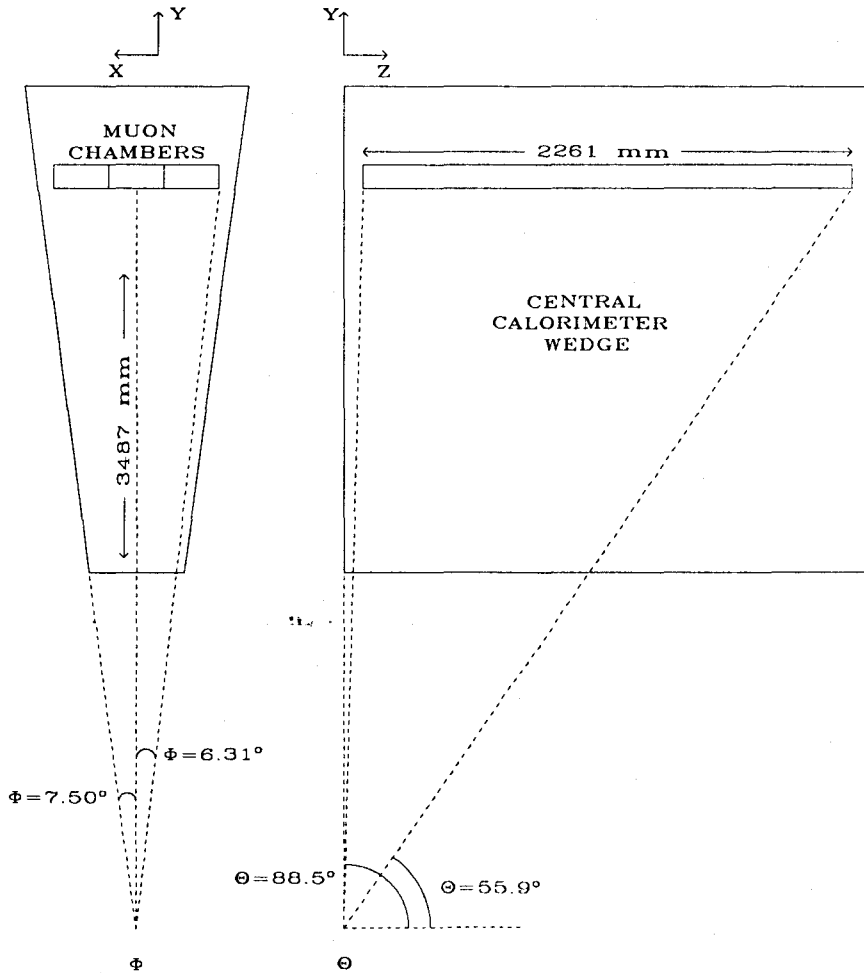


Figure A.1: Location of the central muon chambers within the central calorimeter.

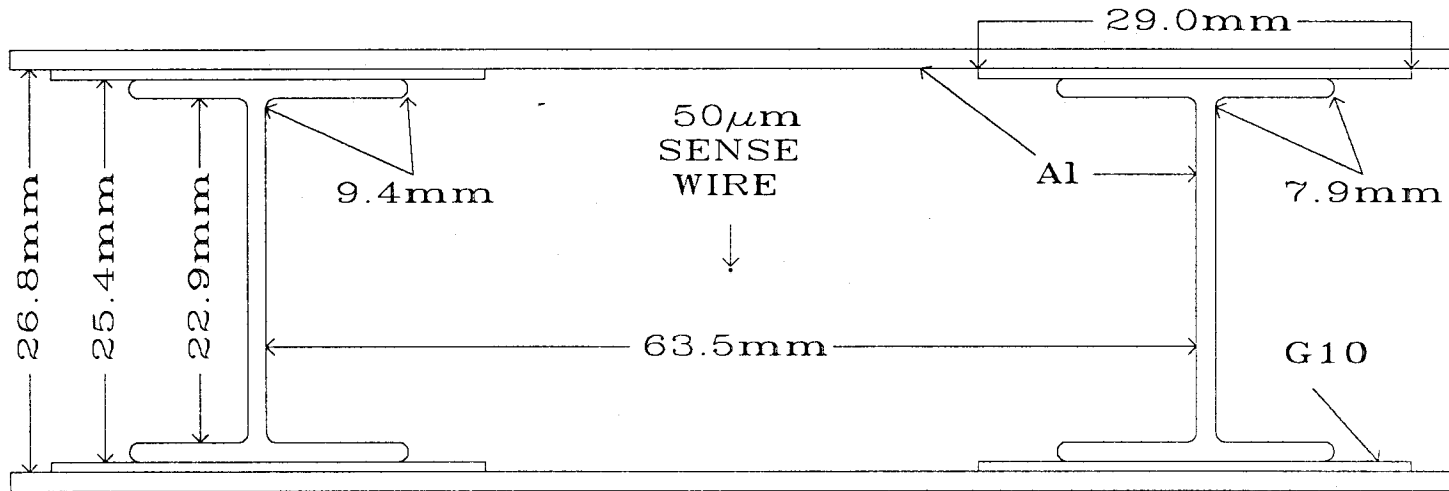


Figure A.2: Central muon drift cell.

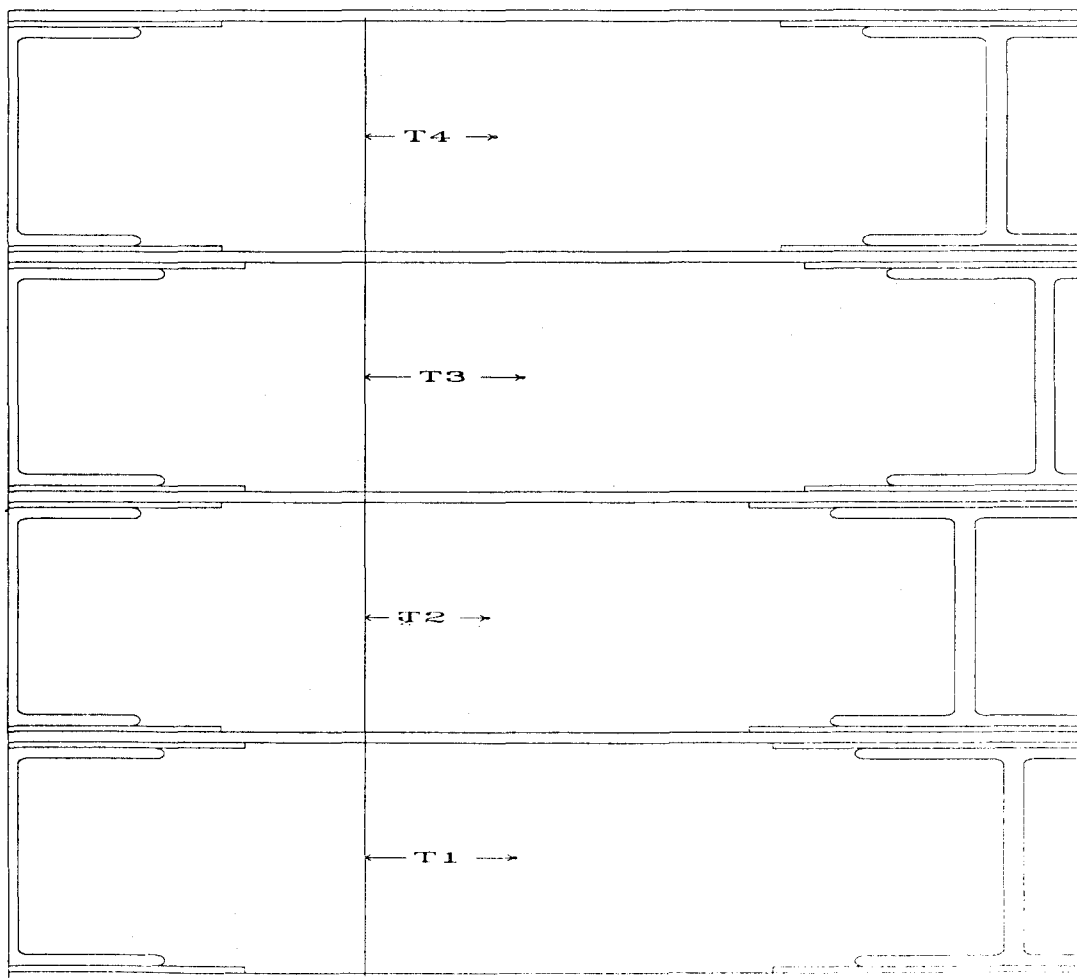


Figure A.3: Central muon tower consisting of four drift cells.

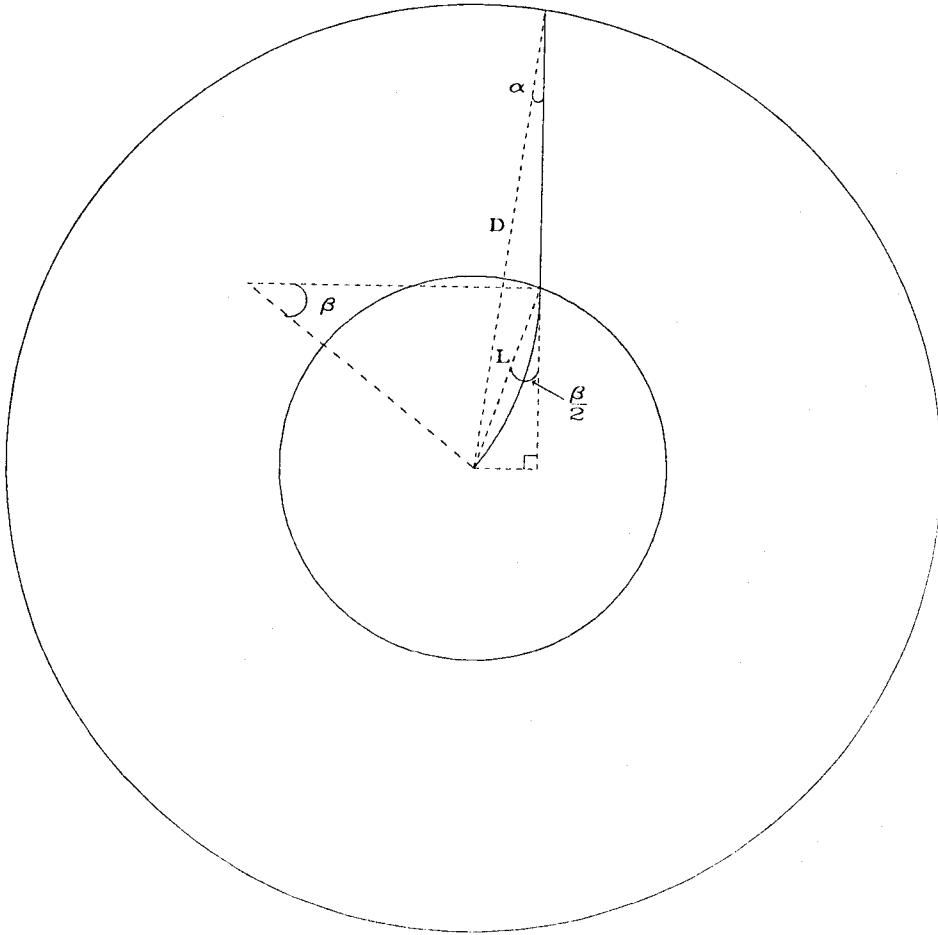


Figure A.4: Transverse view of a charged particle in the CDF detector. The inner circle is permeated by a 1.5 Tesla magnetic field while the outer circle represents the lowest plane of central muon sense wires.

The angle β in turn can be related to the transverse momentum of a particle. If $B = 1.5$ Tesla is the magnitude of the magnetic field and P_t is the transverse momentum of the particle, then

$$\sin\left(\frac{\beta}{2}\right) = \frac{eLB}{2P_t} \quad (2)$$

Equations (1) and (2) when combined give α in terms of P_t

$$\alpha \simeq \sin(\alpha) = \frac{eL^2B}{2DP_t}$$

The relationship between α and the difference in drift times, Δs , for two sense wires in alternating layers is given by

$$\Delta s = \frac{H\alpha}{v}$$

where $H = 55.0$ mm is the separation of the sense wire layers, and v is the drift velocity of the ionization electrons.

Δs is compared to a preset value in the RABBIT muon level - one trigger card [12]. If Δs is less than this value, a level - one trigger signal is generated.

A.3 Chamber Construction

The top and bottom of a drift cell consist of 0.79 mm thick aluminum sheets which span the width of the muon chamber. The sheets are held at ground through small brass 90° angle joints which are connected to the sheets and the aluminum chamber end plates with conductive epoxy. The sides of the cell consist of 25.4 mm aluminum I-beams (C-beams for those cells at the side of chamber) which are electrically insulated from the top and bottom sheets with 0.62 mm thick G-10 strips. The I-beams and C-beams are held at -2500 V. In the center of the cell is a 50 μm stainless steel sense wire with a resistance per unit length of 0.4 Ωmm^{-1} . The sense wire enters the cell through the chamber end plate and is electrically insulated from it by a delrin sleeve. A hollow brass pin in the middle of the sleeve is crimped around the wire to hold it in place. The wire

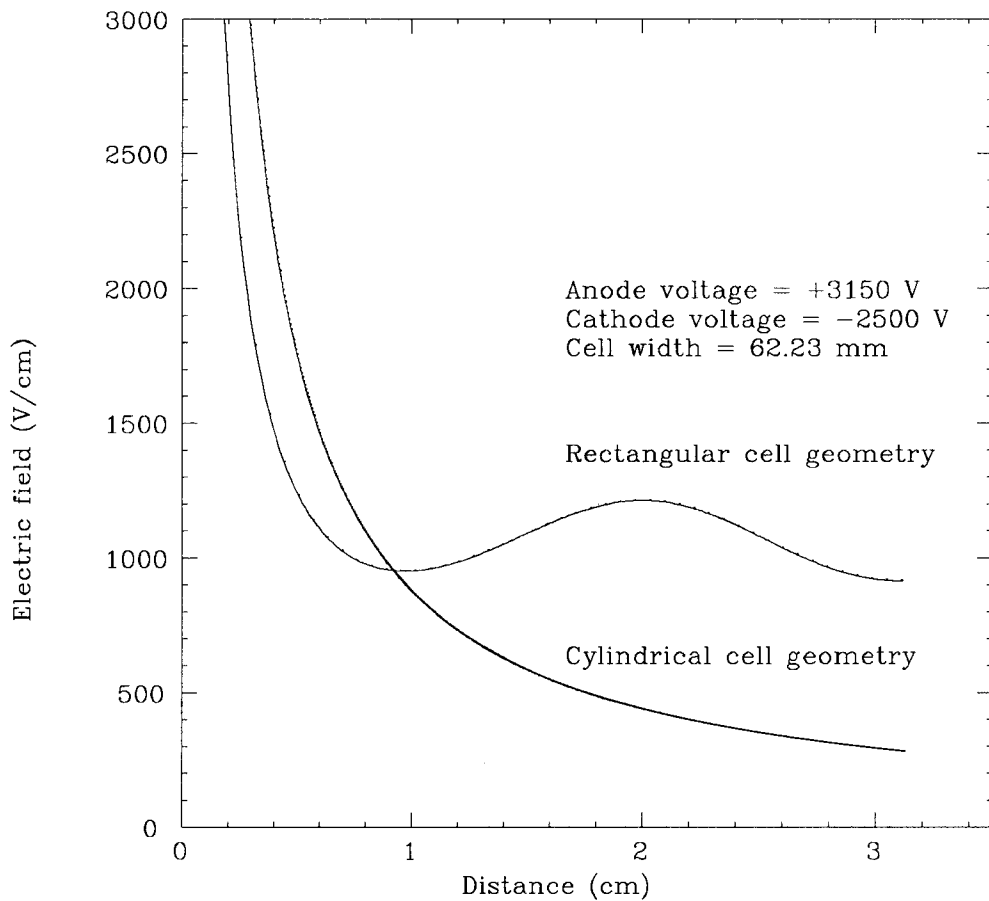


Figure A.5: Electric field as a function of distance from the sense wire.

is placed under a tension of 110 gm which limits the wire sag to $90 \mu\text{m}$. The sense wire is normally held at +3150 V.

Figure A.5 shows the electric field as a function of distance from the wire along a horizontal line passing through the center of the cell. The local minimum in the electric field near the wire is sensitive to the cell width and is also sensitive to the width of the top and bottom of the I-beams. The minimum in the field closest to the I-beam is primarily sensitive to the width of the top and bottom of the I-beam. Because the sense wire arrangement within a chamber requires cell widths ranging from 56.6 mm to 67.8 mm, adjustment of the I-beam width is necessary to insure that the electric field at the

wire is the same for all cells. A minimum field strength of 100 V mm^{-1} is required to maintain a constant drift velocity in 50%/50% argon-ethane gas with 0.7% ethanol [19].

Charge division is used to obtain the position of a track along the sense wire. In order to reduce the number of electronics channels and to enable readout of the chambers to occur at one end of the chamber only, each sense wire is connected at the $\theta = 90^\circ$ end to a sense wire in the same layer which is separated from the first by an intervening drift cell (figure A.6). At the $\theta = 56^\circ$ end of the wire is a $0.1 \mu\text{F}$ blocking capacitor which in turn is connected to the RABBIT muon ADC/TDC cards [10]. The blocking capacitors for all channels of a chamber reside in a single package which bolts on to the $\theta = 56^\circ$ end of the chamber. This package also contains the positive HV connector and readout cable connectors. A smaller package bolted on to the $\theta = 90^\circ$ end contains the negative HV connector and distribution pads for the I-beams in each of the four layers. The electrical connections between the sense wires and the electronics packages are made with flexible cylinders made of conductive epoxy which fit over the brass pins holding the sense wires and butt up against distribution pads on the electronic packages.

A total of 180 muon chambers or 60 wedges were constructed. An individual chamber is constructed starting with the layer furthest from the beam axis. The two aluminum endplates are mounted on a fixture which holds them precisely 2261 mm apart. An aluminum sheet 254 mm wide by 2286 mm long is glued on to the endplates with epoxy to form the top of the chamber. G-10 strips 112 mm wide by 2274 mm long are glued on to form the sides of the chamber. The endplates and accompanying sheets are then transferred to a fixture on a granite table which rigidly holds the end plates and sheets in the desired rectangular shape. C-beams are glued in on each side of the chamber and form the outer walls of the drift cells at the sides of the layer. The location of each of the three I-beams in a layer is determined by spacers which place the I-beam the correct distance from the I or C-beam already in place. An automatic gluing machine then lays down a bead of Eastman 910 along the entire length of the chamber. Another device

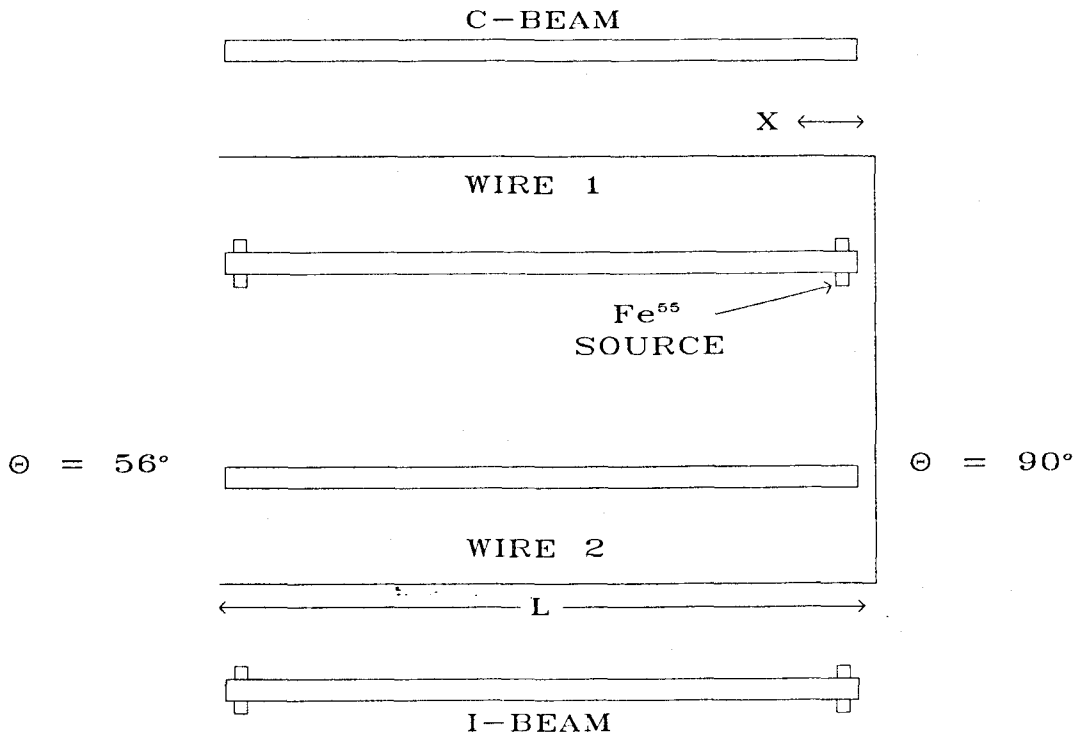


Figure A.6: Three drift cells in a plane. The sense wire length, L , is 2261 mm. The Fe^{55} sources are used for calibration of charge division.

with jaws which hold an I-beam straight along its entire length then presses the I-beam in place with air cylinders. The C and I-beams are internally connected together with jumper wires which connect adjacent beams so that only one negative HV feedthrough is needed for each layer of beams. An aluminum sheet is then glued on top of the I and C-beam to form the top of the cells and complete the layer. Holes have been cut in the interior aluminum sheets to allow gas to pass between layers. Each of the four layers is built up in this manner until the chamber is complete. The chamber is then strung with the sense wires which have 110 gm of tension on each.

The tension of each wire is checked by placing a portion of the chamber in a magnetic field and driving the wires with an alternating voltage as in figure A.7. A lock-in amplifier is used to monitor the in phase component, V_{in} , and the out of phase component, V_{out} , of the voltage drop across $R_T = 50 \Omega$ resistance relative to the driving voltage. The lowest resonance frequency of the sense wire is given by

$$\omega_o = \frac{2\pi\sqrt{T/\rho}}{2L} \simeq 2\pi \times 58 \text{ Hz},$$

where $T = 110 \text{ gm}$ is the tension of the wire; $\rho = 1.55 \times 10^{-5} \text{ gm mm}^{-1}$ is the linear mass density of the wire; and $L = 2261 \text{ mm}$ is the length of the wire. It can be shown that if the frequency of the driving voltage, ω , is near that of the resonance frequency, ω_o , then V_{in} is given by

$$V_{\text{in}} = \frac{R_T V_o}{R_T + R_{\text{wire}}} \left(1 + \frac{\omega\beta\tau}{(\omega - \omega_o^2/\omega)^2\tau^2 + 1} \right)$$

and V_{out} is given by

$$V_{\text{out}} = \frac{R_T V_o \omega\beta\tau^2}{R_T + R_{\text{wire}}} \frac{(\omega - \omega_o^2/\omega)}{(\omega - \omega_o^2/\omega)^2\tau^2 + 1}$$

where V_o is the magnitude of the driving voltage; τ is the damping time for the wire; $R_{\text{wire}} = 904 \Omega$ is the wire resistance and

$$\omega\beta = \frac{B^2 I^2}{MR_{\text{wire}}} \quad (3)$$

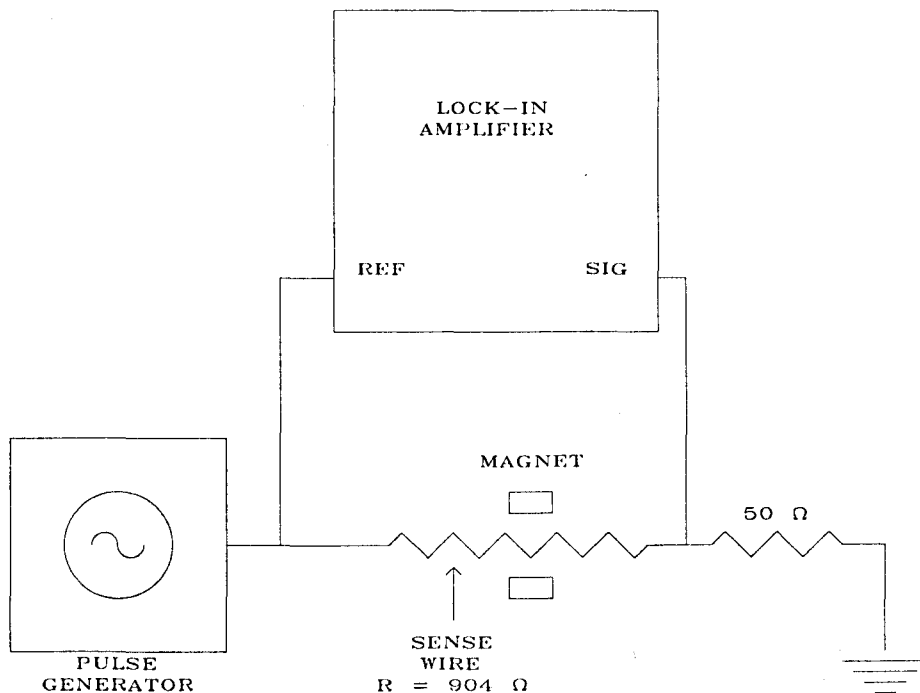


Figure A.7: The sense wire tension is tested by driving the sense wire with a variable frequency and monitoring the in phase and out of phase component of the voltage drop across the 50 Ω resistor. The in phase component attains a maximum value while the out of phase component is zero at resonance.

In equation (3), B is the magnetic field; l is the length of wire in the field; and M is the mass of the wire. It is important to notice that V_{out} vanishes at resonance while V_{in} attains a maximum. The resonant frequency of the wire can therefore be determined by sweeping the frequency of the alternating voltage over a range of values until V_{out} vanishes and V_{in} attains a maximum.

A.4 Charge Division

The position of a track along the sense wire is found by charge division. If a streamer pulse, with total charge, Q_0 , drifts to the wire from a point X mm from the $\theta = 90^\circ$ end of the chamber on wire 1 (figure A.6) then the total charge collected in ADC1 is given by

$$Q_1 = \frac{Q_0}{2} \left(1 + \frac{X}{L}\right) \quad (4)$$

and the charge reaching ADC2 is

$$Q_2 = \frac{Q_0}{2} \left(1 - \frac{X}{L}\right) \quad (5)$$

where L is the length of the unpaired wire. The ratio

$$R = \frac{Q_1 - Q_2}{Q_1 + Q_2} = \frac{X}{L}$$

is then linearly dependent on X . Because the input impedances of the charge amplifiers on the RABBIT muon cards are not zero, the absolute value of R does not range from zero to one but attains a maximum value somewhat less than one. The value of R is also depends on the exponential decay ($\tau = CR_{\text{wire}}$) of the charge accumulated on each of the $0.1 \mu\text{F}$ blocking capacitors at the ends of the wire pair. This leads to modification of equations (4) and (5) of the form

$$Q_1 = \frac{Q_0}{2} \left(1 + \frac{X}{L} e^{-t/\tau}\right)$$

and the charge reaching ADC2 becomes

$$Q_2 = \frac{Q_0}{2} \left(1 - \frac{X}{L} e^{-t/\tau}\right)$$

R is then given by

$$R = \frac{X}{L} e^{-t/\tau} \quad (6)$$

The time, t , in equation (6) is the time interval measured by the TDC's so that R can be corrected for the charge decay. X is then a function of R of the form

$$X = AR + B$$

where $A = L$ and $B = 0$.

In general there are variations in wire resistance and the location at which the sense wires have been crimped is not known. It is therefore necessary to calibrate the charge division (i.e. derive A and B) for each wire. To accomplish this calibration, Fe^{55} sources have been placed in two of the three I-beams of each layer so that each drift cell has a source 75 mm from each end directed into the cell (figure A.6). Each Fe^{55} source emits 5.9 KeV γ rays which produce an interaction in the cell at the rate of about 30 Hz. Source runs are taken in which plots are made of the number of events as a function of R for each source. A gaussian plus background curve is fit to each source plot and the mean location in R of each source is determined. Figure A.8 shows the location, in R, of the four sources in a muon tower. If R_1 is the mean value in R of the source at a distance of D_1 along the wire and R_2 is the mean value of the source at D_2 along the wire then $A = (D_2 - D_1)/(R_2 - R_1)$ and $B = D_1 - A \times R_1$ are determined for each wire.

A.5 Chamber Performance

As part of the checkout procedure of the muon chambers, each chamber goes through a cosmic ray test stand. The test stand set up is illustrated in figure A.9. The chambers

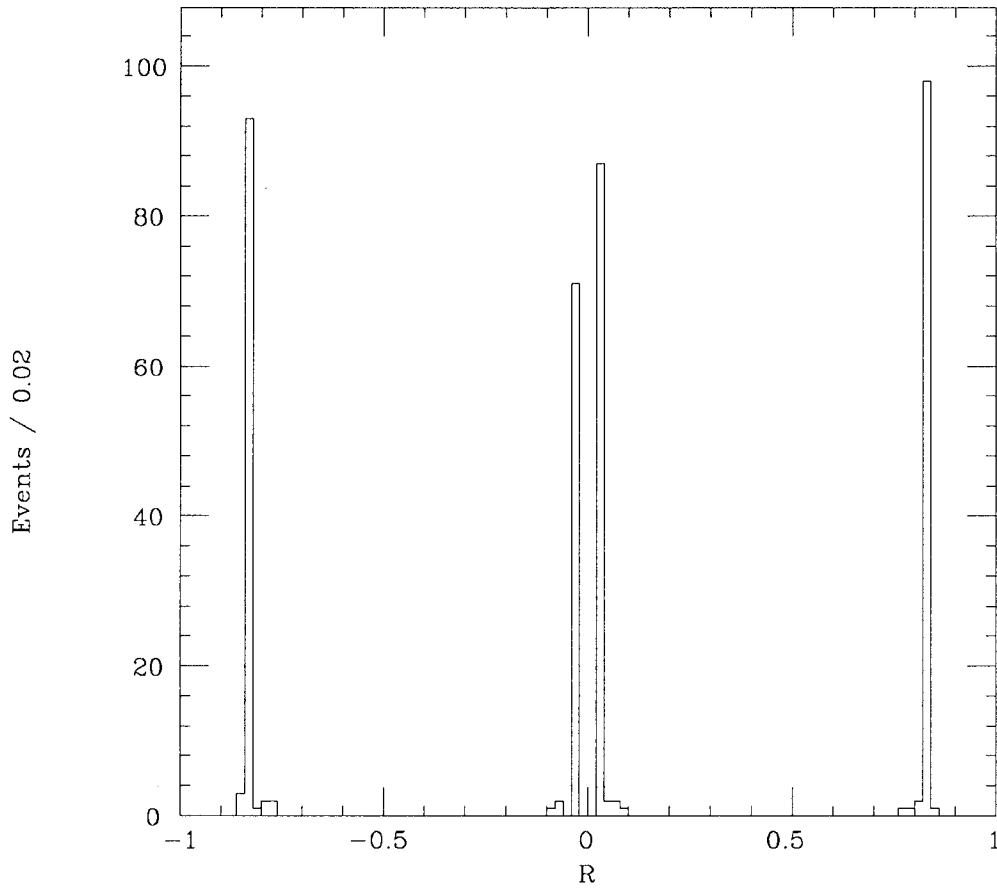


Figure A.8: Location in R of the four Fe^{55} sources for a sense wire.

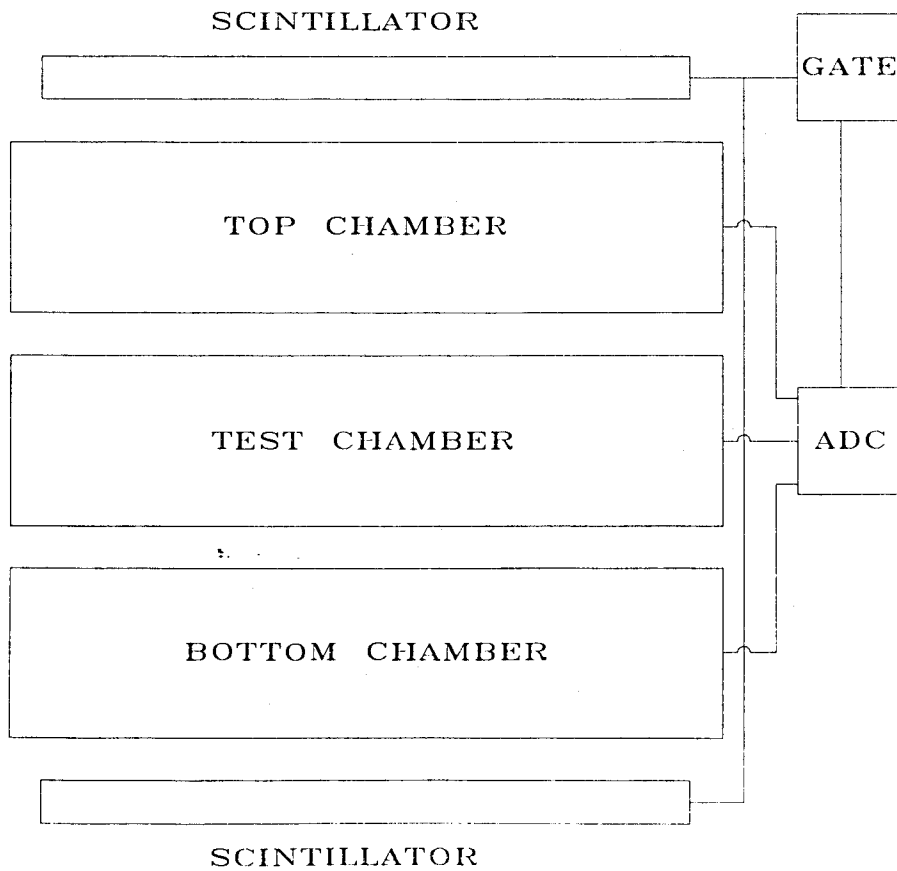


Figure A.9: Cosmic ray test stand setup. The top and bottom chambers define the cosmic ray track which is then interpolated into the center test chamber. Efficiencies for each sense wire can then be determined. The scintillators are used in the trigger.

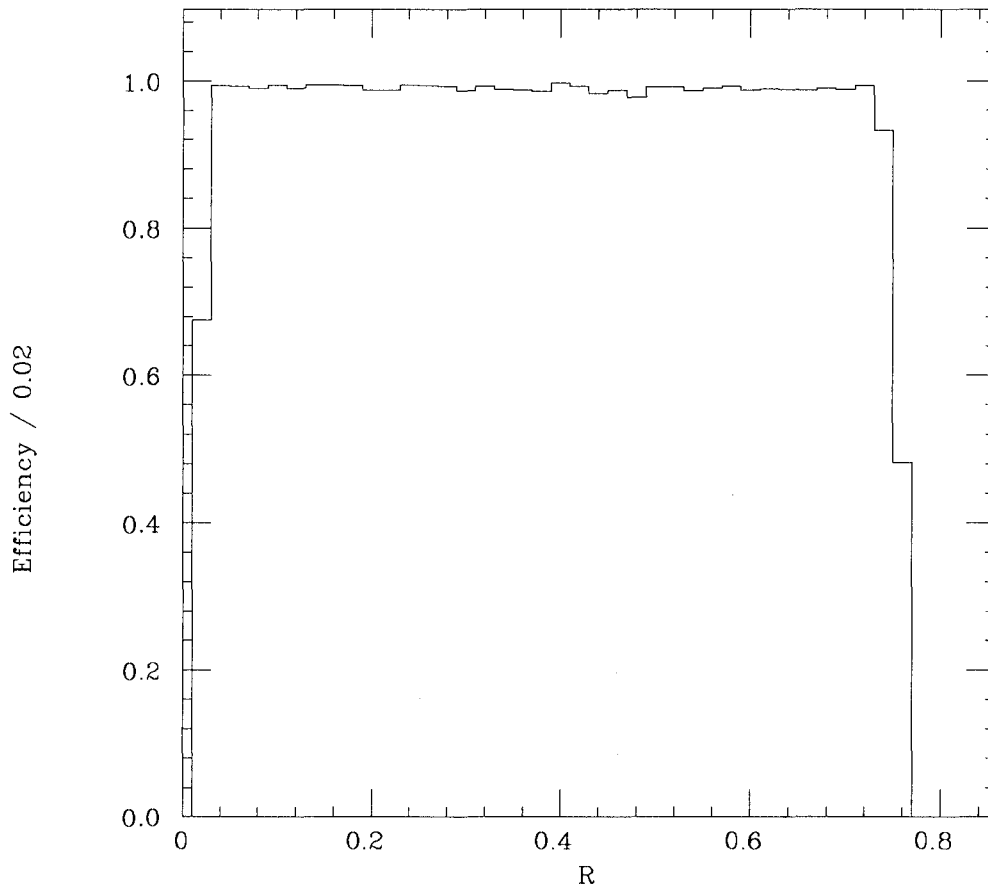


Figure A.10: Efficiency as a function of R for a typical sense wire.

operate in the limited streamer mode with the sense wires at +3150 V and -2500 V on the beams. The top and bottom chambers are used to reconstruct a cosmic ray track which is then projected into the center chamber undergoing testing. The sense wires are divided into 50 mm segments and an efficiency is found for each segment. Figure A.10 shows the results for a typical wire. The wire shows a drop in efficiency at the ends of the chamber due to the distortion of the electric field there.

A cosmic ray run was taken with the muon chambers at $\phi = 67.5^\circ$ and $\phi = 82.5^\circ$ in the CDF detector. The muon level-one trigger card was set up to require a coincidence of all four layers in each muon tower. Prior to the cosmic ray run, source runs were

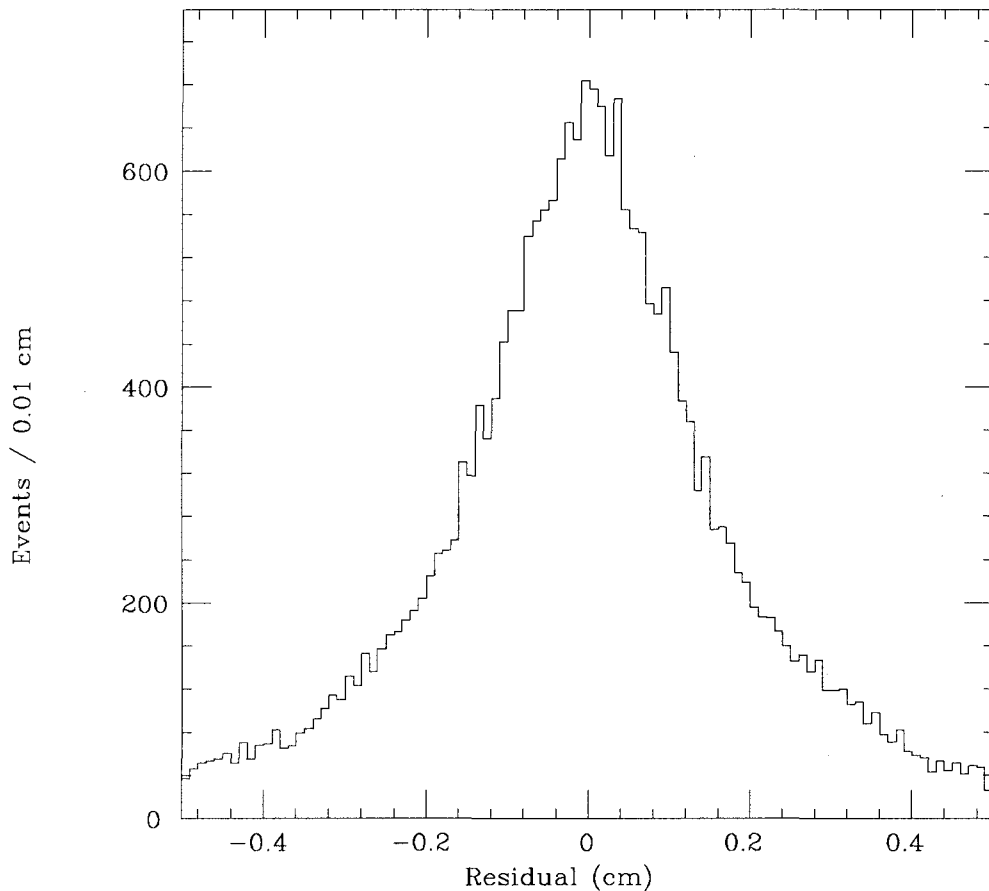


Figure A.11: Residual errors of the fit to cosmic ray tracks in the ZY plane.

taken and A and B were determined for each sense wire. Figure A.1 shows the local coordinate system used in the following analysis.

For a cosmic ray track, the projection of the track into the ZY plane was fit using charge division information from four sense wires in a muon tower. Resolution of the chamber along the wire was determined from a plot of the residuals of the fit for all wires in the wedge at $\phi = 67.5^\circ$. The residual error is defined to be the difference between the fitted track and the location of the hit on a sense wire. Figure A.11 shows a plot of the scaled residual errors for the fit in the ZY plane. Because the sigma of a residual plot tends to underestimate the resolution, the residual for each wire is multiplied by a

layer dependent factor which compensates for this underestimation. The residuals for the inner most and outer most layers were multiplied by 1.83 while the residuals for the two middle layers, were multiplied by 1.20. Figure A.11 gives an rms resolution along the sense wire of 1.2 mm.

A similar situation exists for the fit in the drift direction (XY plane). The calibration constants needed for fitting a track in the drift direction are the drift velocity and time zero, where time zero is the drift time of an event which passes through the sense wires. For technical reasons, time zero could not be determined for this cosmic ray run. The drift velocity, however, can be determined by comparing the difference in time between streamer pulses arriving at the wires which are offset by 2 mm from each other in a muon tower. Referring to figure A.3 where T_i is the drift time for wire i , a plot of the quantity

$$\delta = \frac{T_1 - 3T_2 + 3T_3 - T_4}{4}$$

will have a double peak since tracks on different sides of the sense wires have a delta of opposite sign. The two peaks are separated in space by twice the offset of the wires (2 mm) so that the drift velocity is given by 4 mm divided by the difference in time between the two peaks. Figure A.12 shows a plot of number of events as a function of δ for a typical tower. Figure A.13 shows the scaled residual plots of the fit in the drift direction (XY plane) for all the wires in the wedge. The rms resolution in the drift direction from this plot is 250 μm .

Data was also taken with the muon chambers when the central calorimeter wedges were undergoing calibration in a pion test beam. The central calorimeter was placed on a hydraulic table which allowed the wedge to be moved in both theta and phi. The beam pipe was directly over the pivot point of the table so that beam could be directed into each central calorimeter tower. Figure A.14 is a plot of the ADC distribution from the chambers. The single streamers peak at about 90 pC while a double streamer peak

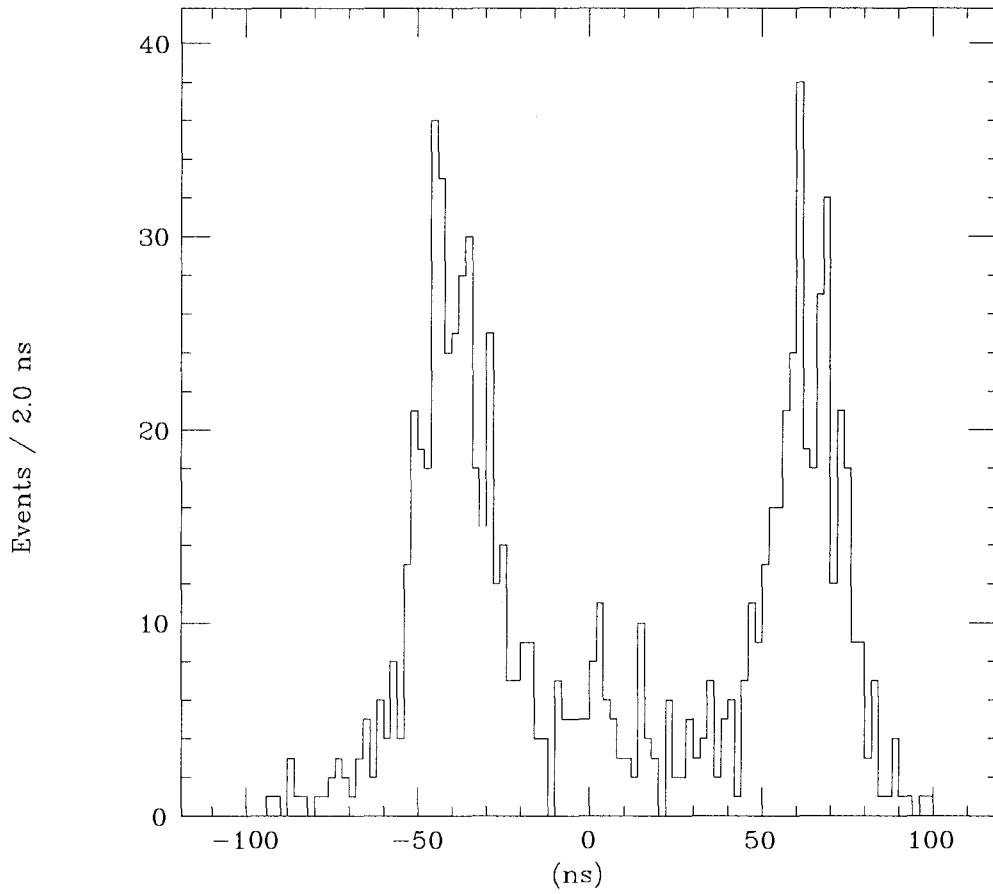


Figure A.12: A plot of $\delta = \frac{T_1 - 3T_2 + 3T_3 - T_4}{4}$. The separation of the two peaks in time represents a separation of 4 mm in space.

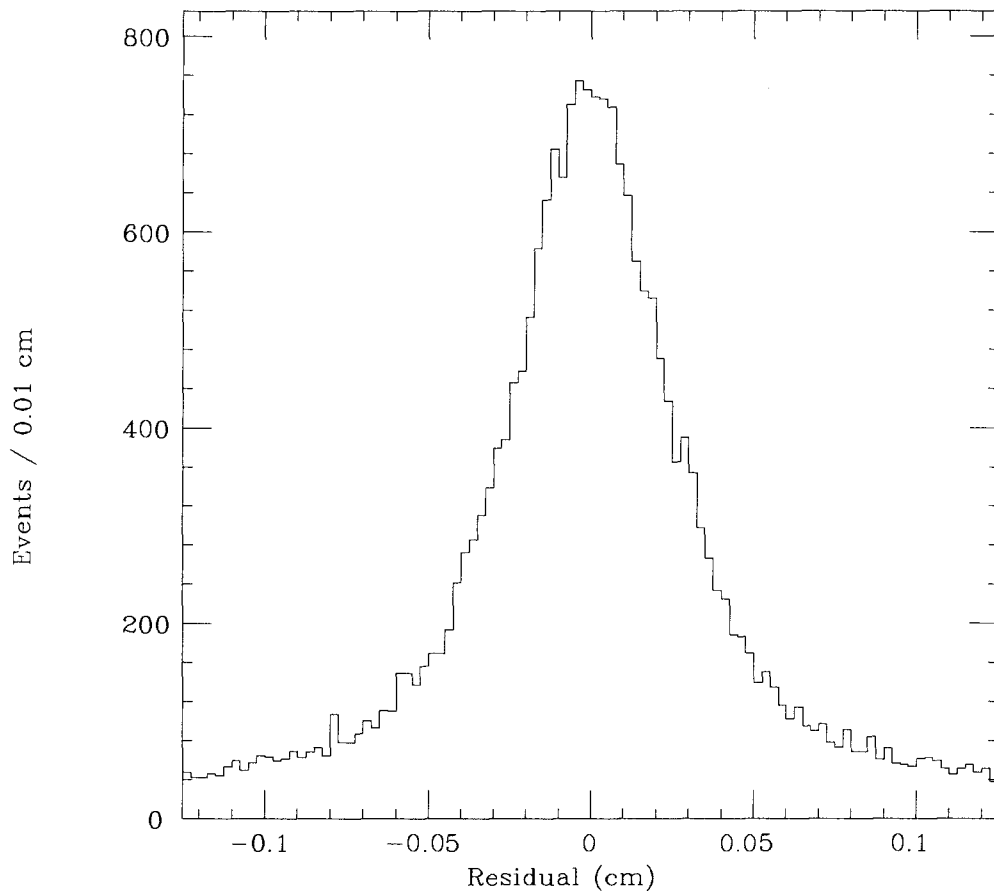


Figure A.13: Residual errors of the fit to cosmic ray tracks in the XY plane.

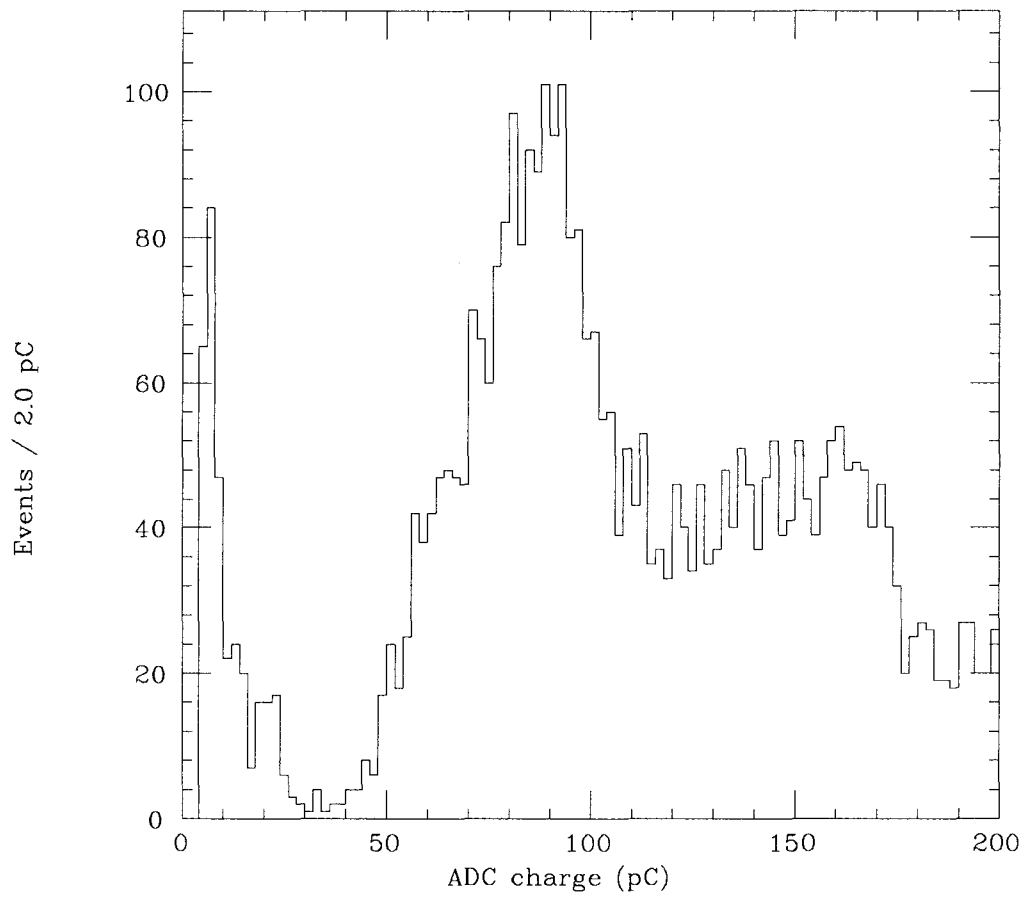
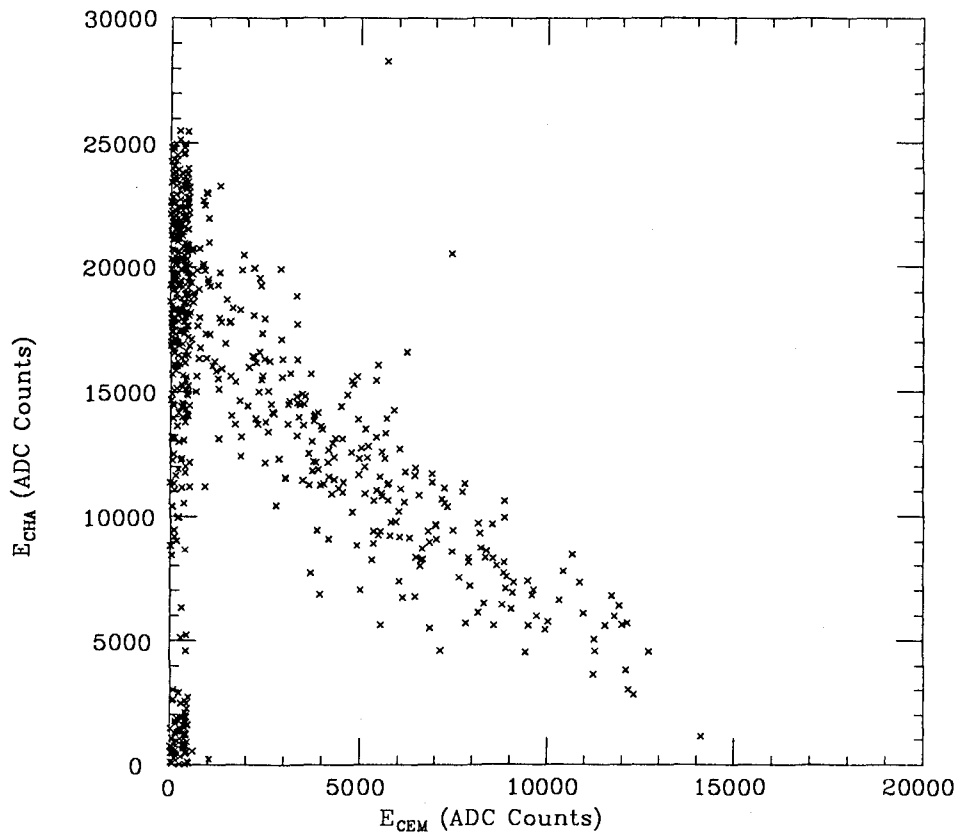


Figure A.14: Pulse height distribution for the muon ADC's.

is seen at about 160 pC. The valley in the distribution at about 30 pC is taken as the cut off for valid hits in the muon chamber.

The pion beam energy ranged from 15 to 50 GeV so the punch-through probabilities as a function of pion energy could be studied. For each run, the beam was directed into the center of tower 2 of the central calorimeter wedge. At tower 2, there is the equivalent of 110 cm of iron. Figure A.15 is a scatter plot of energy deposition in the central hadron calorimeter, E_{CHA} , vs energy deposition in the central electromagnetic calorimeter, E_{CEM} , for 50 GeV pions which produced at least two hits in the muon chamber. Those particles with total energy deposition less than 3000 ADC counts $\simeq 7$ GeV were assumed to be muons and were removed from the sample of punch-through candidates. The ratio of the number of events showing more than two hits in the muon chamber to the total number of pion interactions is plotted as a function of beam energy in figure A.16. Data from Bodek [18] for 110 cm of iron is shown for comparison. With the beam in calorimeter tower 2, the muon chambers extend about 100 cm on either side of the beam in the ZY plane. In XY plane however, the chambers only extend 38 cm to either side of the beam axis. To insure that no punch through events were lost because all of the particles passed through the side of the wedge and not through the muon chamber, the ϕ (in units of CMU cell number) of the particle which passed closest to the beam axis in a punch-through event was plotted in figure A.17. Each increment in cell number is an additional 63.5 mm from the beam axis. Figure A.17 indicates that very few punch-through events fail to intersect the muon chambers so that the punch-through probabilities are correctly reflected in figure A.16.

Figure A.18 is a plot of the number of tracks per event found for tracks in the drift direction (XY plane) for 50 GeV pion punch through events. The vast majority of such events produce only a single track in the muon chambers.

Figure A.15: E_{CHA} vs E_{CEM} for 50 GeV pions.

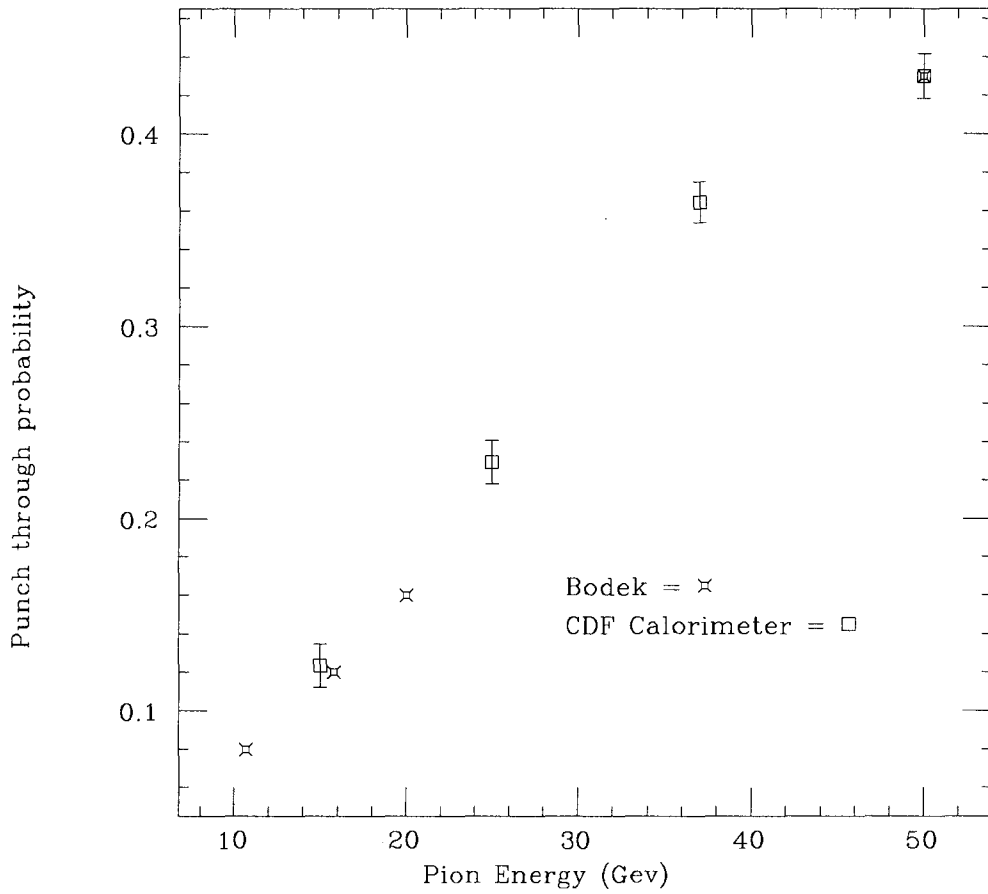


Figure A.16: Punch through probability as a function of incident pion energy for the CDF central calorimeter.

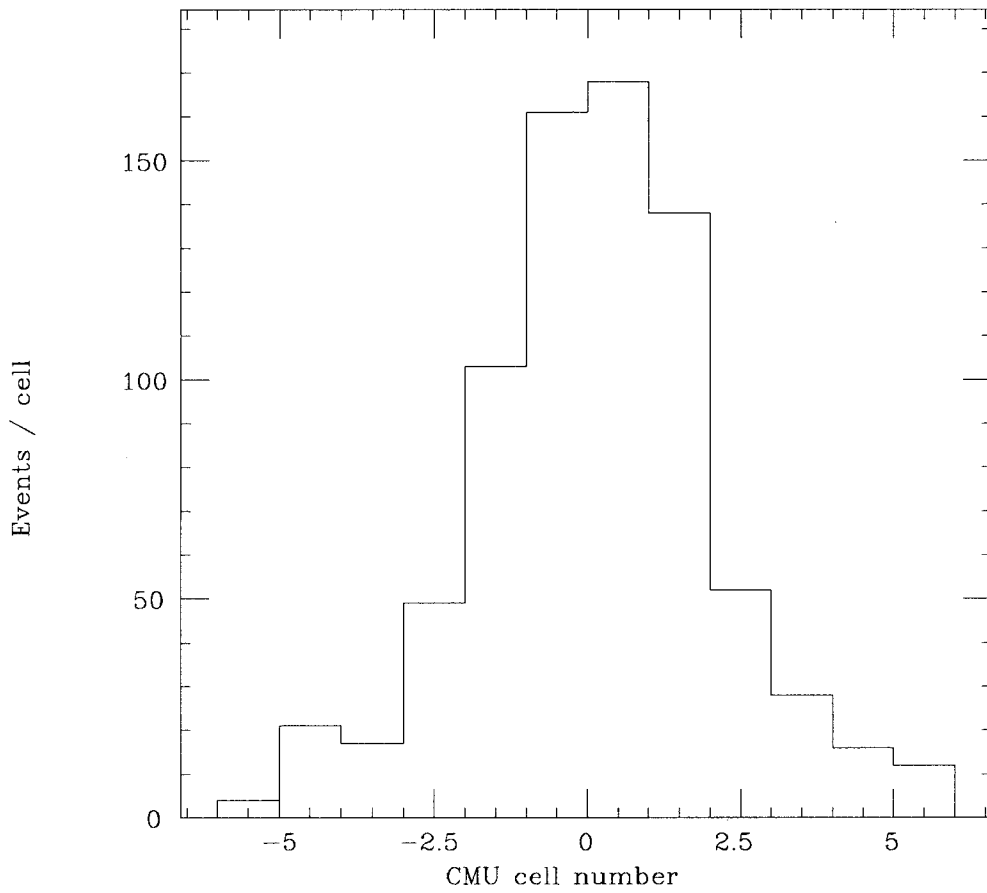


Figure A.17: ϕ , in units of CMU cell number, of the particle which passes closest to the beam axis in a punch through event.

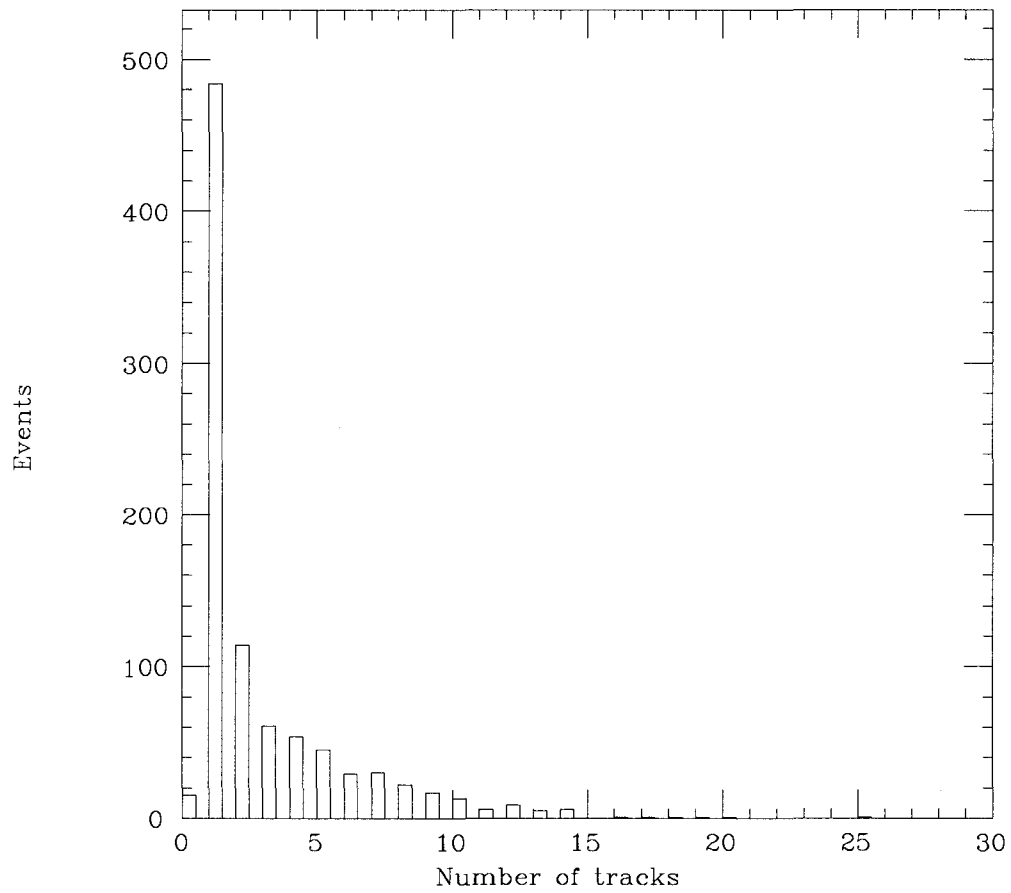


Figure A.18: Number of tracks per punch through event from 50 GeV pions.

A.6 Conclusion

In summary, the CDF muon chambers give adequate resolution in the drift direction of $\sigma_{XY} = 250 \mu\text{m}$ and exceptional resolution along the sense wire of $\sigma_{ZY} = 1.2 \text{ mm}$. It is hoped that difficulties with hadronic punch-through can be overcome through the use of a programmable transverse momentum trigger.

Appendix B

CDF Event Displays

This section contains the CDF event displays for the three W candidates, 7589/1116, 7604/2861, 7605/6279 and for the two Z candidates, 7787/2063, 7787/102 and a background event, 7582/2280. The event displays are of two types. The first type is a display of the CTC looking along the direction of the antiproton beam. The azimuthal angle, $\phi = 0^\circ$, is along the horizontal axis to the right of the display and ϕ increases in the counterclockwise direction. The positive Z axis is vertically outward from the display. The magnetic field has a magnitude of 1.515 Tesla along the negative Z axis (i.e. into the display) throughout the interior of the large circular boundary of the CTC. The positively charged particles are therefore deflected toward increasing ϕ . Around the outside of the CTC is displayed the central calorimeter energy deposited in each 15° phi slice. The rectangles shaded by dots represent electromagnetic energy while the rectangles containing slanted lines denote hadronic energy. The rectangles forming the outermost circle are the central muon chambers and the muon hits are shown in the wedge through which the muon passed. The left-right ambiguity of the muon hits isn't resolved in the picture so both possibilities are shown. The transverse momentum, ϕ and $\cot \theta$, where θ is the polar angle with respect to the positive Z axis are indicated for each muon.

The second type of display is the lego plot of the calorimeter energy in the CDF

detector. The calorimeter has been unfolded into $\eta \times \phi$ space where η is pseudorapidity. The vertical axis is the transverse energy deposited in an individual tower of the calorimeter where a calorimeter tower size is usually about 0.1×0.26 in $\eta \times \phi$ space. Electromagnetic transverse energy is shown in the rectangles shaded with dots and hadronic transverse energy is shown by the rectangles containing slanted lines. A $\mu \rightarrow$ symbol in the lego plot, indicates the calorimeter tower through which the muon passed. $|\vec{E}_t^{\text{Cal}}|$ is indicated as is the azimuthal angle, ϕ_{E_t} , of the missing E_t .

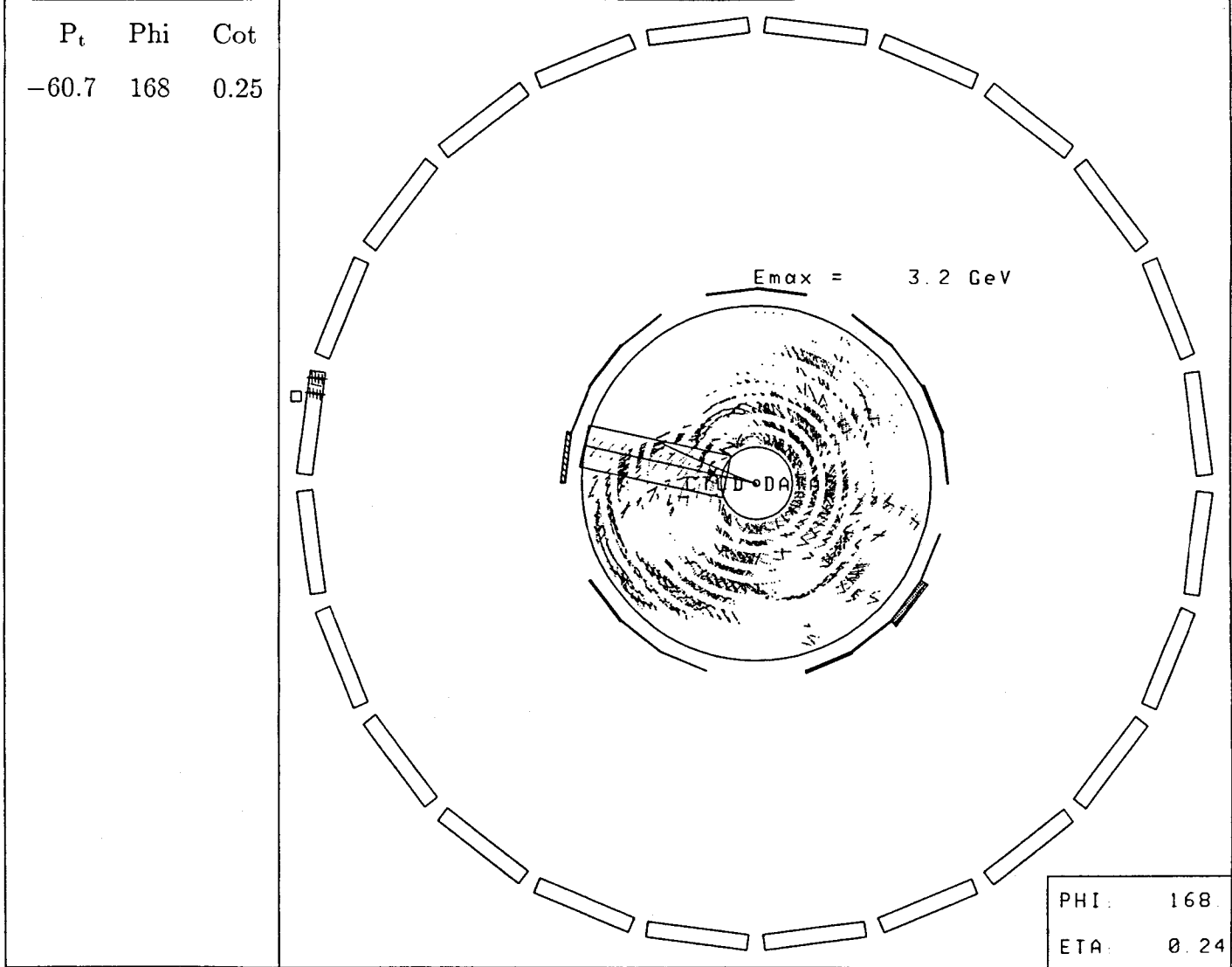


Figure B.1: End view of the CDF central detector for event 7605/6279.

DAIS E transverse Eta-Phi LEGO Plot
 Max tower E= 22.2 Min tower E= 0.50 N clusters

METS: Etotal = 403.4 GeV. Et(scaler)= 75.7
 Et(miss)= 34.9 at Phi= 190.8 Deg.

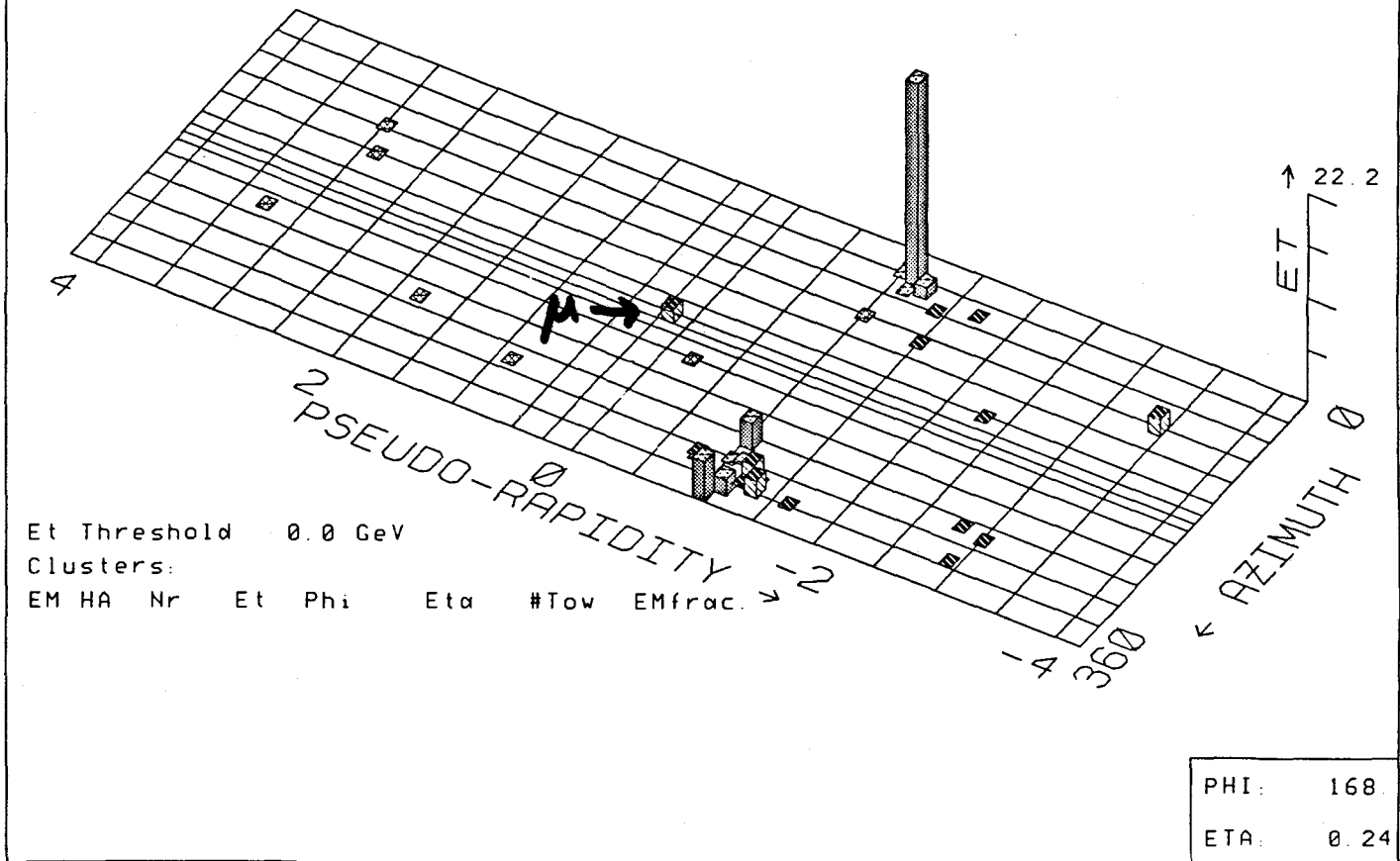


Figure B.2: Lego plot of the CDF calorimeter for event 7605/6279.

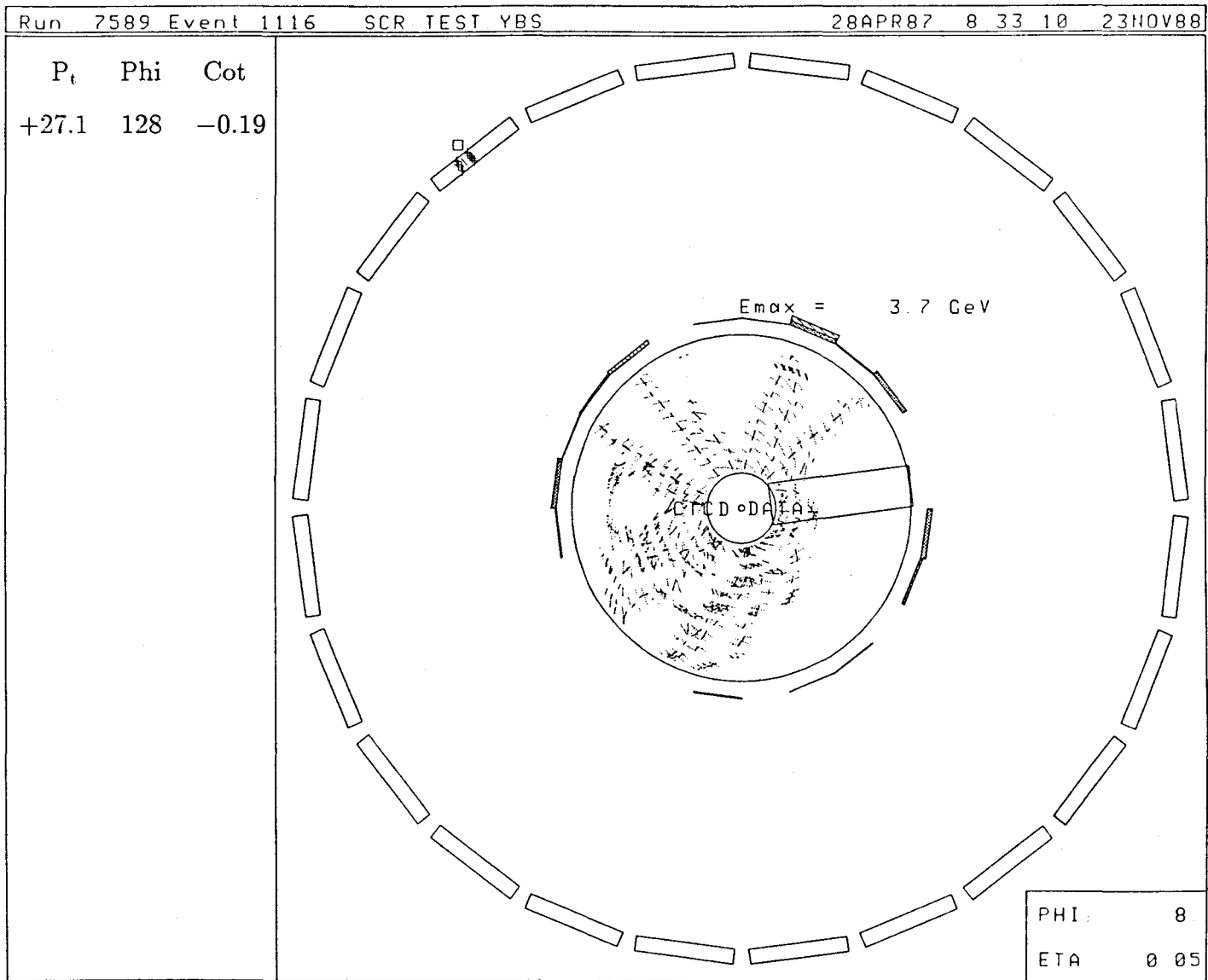


Figure B.3: End view of the CDF central detector for event 7589/1116.

DAIS E transverse Eta-Phi LEGO Plot
 Max tower E= 2.9 Min tower E= 0.50 N clusters
 METS: Etototal = 447.7 GeV. Et(scaler)= 58.3
 Et(miss)= 12.9 at Phi= 239.5 Deg.

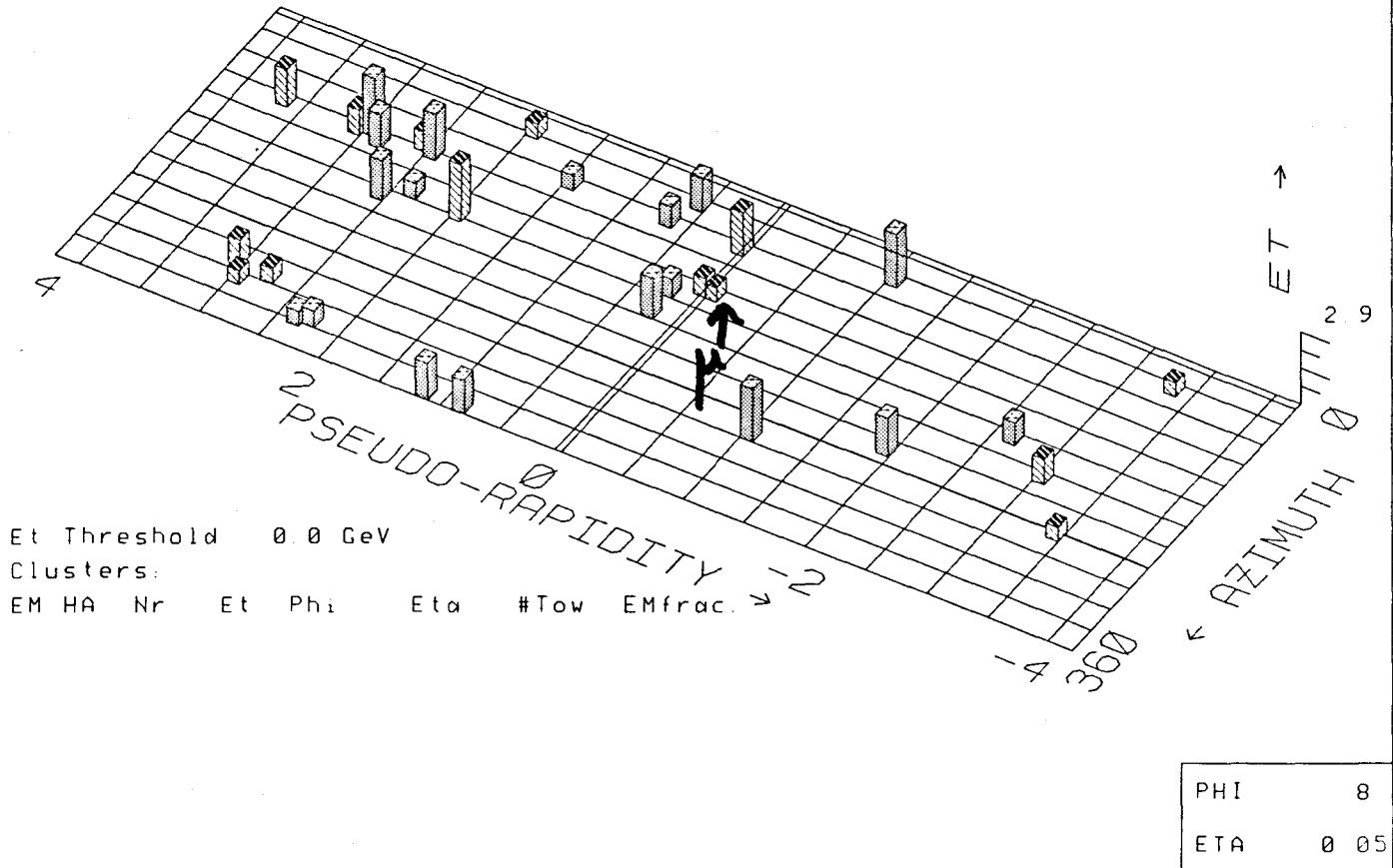


Figure B.4: Lego plot of the CDF calorimeter for event 7589/1116.

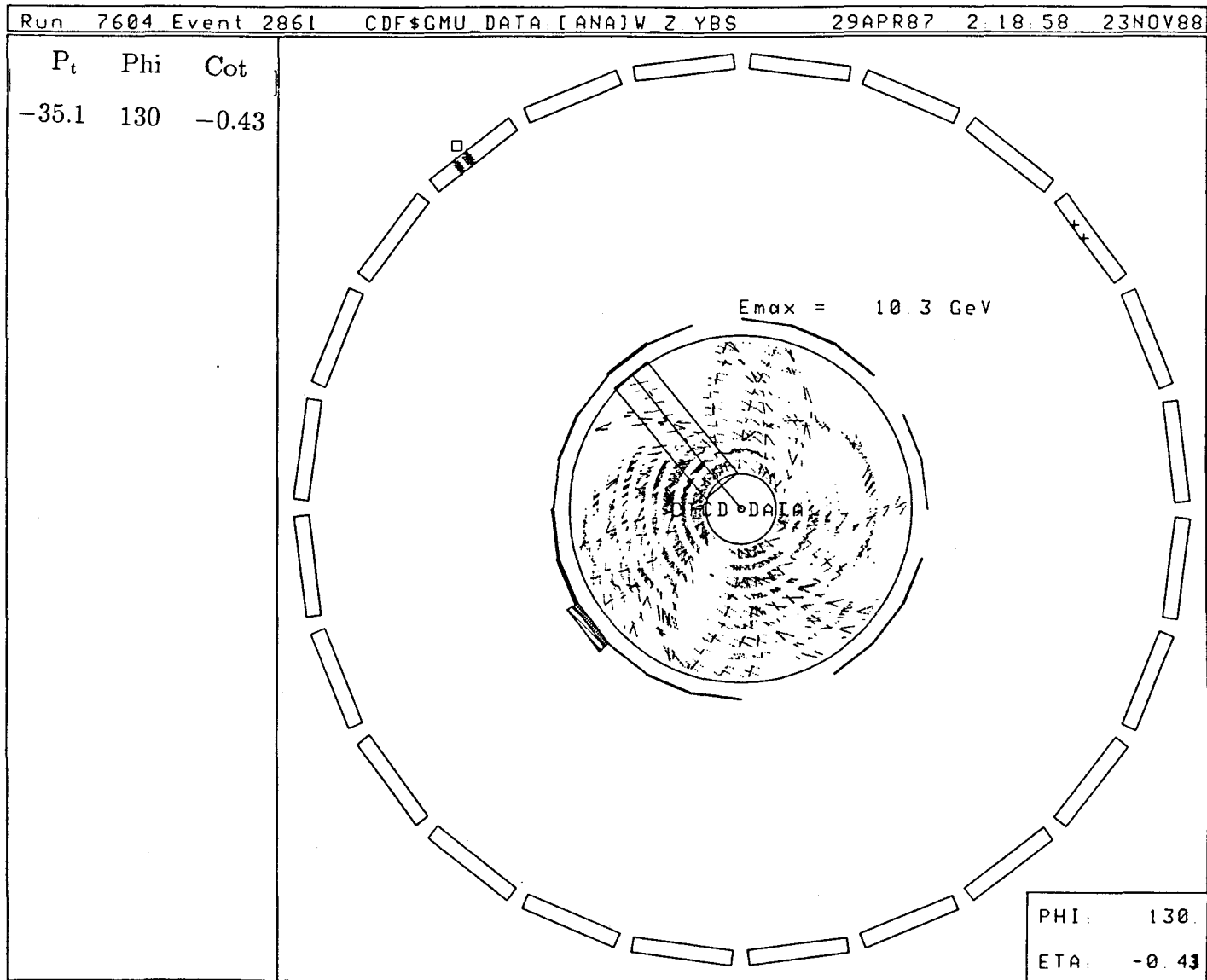


Figure B.5: End view of the CDF central detector for event 7604/2861.

DAIS E transverse Eta-Phi LEGO Plot
 Max tower E= 6.6 Min tower E= 0.50 N clusters
 METS: Etotal = 488.5 GeV. Et(scaler)= 54.0
 Et(miss)= 12.2 at Phi= 46.7 Deg.

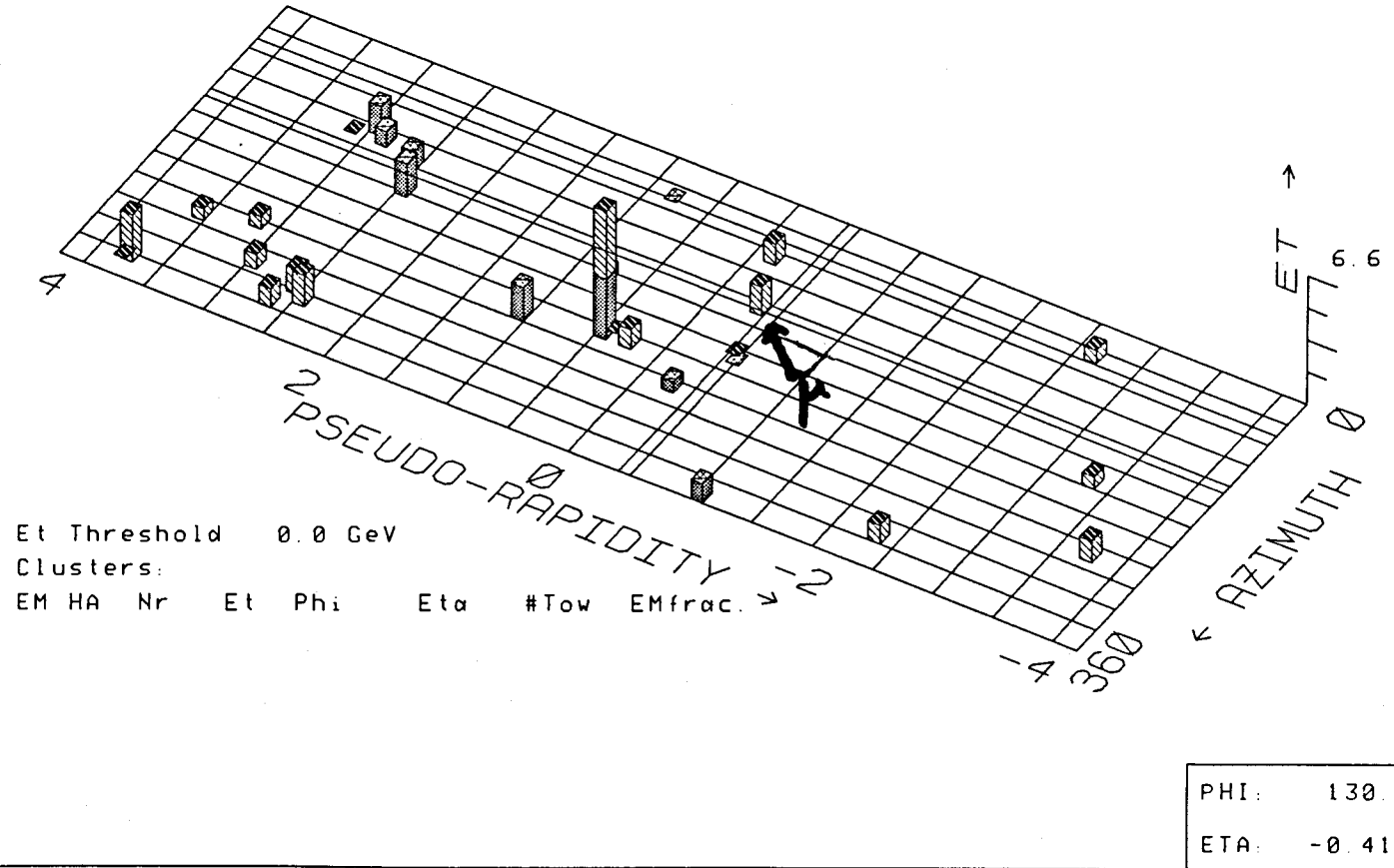


Figure B.6: Lego plot of the CDF calorimeter for event 7604/2861.

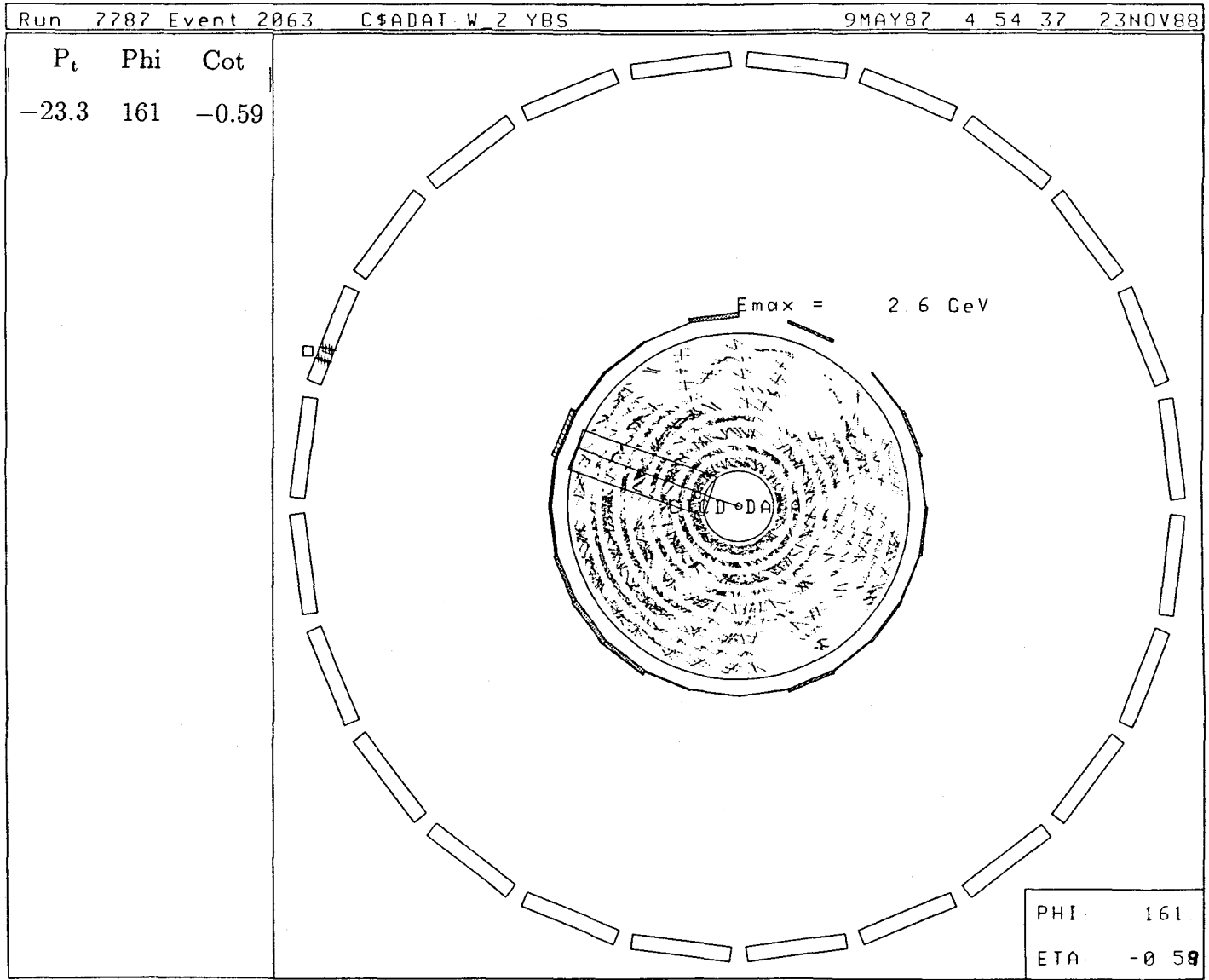


Figure B.7: End view of the CDF central detector for event 7787/2063.

DAIS E transverse Eta-Phi LEGO Plot
 Max tower E= 3.0 Min tower E= 0.50 N clusters
 METS: Etotal = 271.2 GeV. Et(scaler)= 38.8
 Et(miss)= 7.8 at Phi= 355.1 Deg.

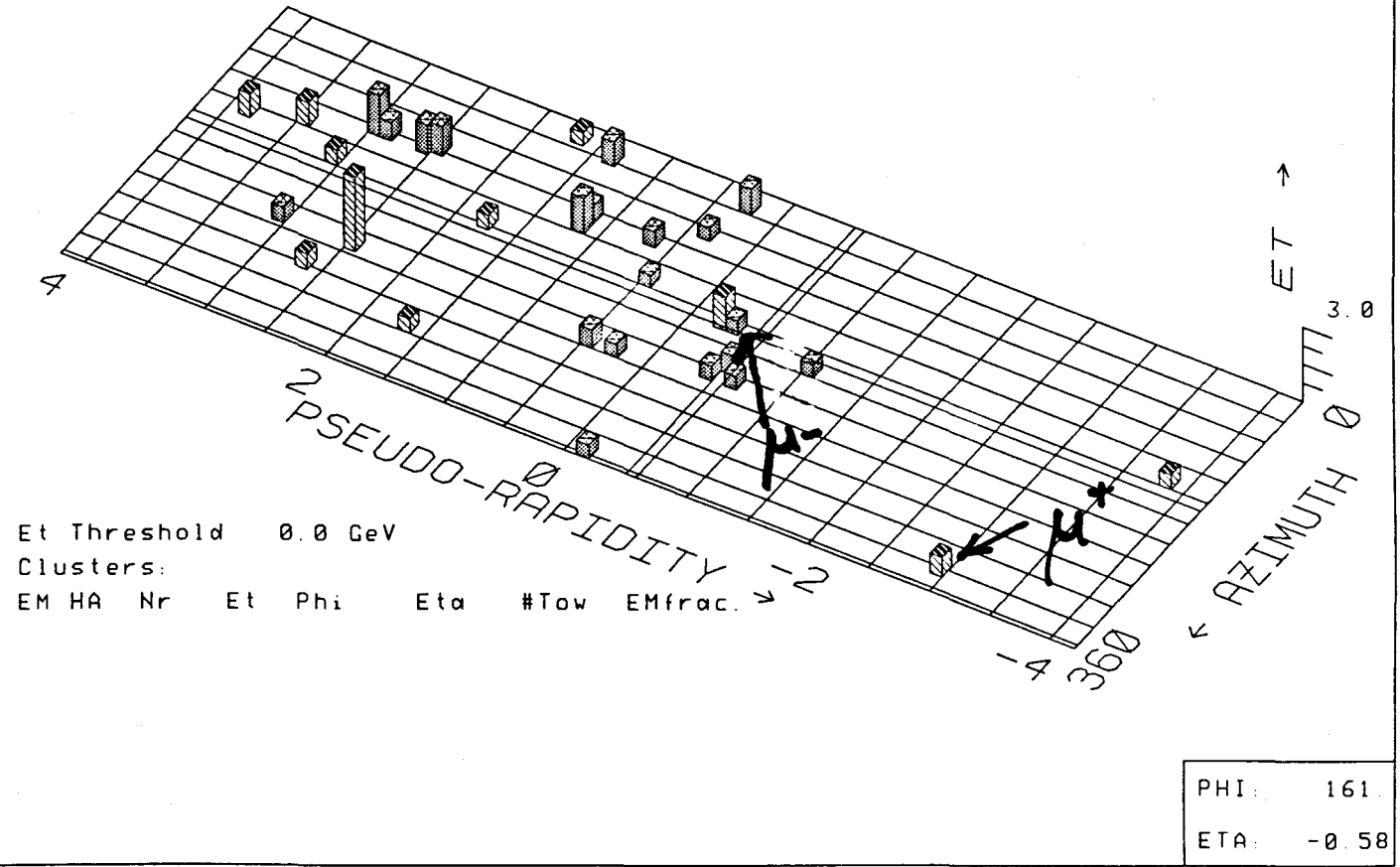


Figure B.8: Lego plot of the CDF calorimeter for event 7787/2063.

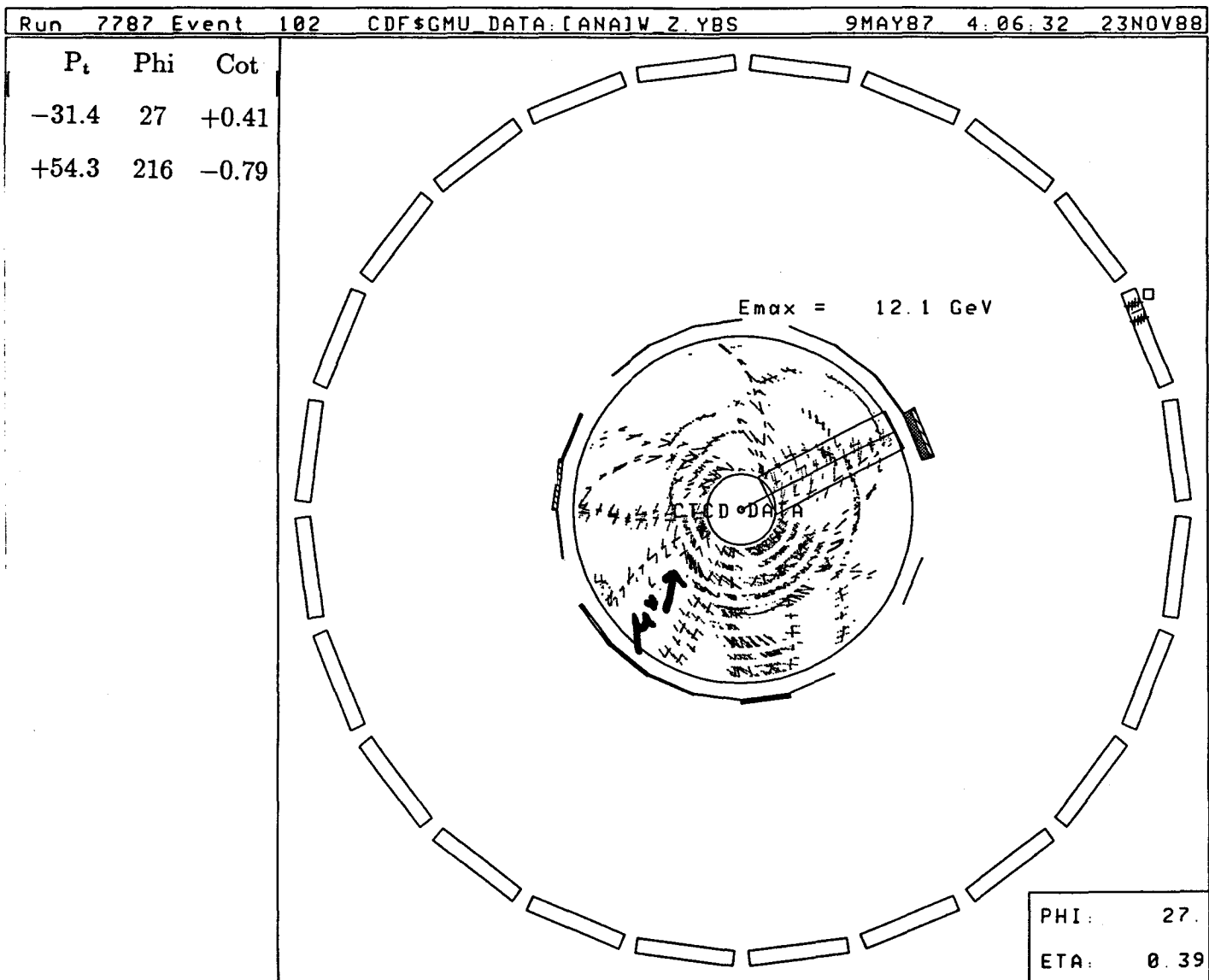


Figure B.9: End view of the CDF central detector for event 7787/102.

DAIS E transverse Eta-Phi LEGO Plot
 Max tower E= 5.8 Min tower E= 0.50 N clusters
 METS: Etotal = 274.7 GeV. Et(scaler)= 54.7
 Et(miss)= 5.0 at Phi= 298.7 Deg.

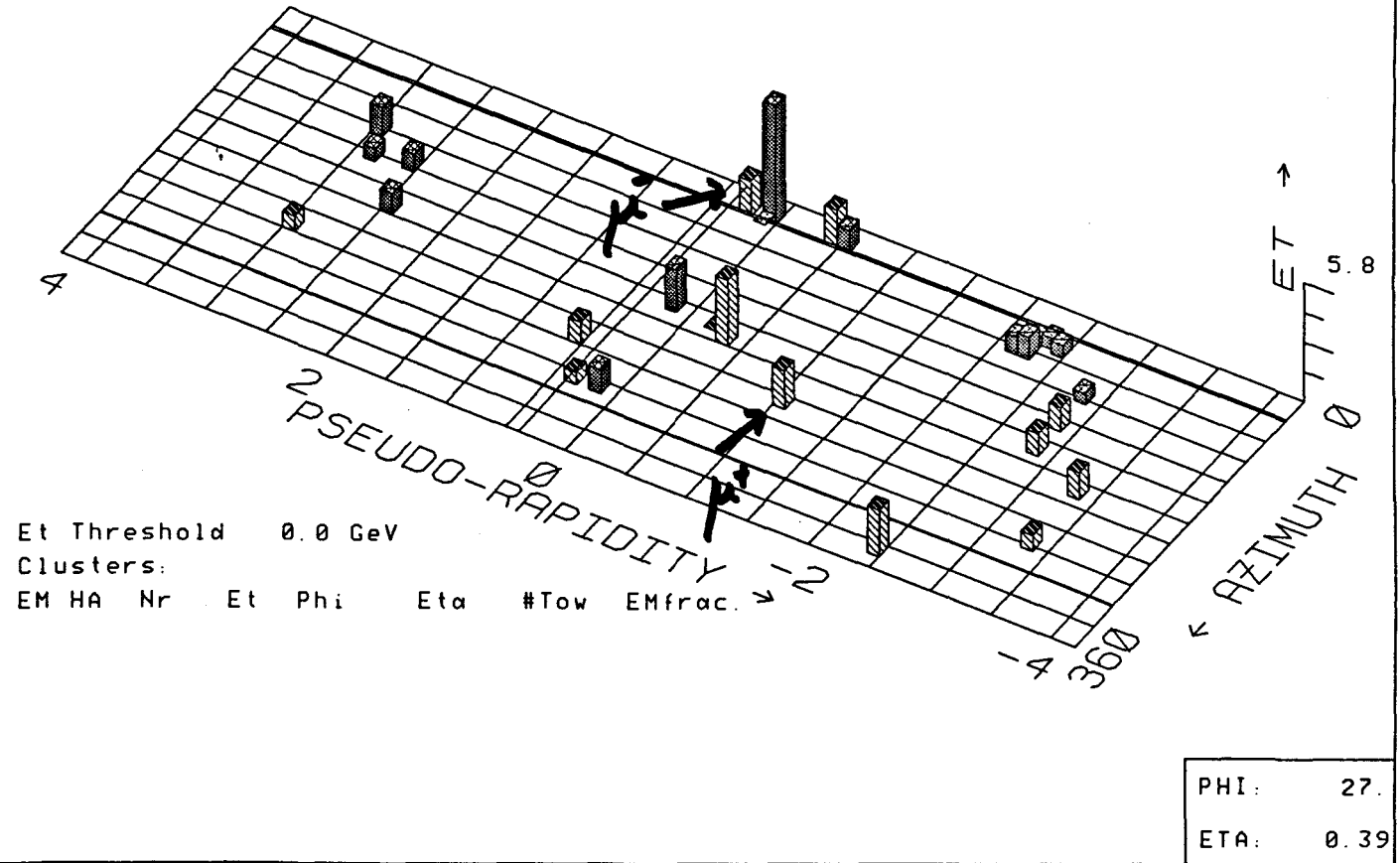


Figure B.10: Lego plot of the CDF calorimeter for event 7787/102.

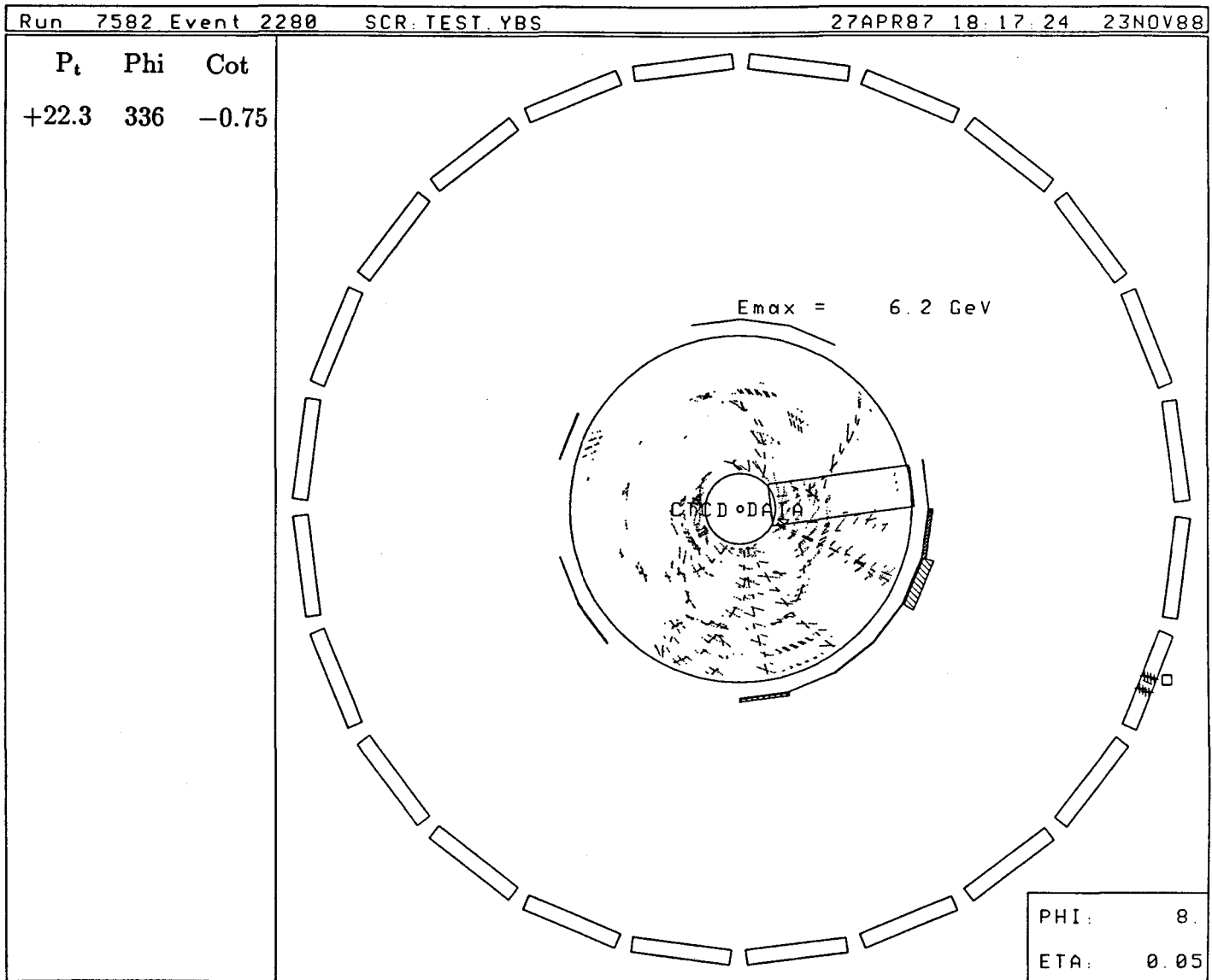


Figure B.11: End view of the CDF central detector for event 7582/2280.

Appendix C

Two Interesting Events

This section contains the CDF event displays for two events, 7310/468 and 7343/1999, which failed to pass the central muon trigger but did pass the calorimetry trigger. They are both high P_t muons which are recoiling against jets. Event 7310/468 has a muon corrected missing E_t of $|\vec{E}_t| = 30.0 \pm 8.4$ GeV at an azimuthal angle of $\phi = 178.8^\circ$ while event 7343/1999 has a muon corrected missing E_t of $|\vec{E}_t| = 24.9 \pm 8.9$ GeV at an azimuthal angle of $\phi = 119.3^\circ$.

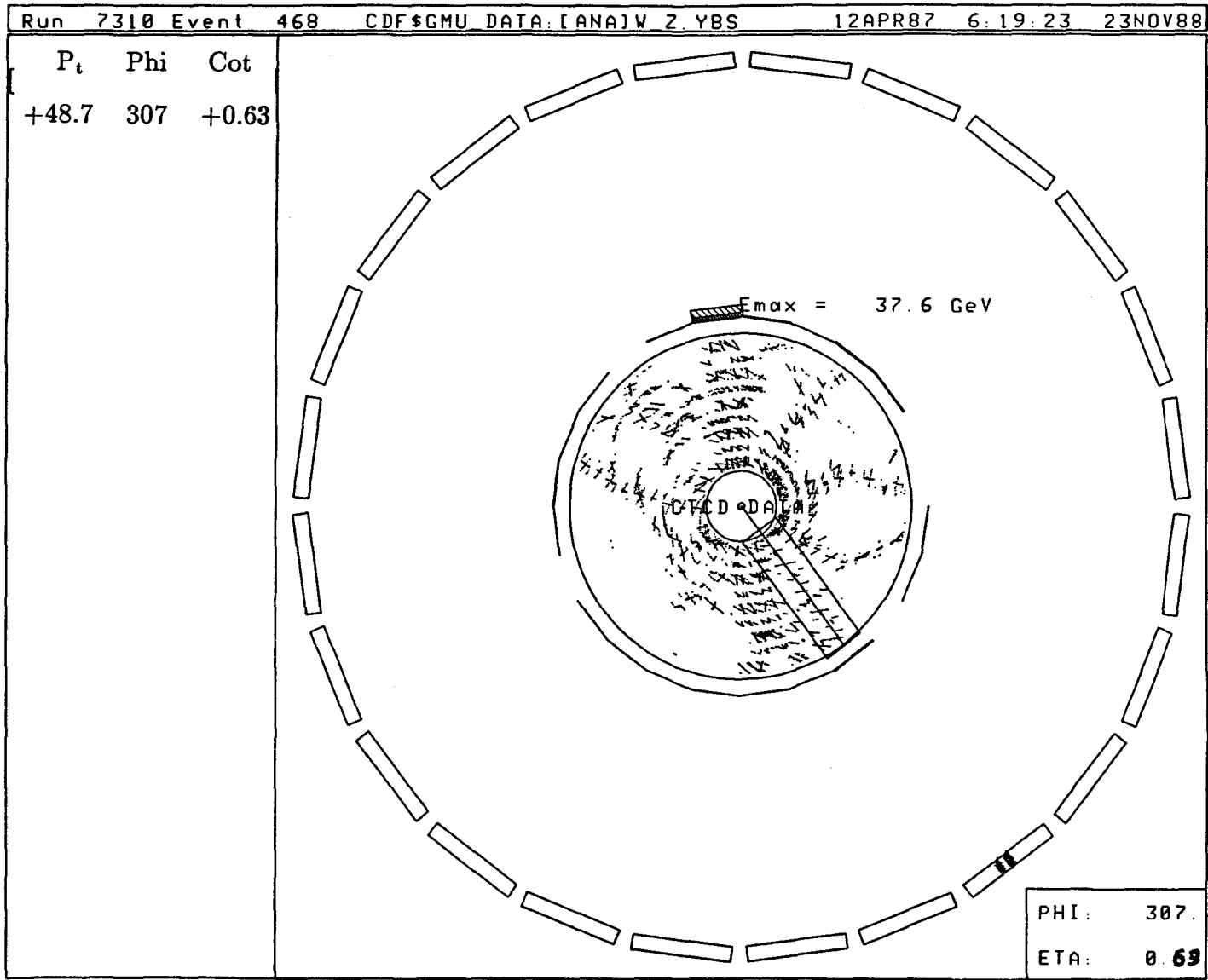


Figure C.1: End view of the CDF central detector for event 7310/468.

DAIS E transverse Eta-Phi LEGO Plot
 Max tower E= 15.2 Min tower E= 0.50 N clusters
 METS: Etotal = 386.4 GeV. Et(scaler)= 74.3
 Et(miss)= 39.4 at Phi= 269.7 Deg.

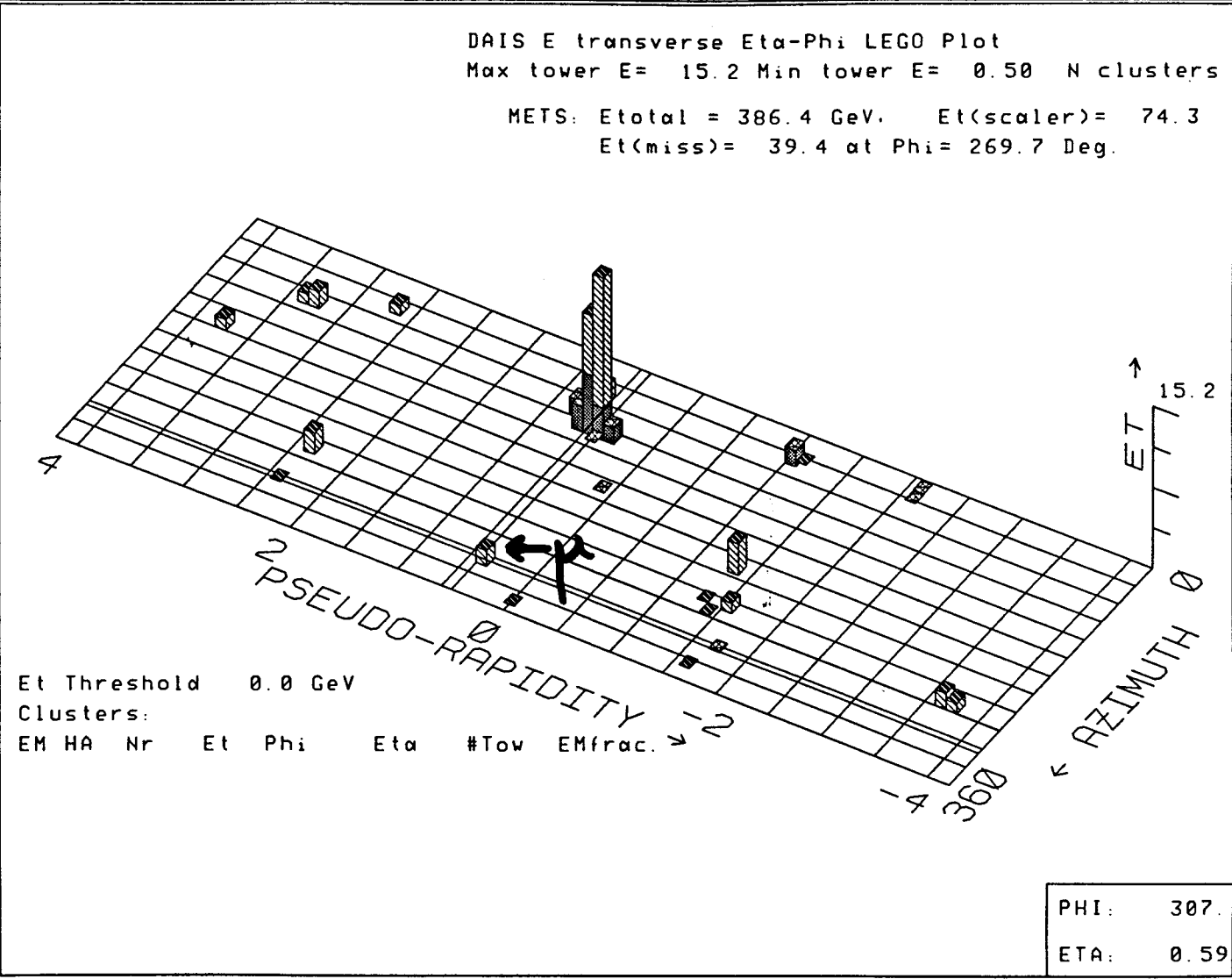


Figure C.2: Lego plot of the CDF calorimeter for event 7310/468.

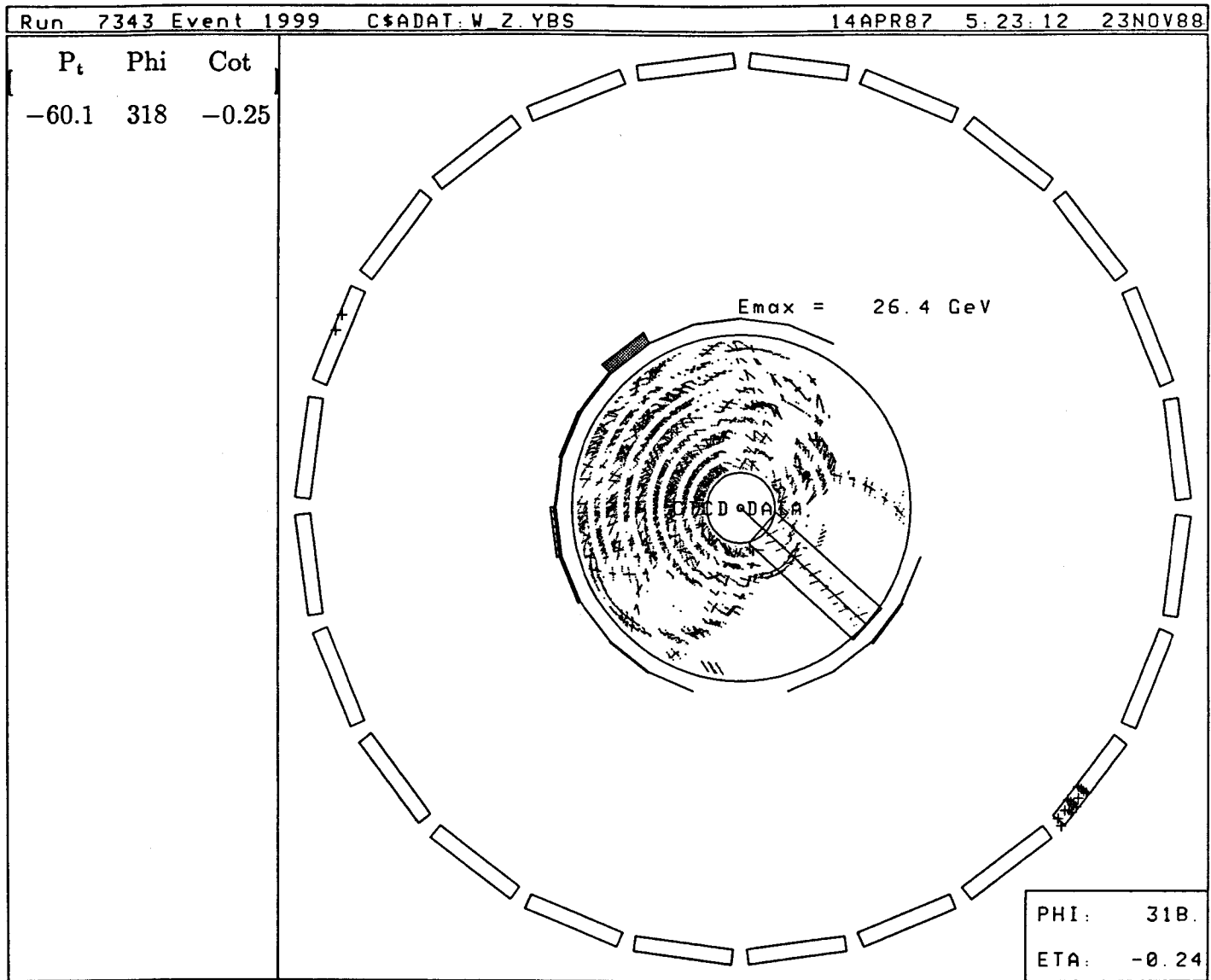


Figure C.3: End view of the CDF central detector for event 7343/1999.

DAIS E transverse Eta-Phi LEGO Plot
 Max tower E= 13.8 Min tower E= 0.50 N clusters
 METS: Etotal = 285.4 GeV. Et(scaler)= 74.7
 Et(miss)= 39.8 at Phi= 327.9 Deg.

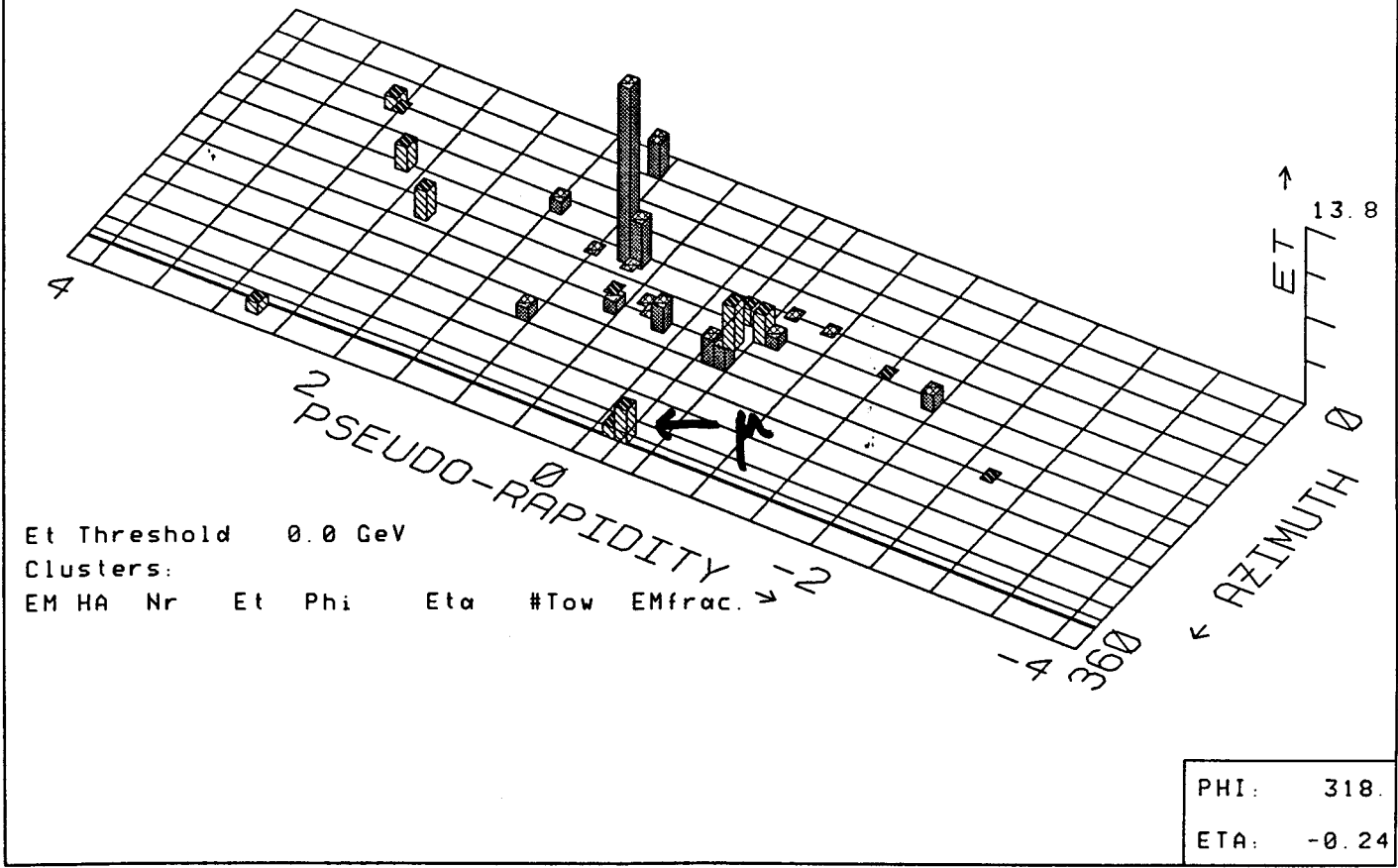


Figure C.4: Lego plot of the CDF calorimeter for event 7343/1999.

Bibliography

- [1] C. Albajar et al., *Phys. Lett.* **198B**, 271 (1987); G. Arnison et al., *Phys. Lett.* **122B**, 103 (1983); M. Banner et al., *Phys. Lett.* **122B**, 476 (1983).
- [2] G. Arnison et al., *Phys. Lett.* **166B**, 484 (1986).
- [3] F. Abe et al., *NIM A* **271**, 387 (1988).
- [4] J. Kim et al., *Rev. Mod. Phys.* **53**, 211 (1981).
- [5] S. D. Drell, T-M Yan, *Phys. Rev. Lett.* **25**, 316 (1970).
- [6] G. Altarelli et al., *Nucl. Phys.* **B246**, 12 (1984); G. Altarelli et al., *Z. Phys.* **C27**, 617 (1985).
- [7] F. Paige, S. Protopopescu, ISAJET Monte Carlo, BNL-38034 (1986).
- [8] G. Ascoli et al., "The CDF Central Muon Detector", *NIM A* **268**, 33 (1988).
- [9] D.A. Smith, H.B. Jensen, "Pion Punchthrough Probability in the Central Calorimeter", CDF-707 (1988).
- [10] G. Drake et al., "CDF Front End Electronics: the RABBIT System", *NIM A* **269**, 68 (1988).
- [11] D. Amidei et al., "A Two Level Fastbus Based Trigger System for CDF", *NIM A* **269**, 51 (1988)

- [12] G. Ascoli et al., "CDF Central Muon System Level 1 Trigger", *NIM A269*, 63 (1988)
- [13] G.W. Foster et al., "A Fast Hardware Track Finder for the CDF Central Tracking Chamber", *NIM A269*, 93 (1988)
- [14] "A Measurement of Intermediate Vector Boson Production in 1.8 TeV $p\bar{p}$ Collisions", The CDF Collaboration (to be published in *Phys. Rev. Let.*, 1989)
- [15] E.Eichten, I.Hinchliff, K.Lane, and C.Quigg, *Rev. Mod. Phys.* **56**, 579 (1984)
- [16] D.A. Smith and T.K. Westhusing, "Decay-in-Flight Acceptance of the Central Muon Chambers", CDF-726 (1988)
- [17] G. Ascoli et al., "An Alignment System for the CDF Central Muon Chambers", *NIM A268*, 41 (1988)
- [18] A. Bodek, University of Rochester preprint UR911 (1985); to be published in Proc. Workshop for Muon Identification at the SSC, Madison, Wisconsin (1985).
- [19] Muzaffer Atac, private communication

Vita

[REDACTED]

[REDACTED]

[REDACTED]

[REDACTED]. Upon graduation he returned to Houston at Rice University to further refine his roping and riding and pumping of the black gold. Always looking for adventure in distant lands, not so little Tommy decided to show those damn Yankees in Illinois about roping and riding and pumping black gold. The only oil to be found however was made from corn. He also found that roping and riding weren't held in high esteem by those damn yankees so he studied physics instead. In December, 1988 he was awarded the Ph.D. for his efforts. But all he really wants to do is rope and ride and pump black gold. Maybe in Italy....